# NOTE TO USERS

Page(s) not included in the original manuscript are unavailable from the author or university. The manuscript was microfilmed as received

iii

This reproduction is the best copy available.

UMI®

RICE UNIVERSITY


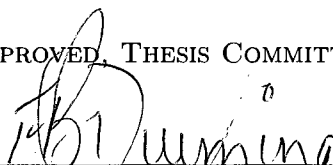# Rydberg Atom Wavepacket Dynamics in One and Two-Dimensions
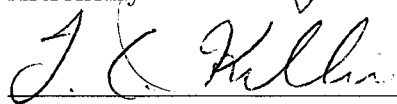
by

**Jeffery Mestayer**


A THESIS SUBMITTED
IN PARTIAL FULFILLMENT OF THE
REQUIREMENTS FOR THE DEGREE

**Doctor of Philosophy**


APPROVED, THESIS COMMITTEE:

F.B. Dunning, Advisor
Professor and Chair of Physics and
Astronomy

T.C. Killian
Associate Professor of Physics and
Astronomy

P. Brooks
Professor of Chemistry


Houston, Texas

January, 2009

UMI Number: 3362361

INFORMATION TO USERS

The quality of this reproduction is dependent upon the quality of the copy submitted. Broken or indistinct print, colored or poor quality illustrations and photographs, print bleed-through, substandard margins, and improper alignment can adversely affect reproduction.

In the unlikely event that the author did not send a complete manuscript and there are missing pages, these will be noted. Also, if unauthorized copyright material had to be removed, a note will indicate the deletion.

# UMI®

# Rydberg Atom Wavepacket Dynamics in One and Two-Dimensions

## Jeffery Mestayer

## Abstract

Atoms in high-lying Rydberg states with large values of principal quantum number $n$, $n \geq 300$, form a valuable laboratory in which to explore the control and manipulation of quantum states of mesoscopic size using carefully tailored sequences of short electric field pulses whose characteristic times (duration and/or rise/fall times) are less than the classical electron orbital period. Atoms react to such pulse sequences very differently than to short laser or microwave pulses providing the foundation for a number of new approaches to engineering atomic wavefunctions. The remarkable level of control that can be achieved is illustrated with reference to the generation of localized wavepackets in Bohr-like near-circular orbits, and the production of non-dispersive wavepackets under periodic driving and their transport to targeted regions of phase space. New protocols continue to be developed that will allow even tighter control with the promise of new insights into quantum-classical correspondence, information storage in mesoscopic systems, physics in the ultra-fast ultra-intense regime, and non-linear dynamics in driven systems.

# Contents

# Tables

# Figures

x

# Chapter 1

# Introduction

Engineering the quantum states of microscopic and mesoscopic objects is a goal in many current fields of research ranging from nanomechanical devices to quantum information processing[1, 2, 3, 4]. Recent advances in experimental technique now allow accurate measurements of the dynamical behavior of atomic systems on a variety of time scales extending into the attosecond regime through the use of short electric field pulses. This has been widely exploited to explore both electron and heavy-particle motions in atoms, molecules, and solids[5, 6].

One area in which major advances have been made is the control of electronic motions in high-$n$ Rydberg atoms using carefully-tailored sequences of pulsed electric fields. Such atoms provide a valuable laboratory in which to explore, control, and manipulate quantum states of mesoscopic size. Here we demonstrate the remarkable control that can be achieved in very high-$n$ Rydberg atom wavepackets using a tailored sequence of half-cycle pulses. There are number of advantages to using very high-$n$ wavepackets. As we will see in the next section, the physical properties of high-$n$ atoms are dramatically different compared to lower lying states. Most importantly, at high-$n$ the spacing between adjacent energy levels becomes extremely small thus allowing the semiclassical modeling of the system. In addition, the change in the

spacing between levels is also very small, leading to a nearly uniformly spaced set of energy levels which is similar to the spectrum of the harmonic oscillator. This near-uniform spacing allows the creation of wavepackets with minimum dispersion, and thus appreciable lifetimes. These characteristics make the very-high-$n$ Rydberg atom an ideal system for the coherent control and manipulation of wavepackets.

## 1.1 Rydberg Atom Properties

A Rydberg atom contains one or more electrons which have been excited to a high principal quantum number, $n$. Many of the physical properties of Rydberg atoms are quite exaggerated compared to low-lying or ground state atoms[7]. Some of these characteristics as listed in table 1.1 along with their dependence on $n$ and typical numerical values for several specific $n$ levels. One such important property is the mean distance between the electron and the nucleus, which scales as $n^2$. At $n = 350$, the mean radius reaches 6.5 $\mu$m, which is comparable to the size of a biological cell, and would be resolvable using an optical micropscope if the Rydberg atom were a solid object. Due to the large separation between the electron and the core, the properties of the Rydberg atom resemble those of the hydrogen atom. The time scale for Rydberg wavepackets, given by the orbital period of an electron in a Kepler orbit about the core, also rapidly increases with increasing $n$. It is of the order of a few nanoseconds (6.5 ns at $n = 350$) which is easily observed using modern electronic equipment. The binding energy of the electron decreases rapidly with increasing $n$ to

hundreds of $\mu$eV at high-$n$, so very little energy is required to ionize it. In addition, at high-$n$, very weak externally applied electric fields ($\sim$ 1mV/cm) can strongly perturb electronic motion. As a result, extreme care must be taken to minimize any stray electric fields present in the experimental volume. However, it is this increased time scale and extreme sensitivity to electric fields that make possible the ability to create, observe, and manipulate the motion and shape of atomic wavepackets.

Table 1.1 : Physical properties of Rydberg atoms.

| Property | Scaling (a.u.) | $n = 1$ | $n = 30$ | $n = 350$ |
|---|---|---|---|---|
| Mean Radius | $n^2$ | $5.3 \times 10^{-9}$ cm | $4.8 \times 10^{-6}$ cm | 6.50 $\mu$m |
| Orbital Period | $2\pi n^3$ | $1.5 \times 10^{-4}$ ps | 4.1 ps | 6.5 ns |
| Binding Energy | $-1/2n^2$ | 13.6 eV | 15 meV | 111 $\mu$eV |
| Energy Spacing | $1/n^3$ | 10.2 eV | 1.0 meV | 0.63 $\mu$eV |
| Classical Field Ionization Threshold | $1/16n^4$ | $3.0 \times 10^8$ V/cm | 400 V/cm | 22 mV/cm |

It is straightforward to create and apply unidirectional electric field pulses (termed half-cycle pulses or HCPs), whose duration are much smaller than the orbital time scale ($T_p \ll T_n$), to high-$n$ Rydberg atoms. In this limit, the applied field delivers an impulsive momentum transfer or "kick" to the excited electron given by

$$\Delta p = - \int F_{HCP}(t) dt \qquad (1.1)$$

where $F_{HCP}(t)$ is the electric field associated with the HCP. Each applied HCP imparts an energy transfer given by

$$\Delta E = \frac{\Delta \vec{p}^2}{2} + \vec{p}_i \cdot \Delta \vec{p} \qquad (1.2)$$

leading to the coherent excitation of a range of Rydberg states. A strong HCP that delivers an energy transfer, $\Delta E$, which exceeds the binding energy of the original Rydberg atom can induce ionization. Monitoring this ionization as a function of time provides a tool for monitoring the motion of Rydberg atom wavepackets. In addition, application of a train of HCPs can be used to study interesting effects such as dynamical stabilization. Also, in the following chapters we will see that a carefully tailored sequence of HCPs can be used to steer a Rydberg wavepacket to arbitrary locations in phase space, laying the foundation for the engineering of atomic wavefunctions.

## 1.2 Overview

In this work, we will discuss the generation of Rydberg atom wavepackets, their control and manipulation, and the experimental observation of their evolution. The resulting dynamics of these wavepackets is analyzed using the classical trajectory Monte Carlo Method[8]. The experimental techniques for creating and observing

wavepackets are summarized in chapter 3.

The control and manipulation of localized wavepackets whose motion is confined to a single dimension is discussed in chapter 4. It is demonstated that, once generated, a wavepacket can be dynamically trapped in a localized region in phase space known as a "stable island". It is possible to transport the wavepacket to a selected location in phase space by adiabatically shifting the position of the stable island. This technique allows control of the final $n$-state distribution as well as the transfer to other stable islands in phase space.

The remarkable results of the manipulation of wavepackets in two dimensions are discussed in chapter 5. The carefull control of Rydberg atom $l$-state distributions leads to the production of localized Bohr-like circular wavepackets. While these localized wavepackets eventually dephase, it is demonstrated that localization can be re-induced using a single HCP. In addition, it is shown that localization can be maintained indefinitely using a tailored periodic train of HCPs.

# Chapter 2

# Rydberg Atom Theory

## 2.1 Coulomb Potential and Orbital Dynamics

The Hamiltonian of a single electron atom in atomic units is

$$H = \frac{p^2}{2} - \frac{1}{|\vec{r}|} \tag{2.1}$$

where $\vec{p}$ is the momentum and $\vec{r}$ is the distance from the nucleus. This Hamiltonian is common to both the classical Rydberg atom and the Kepler motion of planetary orbits. At very high-$n$, due to the close spacing of the energy levels, the dynamics of the Rydberg atom can frequently be modeled classically[9, 10, 11]. Therefore it is useful to describe some of the properties of classical Kepler orbits.

Since the potential only depends on the distance from the nucleus, the system has spherical symmetry and thus it is rotationally invariant. As a consequence, the angular momentum $\vec{L} = \vec{r} \times \vec{p}$ is a constant of the motion. The bound solutions to the Hamiltonian are ellipses, and in polar coordinates are defined by the equation

$$r = \frac{L^2}{1 + \varepsilon \cos\theta} \tag{2.2}$$

A typical orbit is shown in Fig. 2.1. Another quantity that is conserved in this system
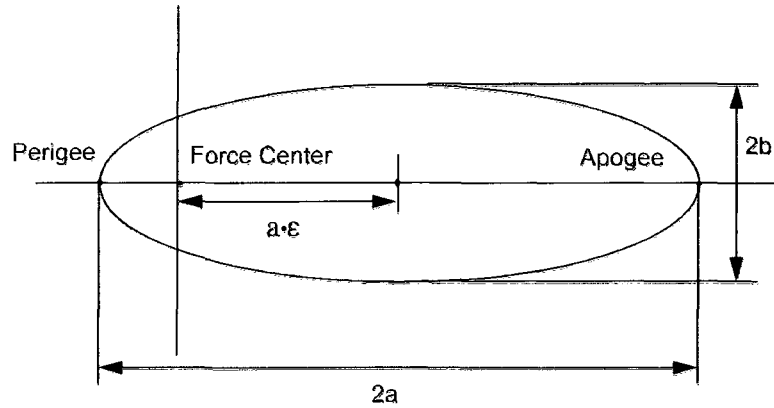
Figure 2.1 : Parameters describing a Kepler orbit.

is the Runge-Lenz vector, which is defined as

$$\vec{A} = \vec{p} \times \vec{L} - \frac{\vec{r}}{|\vec{r}|} \qquad (2.3)$$

The Runge-Lenz vector lies along the major axis of the orbital ellipse and points from the nucleus to the point of closest approach, also known as the perigee. Because the Runge-Lenz vector is in the plane of the orbit, $\vec{A} \cdot \vec{L} = 0$ . The magnitude of the Runge-Lenz vector is equal to the eccentricity, $\varepsilon$ . The value of $\varepsilon$ determines the nature of the orbit. For $\varepsilon > 1$ the motion is hyperbolic and unbound. For bound states however, $\varepsilon$ is defined as

$$\varepsilon = \sqrt{1 + 2EL^2} \qquad (2.4)$$

and is related to the scaled angular momentum $L_0$ by
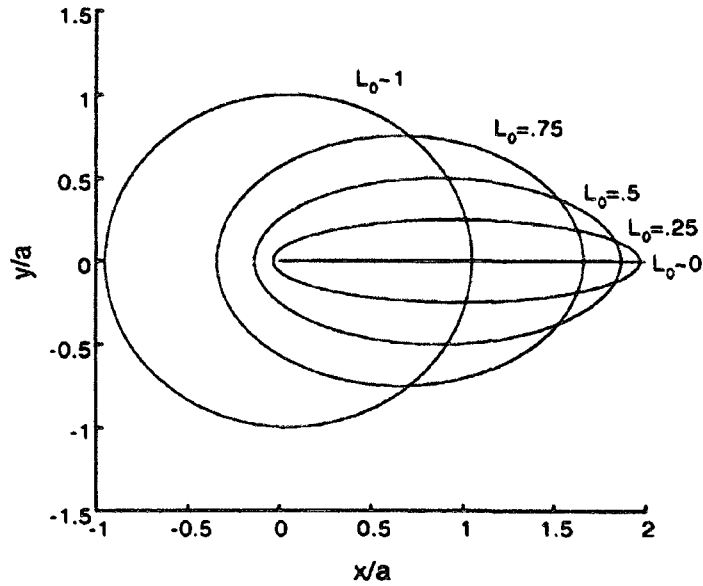
Figure 2.2 : Orbits of varying eccentricity.

$$L_0 = L\sqrt{2E} = \sqrt{1 - \varepsilon^2} \qquad (2.5)$$

Notice that, as shown in Fig.2.2, as $L_0$ varies from 0 to 1.0, the orbit goes from nearly one-dimensional to nearly circular. This fact will prove to be quite important in the upcoming analysis of one and two-dimensional wavepackets.

## 2.2 Rydberg Atoms in External Electric Fields

Rydberg atom electrons occupying very-high-$n$ levels are very strongly perturbed by electric fields that are considered "weak" ($\sim 100$ $\mu$V/cm) by ordinary laboratory

standards. This characteristic presents a tremendous challenge when attempting to selectively photoexcite very-high-$n$ Rydberg atoms. However, if one has the means to precisely control the applied electric field, this same property can be quite useful in the areas of wave packet manipulation and selective ionization. In either case, it is imperative to understand precisely how Rydberg atoms respond to external fields.

### 2.2.1 The Hydrogen Atom in a Static Field
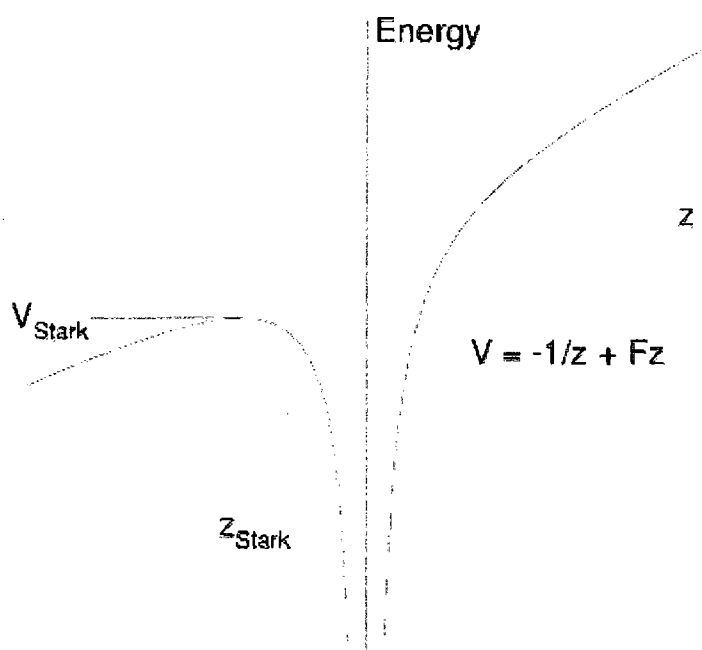


Figure 2.3 : Potential energy of an electron in a uniform electric field in the z-direction.

If a hydrogen atom is placed in an external electric field, $\vec{F}$, in the z direction the resulting potential seen by the electron is

$$V = -\frac{1}{r} + |\vec{F}|z \tag{2.6}$$

The resulting Schrödinger equation is not separable in spherical polar coordinates. The most common way of dealing with this problem is to transform to parabolic coordinates, for which the equation remains separable[12, 13]. The parabolic coordinate system is defined in terms of the Cartesian coordinates as follows

$$\xi = r + z = r(1 + \cos\theta) \tag{2.7}$$

$$\eta = r - z = r(1 - \cos\theta) \tag{2.8}$$

$$\phi = \tan^{-1}\frac{y}{x} \tag{2.9}$$

with the associated inverse transform

$$x = \sqrt{\xi\eta}\cos\phi \tag{2.10}$$

$$y = \sqrt{\xi\eta}\sin\phi \tag{2.11}$$

$$z = (\xi - \eta)/2 \tag{2.12}$$

$$r = (\xi + \eta)/2 \tag{2.13}$$

The parabolic coordinate system is a system of curvilinear coordinates obtained by revolving parabolas about the z-axis as shown in Fig. 2.4. Using the above transformation equations the Schrödinger is now written as[7]
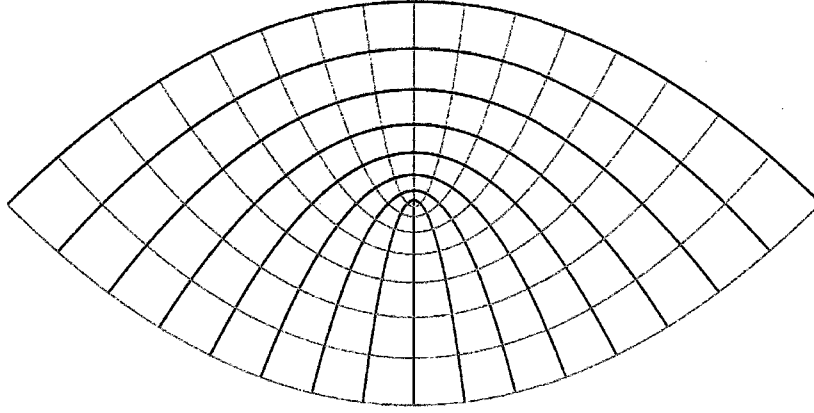
Figure 2.4 : Parabolic coordinate system.

$$\left(-\frac{\nabla^2}{2} - \frac{2}{\xi + \eta} + \frac{F(\xi - \eta)}{2}\right)\psi = W\psi \qquad (2.14)$$

where

$$\nabla^2 = \frac{4}{\xi + \eta}\frac{\partial}{\partial\xi}\left(\xi\frac{\partial}{\partial\xi}\right) + \frac{4}{\xi + \eta}\frac{\partial}{\partial\eta}\left(\eta\frac{\partial}{\partial\eta}\right) + \frac{1}{\xi\eta}\frac{\partial^2}{\partial\phi^2} \qquad (2.15)$$

and W is the energy. Here we use the most common technique for separating variables

in a partial differential equation, assuming a product solution of the form[12]

$$\psi(\xi, \eta, \phi) = u_1(\xi)u_2(\eta)e^{im\phi} \qquad (2.16)$$

Inserting the trial product solution back into (2.14), we find that we can recover two

independent equations

$$\frac{d}{d\xi}\left(\xi\frac{du_1}{d\xi}\right) + \left(\frac{W\xi}{2} + Z_1 - \frac{m^2}{4\xi} - \frac{F\xi^2}{4}\right)u_1 = 0 \qquad (2.17)$$

and

$$\frac{d}{d\eta}\left(\eta\frac{du_2}{d\eta}\right) + \left(\frac{W\eta}{2} + Z_2 - \frac{m^2}{4\eta} - \frac{F\eta^2}{4}\right)u_2 = 0 \qquad (2.18)$$

Notice that $m$ only appears as a squared term, thus its sign is irrelevant. Therefore the wavefunctions associated with $\pm m$ are degenerate. This is not surprising considering the cylindrical symmetry in this system. The parameters $Z_1$ and $Z_2$ are separation constants, and are related by the expression

$$Z_1 + Z_2 = 1 \qquad (2.19)$$

The terms $Z_1$ and $Z_2$ are often referred to as the effective charges, because they mathematically resemble positive binding charges in the $\xi$ and $\eta$ directions.

The most concise way of proceeding at this point is to solve the zero field case, and then to use the zero field parabolic wavefunctions as basis functions in a perturbation expansion. In solving the zero field case, we find that there are two additional quantum numbers $n_1$ and $n_2$, that are related to $n$ and $|m|$ by

$$n = n_1 + n_2 + |m| + 1 \qquad (2.20)$$

They are also related to $Z_1$ and $Z_2$ by

$$Z_1 = \frac{1}{n}\left(n_1 + \frac{|m|+1}{2}\right) \tag{2.21}$$

and

$$Z_2 = \frac{1}{n}\left(n_2 + \frac{|m|+1}{2}\right) \tag{2.22}$$

The wavefunctions themselves can be given in terms of associated Laguerre polynomials as

$$\psi_{n n_1 n_2 m} \propto e^{im\phi}\xi^{n_1+\frac{|m|}{2}}\eta^{n_2+\frac{|m|}{2}}e^{-\frac{(\xi+\eta)}{2n}} \tag{2.23}$$

using the reverse transformation equations (2.13), we obtain the electronic probability density in spherical coordinates[12]

$$|\psi_{n n_1 n_2 m}|^2 = r^{2n-2}(1+\cos\theta)^{2n_1+|m|}(1-\cos\theta)^{2n_2+|m|}e^{-\frac{2r}{n}} \tag{2.24}$$

The probability density is plotted for $n = 8, m = 0, n_1 - n_2 =$-7 to 7 in Fig. 2.5. Quite striking in this plot is that the extreme states ($n_1 - n_2 =$-7 and 7) are aligned parallel and anti-parallel with the applied field.

Using the zero field wavefunctions in (2.23), the first order energies are[12]

$$W_{n n_1 n_2 m} = -\frac{1}{2n^2} + \frac{3}{2}F(n_1 - n_2)n \tag{2.25}$$
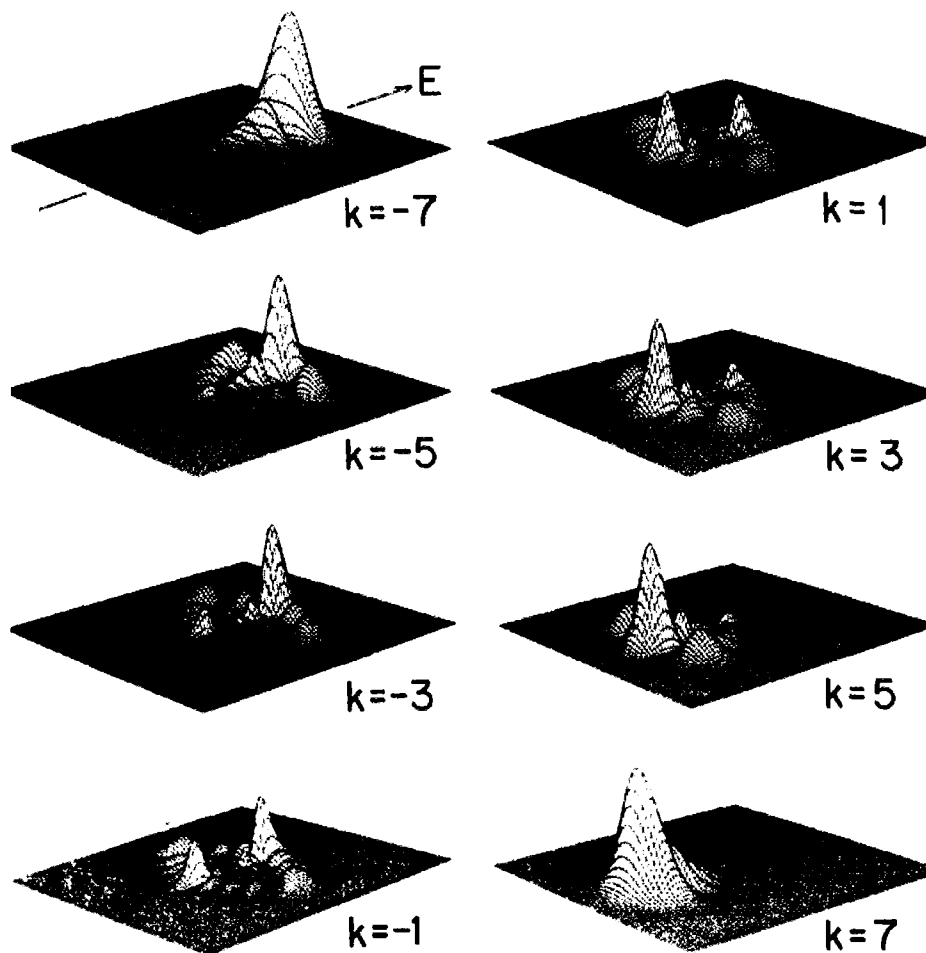
Figure 2.5 : Electron probability density plots for hydrogenic parabolic states at $n$=8

Interestingly, for states where $n_1 - n_2 = 0$ there is no first order Stark shift. Coincidentally, these are also the same states that have no net dipole moment. In addition, it is important to note that for each $n$ and $|m|$ state, there are $n - |m|$ Stark levels. If the perturbation calculation is taken to second order, the energies are[12]

$$W_{nn_1n_2m} = -\frac{1}{2n^2} + \frac{3}{2}F(n_1 - n_2)n - \frac{F^2}{16}n^4(17n^2 - 3(n_1 - n_2)^2 - 9m^2 + 19) \quad (2.26)$$
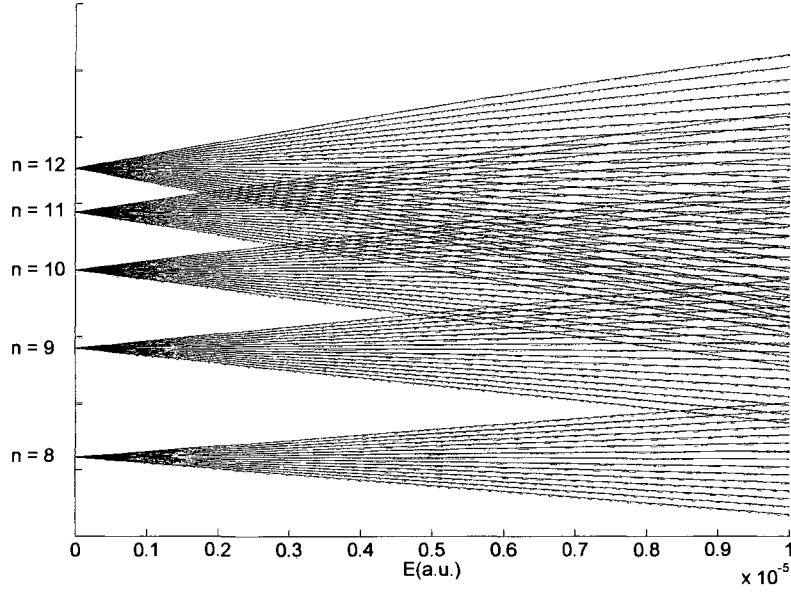


Figure 2.6 : Stark energy structure for $|m| = 1$ hydrogen

Figure 2.6 shows the Stark energy structure for hydrogen from $n = 8$ to 12, $|m| = 1$. To a good approximation, the energies vary linearly with field all the way to the point of ionization. This shows that the second order expansion, Eq. 2.26, is sufficient for most applications. Using the first order energy levels, Eq. 2.25, we find for a given value of $|m|$, that the spacing between adjacent Stark levels is given by[14]

$$\Delta W = W_{n,n_1,|m|} - W_{n,n_1-1,|m|} = 3nF \qquad (2.27)$$

Using the zero field energy level spacing of $\Delta W_{n \to n+1} \approx \frac{1}{n^3}$ and the first order Stark

energy, Eq. 2.25, we find that extreme members of adjacent manifolds cross at fields

of

$$F_{crossing} = \frac{1}{3n^5} \tag{2.28}$$

At $n = 350$, this crossing field corresponds to 326 $\mu$V/cm. Therefore, to selectively

excite states within the $n = 350$ Stark manifold, we must control the applied electric

field in the apparatus to less than $\sim$ 100 $\mu$V/cm. Although these level crossings

appear to violate the "no-crossing" theorem of Wigner and von Neumann, this is

not actually the case. The symmetry unique to the Coloumb potential allows levels

of identical $|m|$ to cross[15]. In alkali atoms, the core breaks this symmetry and in

general, states with the same value of $m$ do not cross.

### 2.2.2 Alkali Atoms in a Static Field

Alkali atoms behave very similarly to hydrogen atoms in an electric field. However,

there are some important differences due to the finite size of the ionic core. The

Hamiltonian for an alkali atom in the presence of an electric field in the z-direction

is given by

$$H = -\frac{\nabla^2}{2} + \frac{1}{r} + V_d(r) + Fz \tag{2.29}$$

where $V_d(r)$ is the potential due to the core. $V_d(r)$ is only non-zero close to the
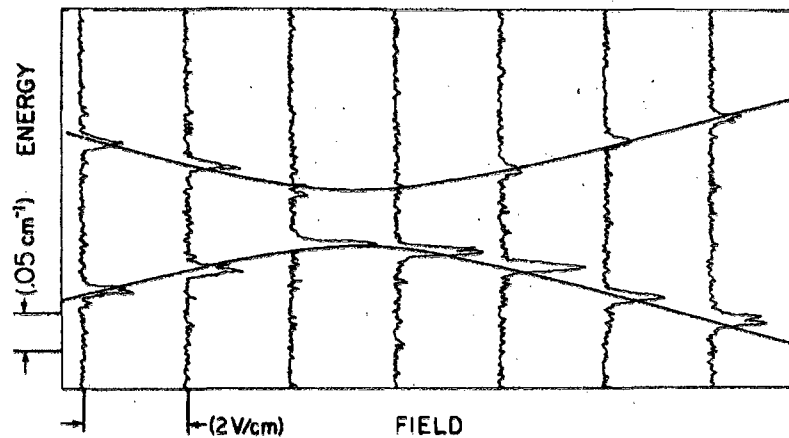
Figure 2.7 : Avoided crossing in Li of the $(n, n_1, n_2, |m|)$ states (18,16,0,1) and (19,1,16,1). The calculated energy level structure is superimposed on experimental excitation spectra. From ref. [14].

nucleus. One of the most important implications of adding the $V_d(r)$ term is that the parabolic quantum number $n_1$ is no longer a good quantum number, which is of course not the case in hydrogen. One of the results of this is that the red and blue states are now coupled due to overlap near the core. As a result, red and blue shifted Stark states from adjacent $n$ manifolds no longer cross, but instead exhibit avoided crossings as seen in Fig. 2.7.

There is no direct analytical solution for the Shrodinger equation with the Hamiltonian (2.29). In addition, the perturbation expansion is asymptotic and nonconvergent. However, the problem can be solved using a direct numerical matrix diagonalization technique using the zero field $nlm$ spherical states as a basis[14]. Figure 2.8 shows the results of such a calculation for potassium in the vicinity of $n = 15$.
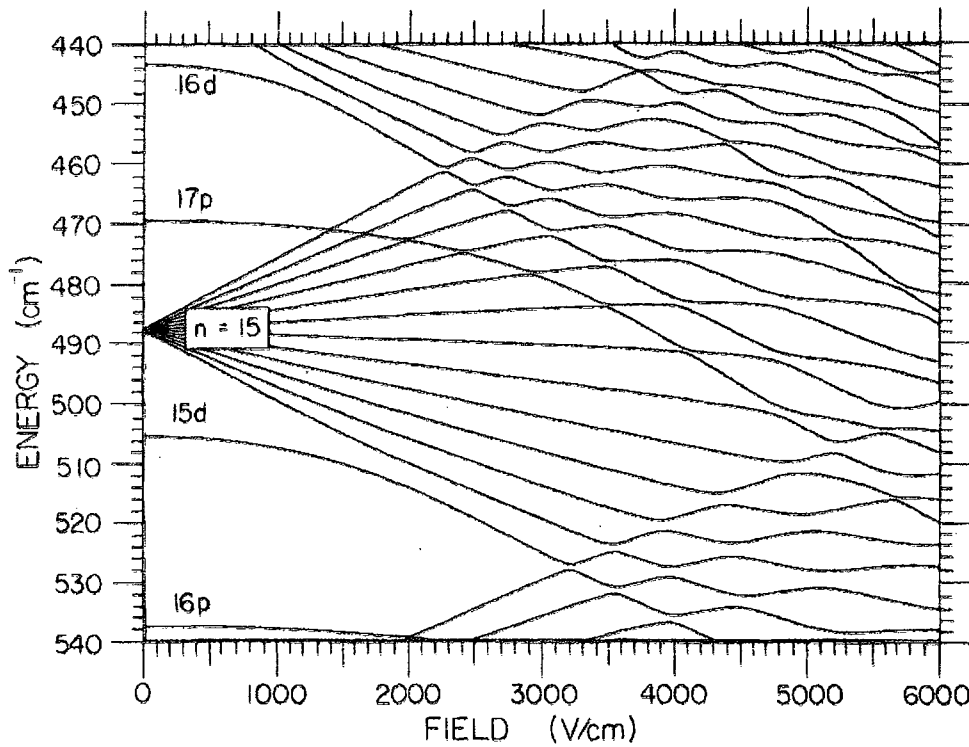
Figure 2.8 : Stark energy structure for $|m| = 1$ potassium near $n = 15$. From ref. [14]

## 2.2.3   Pulsed Field Ionization

**Adiabatic and Diabatic Ionization**

The ionization due to pulsed electric fields has been the subject of much investigation[16, 17]. This is due in part to the efficiency and selectivity in which field ionization can be employed as a detection method for Rydberg atoms. The most simplistic analysis results from the combined Coulomb-Stark potential

$$V = -\frac{1}{r} + Fz \tag{2.30}$$

which has a saddle point on the z-axis at $z = -\frac{1}{\sqrt{F}}$ as illustrated in Fig. 2.3. At the saddle point, the potential has the value $-2\sqrt{F}$. Thus if if the atom has a binding energy, $W$, then ionization will occur at a field of

$$F = \frac{W^2}{4} \tag{2.31}$$

If we ignore the Stark shift and use $W = -1/2n^2$, we obtain the classical ionization threshold

$$F = \frac{1}{16n^4} \tag{2.32}$$

Although this approach completely ignores the Stark energy shift and the possibility of tunneling through the barrier, it is still quite useful in determining the order of magnitude at which field ionization is expected.

As the value of $|m|$ increases, the associated centrifugal barrier potential raises the threshold field. We can account for this by considering the fractional field change compared with the $|m| = 0$ state as follows[18]

$$\frac{\Delta F}{F} = \frac{|m|\sqrt{W}}{\sqrt{2}} = \frac{|m|}{2n} \tag{2.33}$$

We can further improve the accuracy of (2.32) for red shifted Stark states simply by inserting the first order shift into (2.31). The result of doing so is[7]

$$F = \frac{1}{9n^4} \qquad (2.34)$$

All of the above formulas rely on a simple over the barrier picture. However, tunneling through the barrier usually blurs the concept of a true "threshold" field. There have been accurate calculations of ionization rates which take this into account[19, 20, 21].
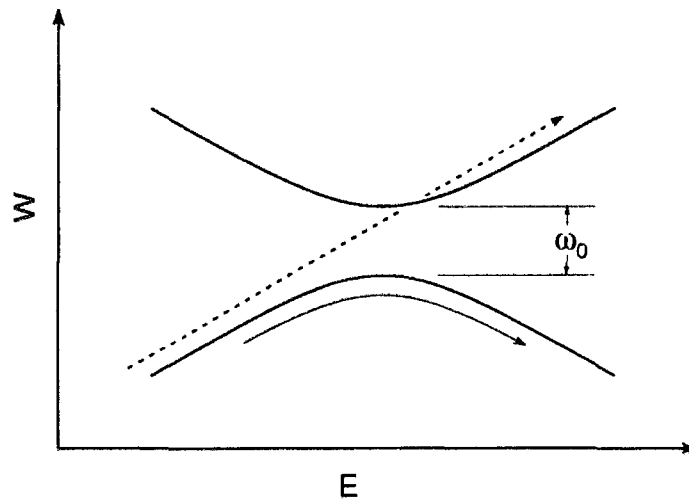


Figure 2.9 : Stark levels at an avoided crossing showing adiabatic(solid arrow) and diabatic(broken arrow) passage. From ref.[7]

When a field ionization pulse is applied, there are two possible ionization paths. As the applied field increases, the Stark state in question will eventually approach an avoided crossing, $\omega_0$, with the adjacent manifold. If the applied field is slewed through the crossing over a time long compared to $1/\omega_0$ the passage with be adiabatic. But, if the applied field is slewed quickly through the crossing, the passage

will be diabatic. In general, adiabatic ionization ionization occurs at lower fields than diabatic ionization[7].

**Impulsive Ionization**

While the ionization of Rydberg atoms by pulsed electric fields has been studied extensively, in the majority of these studies, the rise time and width of the applied pulses are greater than the classical Kepler orbital period of the Rydberg electron, $T_n$, given by

$$T_n = (1.5 \times 10^{-16})n^3 s \tag{2.35}$$

where $n$ is the principal quantum number. In the slowly varying regime, ionization results from over the barrier escape and tunneling through the barrier. From Eq. 2.32, we see that the threshold field decreases rapidly with increasing $n$, scaling as $1/n^4$. However, application of a very short electric-field pulse with duration $T_p < T_n$ lowers the Coulomb barrier only briefly, limiting electron escape. However, ionization can still occur if the impulse delivered to the electron by the pulsed field is sufficient to increase its energy by more than its original binding energy. As a result, the $n$ scaling of the ionization threshold field crosses over from the $1/n^4$ dependence characteristic of "long-pulse" ionization to a $1/n$ dependence in the limit of ultrashort pulses, $T_p \ll T_n$ [22, 23].

The application of such an ultra-short pulse leads to an impulsive momentum,

$\Delta\vec{p}$, transfer to the excited electron given by

$$\Delta\vec{p} = -\int_{-\infty}^{\infty} \vec{F}(t)dt \tag{2.36}$$

where $\vec{F}(t)$ is the time varying applied electric field. If the atom is initially in some stationary Rydberg state $|\phi_i\rangle$, the electronic wavefunction immediately after application of the pulse can be written

$$|\psi(t = 0)\rangle = |\phi_i^B\rangle = e^{i\Delta\vec{p}\cdot\vec{r}}|\phi_i\rangle \tag{2.37}$$

which corresponds to the initial state shifted in momentum space by $\Delta\vec{p}$. The resulting expectation values for energy and momentum are[10]

$$\langle E\rangle_{t=0} = \langle\phi_i^B|H_{at}|\phi_i^B\rangle = \langle\phi_i|H_{at}|\phi_i\rangle + \frac{(\Delta p)^2}{2} + \langle\phi_i|\vec{p_e}\cdot\Delta\vec{p}|\phi_i\rangle \tag{2.38}$$

$$\langle\vec{p_e}\rangle_{t=0} = \langle\phi_i^B|\vec{p_e}|\phi_i^B\rangle = \Delta\vec{p} + \langle\phi_i|\vec{p_e}|\phi_i\rangle \tag{2.39}$$

where $H_{at}$ is the atomic Hamiltonian and $\vec{r}$ and $\vec{p_e}$ are the electron momentum and position operators, respectively. Classically, the application of an ultra-short pulse to an electron with momentum $\vec{p_e}$ and position $\vec{r}$ leads to a final energy of

$$E(t = 0) = E_{n_i} + \frac{(\Delta p)^2}{2} + \vec{p_e}\cdot\Delta\vec{p} \tag{2.40}$$

where $E_{n_i}$ is the initial energy of the electron. We can easily re-write (2.40) as an expression for the energy transfer, $\Delta E$, as follows

$$\Delta E = E(t = 0) - E_{n_i} = \frac{(\Delta p)^2}{2} + \vec{p_e} \cdot \Delta \vec{p} \qquad (2.41)$$
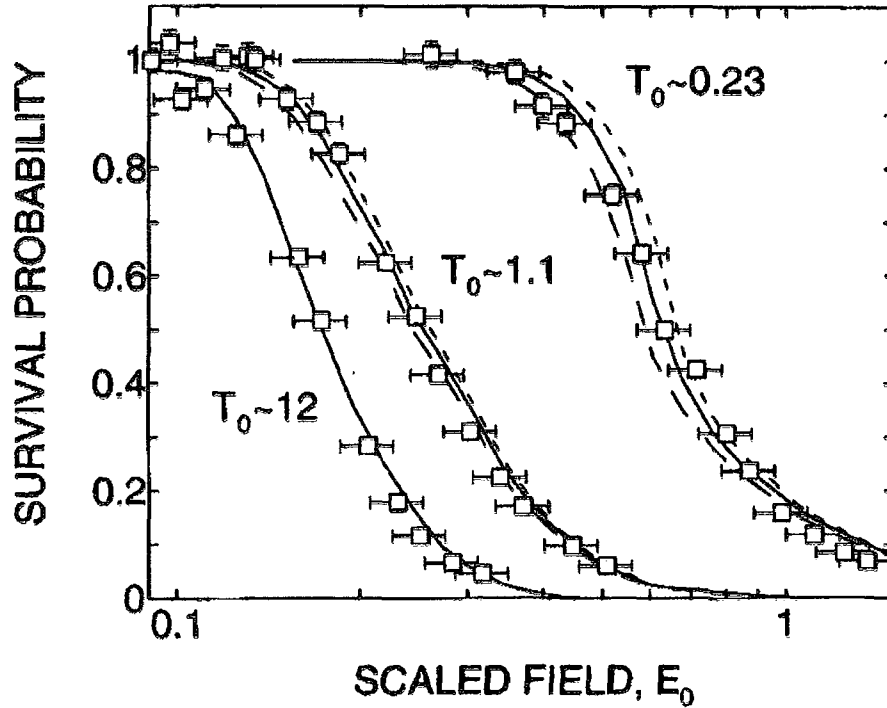


Figure 2.10 : Calculated and experimental survival probabilities as a function of the scaled pulse field amplitude $F_0 = n^4 F$ for different $T_0 = T_p/T_n$. From ref [9].

If the energy transfer, $\Delta E$, is greater than the initial binding energy of the electron, then ionization will occur. The ionization profiles for several different scaled pulse widths, $T_0 = T_p/T_n$, are shown in Fig. 2.10. Notice that as $T_0$ decreases to the impulsive limit ($T_0 \ll 1$), the ionization profile becomes much steeper.
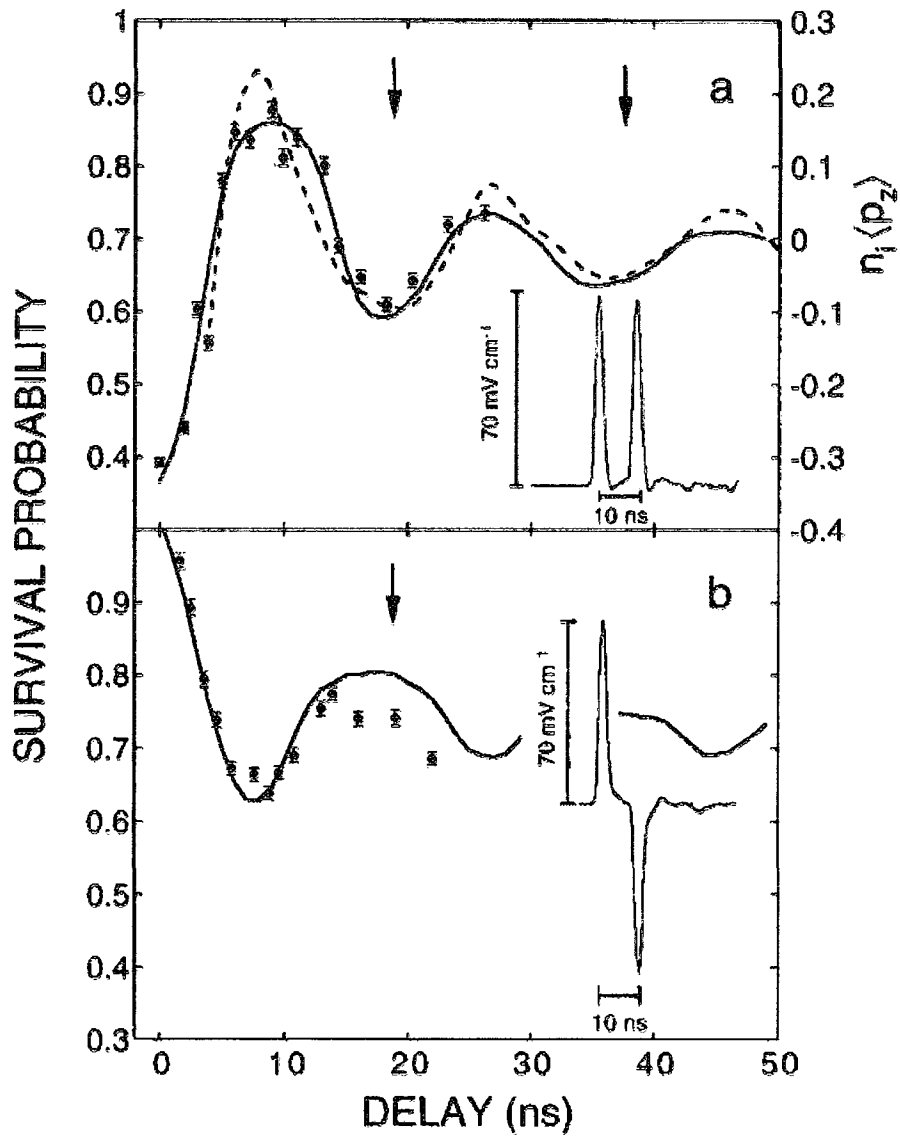
Figure 2.11 : Rydberg atom survival probability following application of two pulses in (a) the same and (b) opposite directions to K atoms with $n_i \sim 417$ as a function of time delay. From ref [10].

The use of slowly varying fields for ionization of Rydberg atoms yields information

about the excited state distribution since the ionization threshold depends strongly

on $n$. The use of an ultra-short pulse for ionization, however, allows one to probe the time evolution of a wavepacket. Equation (2.41) shows that the energy transferred by an ultra-short pulse depends directly on the initial momentum of the electron. If a relatively large pulse is used, $\frac{\Delta \vec{p}}{n_i \vec{p_e}} = 0.5$, variations in the electron momentum will appear as variations in the measured survival probability. An example of this procedure is demonstrated in Fig. 2.11.

## 2.3    Quantum-Classical Correspondence and the CTMC model

The classical orbits described in section 2.1 are not equivalent to quantum mechanical wavefunctions. As the principal quantum number, $n$, of a Rydberg atom increases, the atomic dimensions eventually become greater than the deBroglie wavelength associated with the electron. Thus we would expect a particle-like classical model to become an increasingly valid description. This is the essence of classical-quantum correspondence. However, even at the very-high-$n$ levels, the Rydberg atoms discussed in the present work are still quantum systems, whose properties and dynamics are completely described by the time dependent Schrödinger equation

$$i\hbar \frac{\partial \psi}{\partial t} = \left( -\frac{\hbar^2}{2m} \nabla_r^2 + U(\vec{r}, t) \right) \psi \tag{2.42}$$

where $U(\vec{r}, t)$ is the time dependent potential, and $\psi(\vec{r}, t)$ is the usual complex valued wavefunction. Even though the above equation fully describes the system in question, its solution at very-high-$n$ can be exceedingly difficult if not impossible given current

available computing power and numerical techniques. However, insights into the behavior of high-$n$ systems can be obtained using classical or semi-classical methods.

Many classical approximation techniques have been pioneered[24, 25, 26], mostly in the field of ion-atom collisions. Among these, the most successful approximation has been the classical trajectory Monte Carlo(CTMC) method first introduced by Arbines and Percival[8]. In general, the CTMC method employs an initial classical microcannonical ensemble which reproduces the quantum density distribution in position and momentum.

## Development of the CTMC Method

We begin by considering a fluid dynamical interpretation of the Schrödinger equation for one-electron systems[27]. In this alternative and equivalent quantum mechanical description, the *complex* wavefunction $\psi(\vec{r}, t)$ is replaced by a *real* probability density in phase space, $f_q(\vec{r}, \vec{p}, t)$. This phase space distribution function is obtained as a Weyl transform of the density matrix, $\mathbf{D}$, which leads to the Wigner probability density

$$f_q(\vec{r}, \vec{p}, t) = h^{-3} \int d^3 q e^{i\vec{p}\cdot\vec{q}/\hbar} \langle \vec{r} - \vec{q}/2 | \mathbf{D} | \vec{r} + \vec{q}/2 \rangle$$

$$f_q(\vec{r}, \vec{p}, t) = h^{-3} \int d^3 q e^{i\vec{p}\cdot\vec{q}/\hbar} \psi(\vec{r} - \vec{q}/2) \psi(\vec{r} + \vec{q}/2) \tag{2.43}$$

The time evolution of $f_q$ is governed by the Weyl transform of the Von Neumann equation for the density matrix. This leads to the quantum Liouville equation[28, 29]

$$\frac{\partial f_q}{\partial t} = L_q f_q = -\vec{p} \cdot \frac{\partial f_q}{\partial \vec{r}} + \frac{2}{\hbar} \sin\left(\frac{\hbar}{2} \frac{\partial}{\partial \vec{p}} \cdot \frac{\partial}{\partial \vec{r}}\right) f_q U \tag{2.44}$$

where $L_q$ is the quantum Liouville operator. If $L_q$ is simply replaced with the classical Liouville operator, $L_c$, not surprisingly, this leads to the classical Lioville equation[27]

$$\frac{\partial f}{\partial t} = L_c f = [H, f] \tag{2.45}$$

where $[,]$ denotes a Poisson bracket, and $H$ is the time dependent Hamiltonian. While the quantum and classical Liouville equations are not equivalent, they are entirely analogous. Just as in the quantum formalism, the classical Liouville equation governs the time evolution of the phase space distribution function, $f$. However, in the classical case, the points in phase space evolve independently in time allowing for a direct numerical integration.

The largest challenge to this approach is in constructing the initial ensemble. For computational purposes, a discrete number of random points must be chosen to represent the continuous phase space distribution, $f$. Each individual phase space trajectory alone does not have any specific meaning. Only the total ensemble of trajectories determines the values of the observable quantities. There does not exist a unique initial phase distribution which mimics the initial quantum state. However, we adopt the most common choice which is the microcannonical ensemble

$$f_i(\vec{r}, \vec{p}) = C_i \delta \left[ E_i - \frac{p^2}{2} - V_{at}(\vec{r}) \right] \mho_i \tag{2.46}$$

where $C_i$ is a normalization constant, $E_i$ is the initial quantum mechanical binding energy, and $\mho_i$ is a characteristic function representing the other quantum numbers of the initial state. For a hydrogenic spherical state $|n_1, l_i, m\rangle$ [30]

$$\mho_{l_i, m_i} = \Theta(L - l_i)\Theta(l_i + 1 - L)\Theta\left(L_z - \frac{L(2m_i - 1)}{2l_i + 1}\right)\Theta\left(\frac{L(2m_i + 1)}{2l_i + 1} - L_z\right) \tag{2.47}$$

where $\vec{L} = \vec{r} \times \vec{p}$ is the classical angular momentum and $\Theta$ denotes a step function. In addition, for a hydrogenic parabolic state with the quantum numbers $n_i, n_{1i}, n_{2i}$

$$\begin{aligned}
\mho_{n_{1i}, n_{2i}} = {} & \Theta\left(N_1^c - n_{1i} + \frac{1}{2}\right)\Theta\left(-N_1^c + n_{1i} + \frac{1}{2}\right) \\
& \times \Theta\left(N_2^c - n_{2i} + \frac{1}{2}\right)\Theta\left(-N_2^c + n_{2i} + \frac{1}{2}\right)
\end{aligned} \tag{2.48}$$

where

$$N_{1,2}^c = \frac{1}{2}[n_i(1 \mp A_z) - (|L_z| + 1)] \tag{2.49}$$

where $\vec{A}$ is the Runge-Lenz vector. After propagating the initial classical state, $f_i$, all of the relevant observables (i.e. energy, position, momentum, angular momentum, etc) can be extracted from the final statistical ensemble. Survival probability can be calculated by considering the ratio of phase trajectories that remained bound ($E_{final} < 0$) to the total size of the initial ensemble as follows
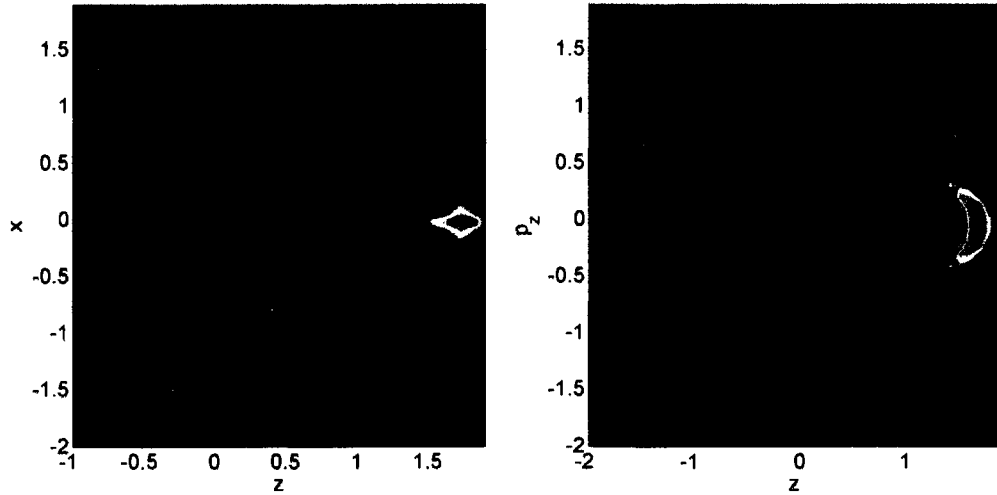
Figure 2.12 : Phase space distribution, $f$, for the initial parabolic state. (a) Spatial probability density projected onto the $x, z$ plane. (b) Poncaré section in the $z, p_z$ plane.

$$P_{survival} = \frac{\text{Number of trajectories with a negative energy at time t}}{\text{Total number of trajectories in initial ensemble}} \qquad (2.50)$$

## Limitations of the CTMC method

The CTMC method has been shown to accurately reproduce the dynamics of atomic wavepackets even for relatively low-lying states ($n < 10$) [31]. But, the method is an approximation and has limitations. At longer evolution times, the classical and quantum dynamics begin to diverge. This breakdown time is governed by the

Heisenberg time

$$t_{Heisenberg} = \frac{\hbar}{\langle \Delta E \rangle} \qquad (2.51)$$

For Rydberg atoms, the energy spacing scales as $\sim 1/n^3$ and becomes quite small. Thus, the breakdown time becomes quite large allowing CTMC modeling of very-high-$n$ wavepackets for an extended period, $\sim 1\mu s$ at $n \sim 300$.

## 2.4 Classical Scaling Invariance

The values shown in table 1.1 can be computed easily based on classical scaling invariance. Each parameter shown for different levels of $n$ can be reduced to a common reference value normalized to $n = 1$. It has been demonstrated that the classical equations of motion are invariant under the scaling transformation[8, 26]

$$\vec{r} = n^2 \vec{r_0} \qquad (2.52)$$

$$t = n^3 t_0 \qquad (2.53)$$

where $\vec{r_0}$ and $t_0$ are now the scaled parameters. We can extend this transformation using the definition of momentum as follows

$$\vec{p} = \left( \frac{d\vec{r}}{dt} \right) = \frac{n^2}{n^3} \left( \frac{d\vec{r_0}}{dt_0} \right) = \frac{1}{n}\vec{p_0} \quad \Rightarrow \quad \vec{p_0} = n\vec{p} \qquad (2.54)$$

Continuing this procedure for the angular momentum $\vec{L}$

$$\vec{L} = \vec{r} \times \vec{p} = (n^2 \vec{r_0}) \times \left(\frac{\vec{p_0}}{n}\right) = n\vec{r_0} \times \vec{p_0} \quad \Rightarrow \quad \vec{L_0} = \frac{\vec{L}}{n} \tag{2.55}$$

Continuing the transformation for the remaining relevant parameters and summarizing the previous results, we find

$$E_0 = n^2 E$$

$$t_0 = \frac{t}{n^3}$$

$$\vec{r_0} = \frac{r}{n^2}$$

$$\vec{p_0} = n\vec{p} \tag{2.56}$$

$$\vec{L_0} = \frac{\vec{L}}{n}$$

$$\vec{F_0} = \frac{\vec{F}}{n^4}$$

$$z_0 = \frac{z}{n^2}$$

Applying the above transformation to the atomic Hamiltonian, we find

$$H(\vec{r}, \vec{p}, t) = \frac{p^2}{2} - \frac{1}{r} = \frac{p_0^2}{2n^2} - \frac{1}{r_0 n^2} = \frac{1}{n^2} H_0(\vec{r_0}, \vec{p_0}, t) \tag{2.57}$$

where $H_0$ is now the invariant Hamiltonian. Under this tranformation, initial ensembles with different energies, along with the associated dynamics, become identical. This is useful for comparing the behavior of Rydberg atoms in different energy levels, and for testing quantum-classical correspondence, because quantum corrections break the scaling invariance[32]. Scaled parameters are used throughout this work and are denoted by the subscript 0.

## 2.5  Quasi-One Dimensional Rydberg Atoms

The Rydberg atom is a three dimensional system. However, if the probability density of the electron can be confined to a single dimension, not only would the resulting dynamics be greatly simplified but the resulting atoms would form an excellent starting point for further studies of quantum control and manipulation. In principle, it is straightforward to create atoms which are nearly one-dimensional by exciting the extreme members of the Stark manifolds[12, 33]. As shown in Fig. 2.5, the extreme members of the Stark manifold have large permanent electric dipole moments and are strongly polarized along the direction of the applied field. While these states are not entirely confined in one-dimension, they are a close approximation and are referred to as quasi-one-dimensional(quasi-1d or Q1-D) states. It is expected that the dynamics of these quasi-1D states will mimic that of true 1D atoms[34, 35].

The excitation of extreme members of a given Stark manifold as a method of producing quasi-1D atoms is simple in concept. However, the production of selected Stark states at high-$n(n > 100)$ remains a challenge because the oscillator strengths associated with their excitation are small, and because the Stark energy levels are closely spaced requiring the use of narrow-linewidth frequency-stabilized lasers and the minimization of Doppler effects.

Figure 2.13 gives an example of the calculated Stark energy level structure for potassium ($m = 0$) states in the vicinity of $n \sim 50$[36]. The essential features of the
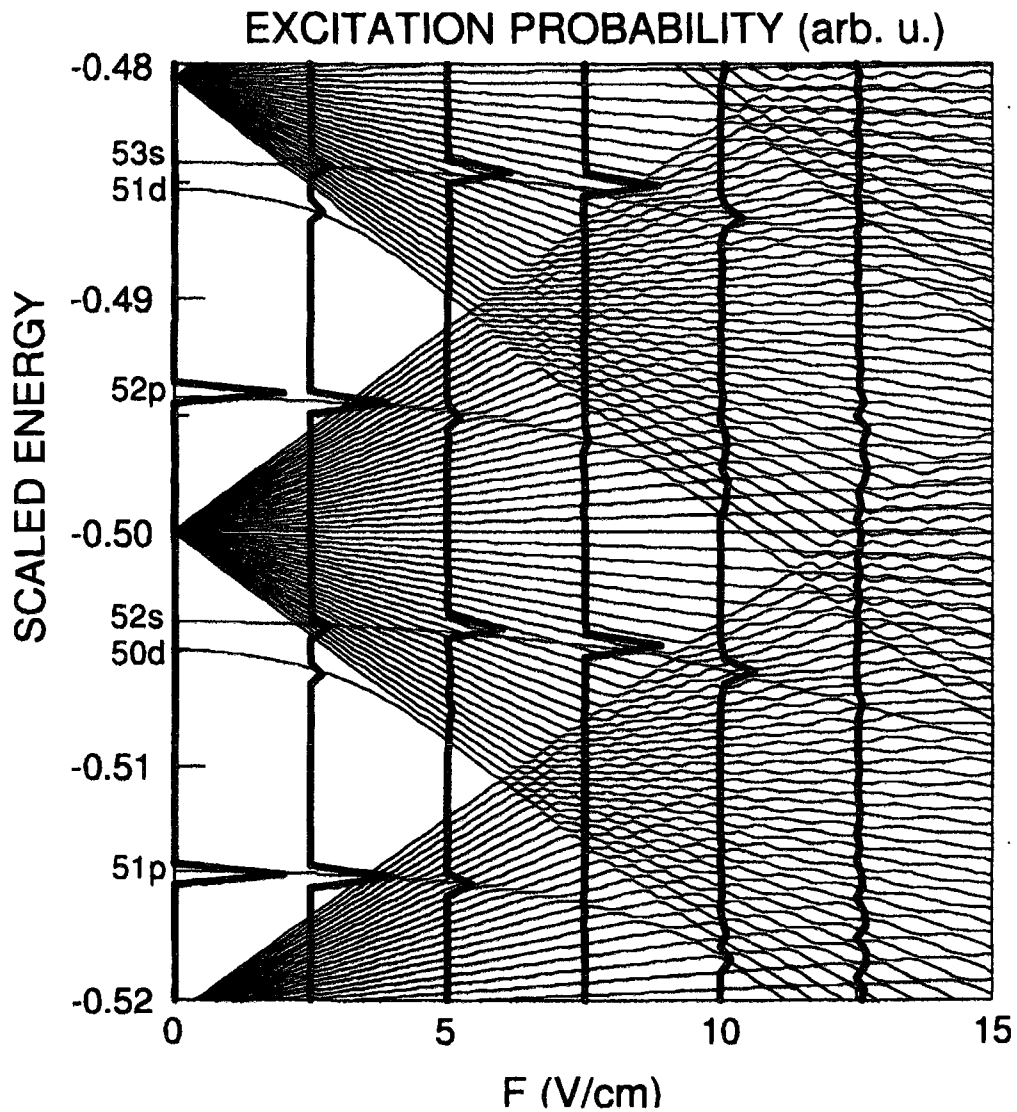
Figure 2.13 : Calculated Stark energy level structure for K($m = 0$) states near $n = 50$ (thin lines). Also included is the probability for photoexcitation from the ground state (thick lines) by a laser with a linewidth $\Delta\omega_L = 10^{-3}/n^2$ for several values of applied field.

Stark manifold are the same as for the $n \sim 300 - 350, m = 0$ states used in the present

work after re-scaling the energy by $n^2$ and field strength by $1/n^4$. Most importantly,

the positions of the low-$l$, $s, p$, and $d$ core-penetrating states relative to their adjacent Stark manifolds are invariant because the quantum defects are insensitive to $n$. As the strength of the applied field increases, these states begin to interact with states in the neighboring Stark manifolds. The $d$ state couples with states of the same $n$ and mixes strongly with the highly-polarized downhill states.

Experimentally, the probability of photoexcitation from the K (4s) ground state depends on the oscillator strengths. Figure 2.13 shows the calculated excitation probability for several values of applied electric field. The transitions obey the dipole selection rule $\langle n_f, l_f | z | n, l \rangle \sim \delta_{l,(l_f \pm 1)}$. As a result, only the $p$-state can be excited in zero field. As the applied field is increased, other low-$l$ states begin to couple to the $p$-state and to acquire $p$-like character. As the applied field approaches the manifold crossing field, the Stark shifted $s$ and $d$ states acquire significant excitation probability. Also, near the manifold crossing the $d$ state has become strongly polarized due to coupling with the neighboring downhill manifold states. This along with its modest excitation probability, makes the d state the best choice for experimentally producing quasi-1D atoms. The applied field used during excitation is thus the manifold crossing field given by Eq. (2.28).

While the above discussion is somewhat qualitative, the polarization of a given Stark state, $|f\rangle = |n, n_1, n_2\rangle$ can be quantified in terms of its scaled dipole moment along the $z$-axis. Since in scaled atomic units, the charge of the electron is unity, the
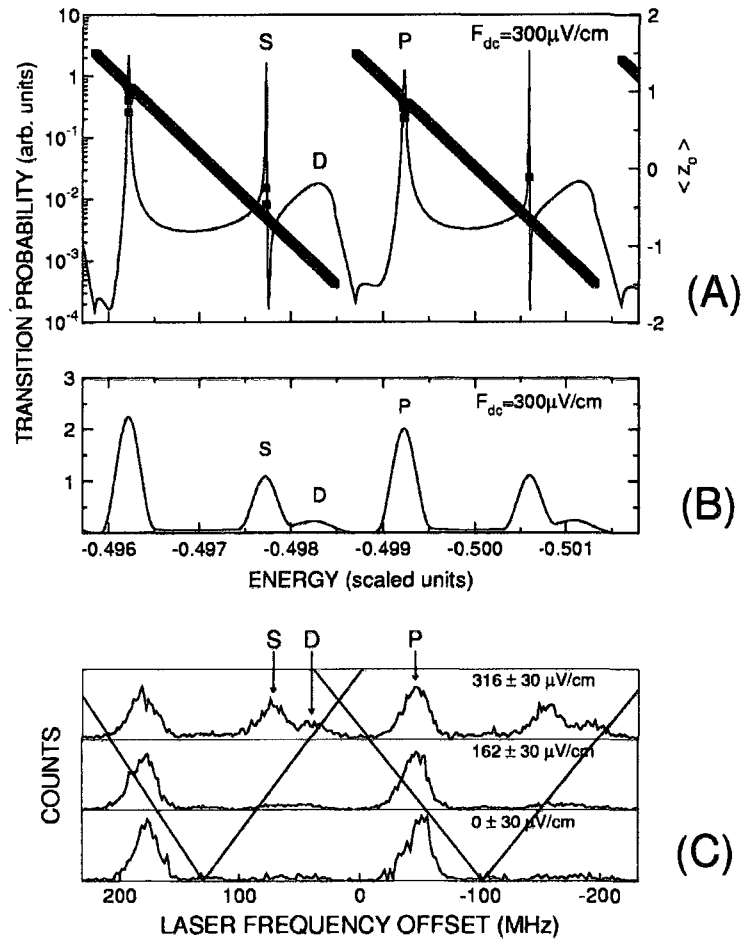
Figure 2.14 : Probability for photoexcitation of ground state of potassium atoms into $m = 0$ Stark states in the vicinity of $n = 350$: (A) calculation for an ultra narrow linewidth ($\Delta\omega_L = 0$) laser and $F_{dc} = 300\mu$ V/cm (thin line). (B) same as (A) but assuming an effective laser linewidth of $\sim 10$ MHz. (C) measured excitation spectra for several values of applied field. Also displayed in (A) are the z-components of the dipole moments for each excited state (heavy black lines). The thin lines in (C) indicate the position of the extreme members of the Stark manifold.

dipole moment is given by the scaled expectation value of the $z$-coordinate.

$$\langle z_0 \rangle = \langle f|z|f \rangle / n^2 \tag{2.58}$$

For large $n$ and $m = 0$, the dipole moment lies in the range $-1.5 < \langle z_0 \rangle < 1.5$. Figure 2.14 shows a detailed view of the Stark transition probabilities near the manifold crossing field. Also shown is the scaled dipole moment in the z-direction. Notice that the extreme value of the dipole moment corresponds to the position of the $d$-state. The actual values of the dipole moment for the $s$, $p$, and $d$ levels are -0.25, +0.7, and -1.25 respectively[36]. Also shown are several experimental excitation spectra.

The quasi-1D nature of these excited states can be examined experimentally by observing the asymmetry in ionization profiles when ultra-short pulsed fields are applied parallel and transverse to the weak DC excitation field. The results of such an experiment are demonstrated in Fig. 2.15. When probed transverse to the atomic axis a sharp decrease in survival probability with increasing kick strength is observed pointing to a narrow distribution of transverse momentum. When probed along the axis of orientation, the survival probability decreases much more slowly with increasing kick strength indicative of a much broader distribution of electron momenta parallel to the axis. Also shown, is the calculated spatial probability density of the final excited state, which, as expected, is strongly polarized along the $z$-axis. The excitation of these quasi-1D states is the first step in all of the following experiments.
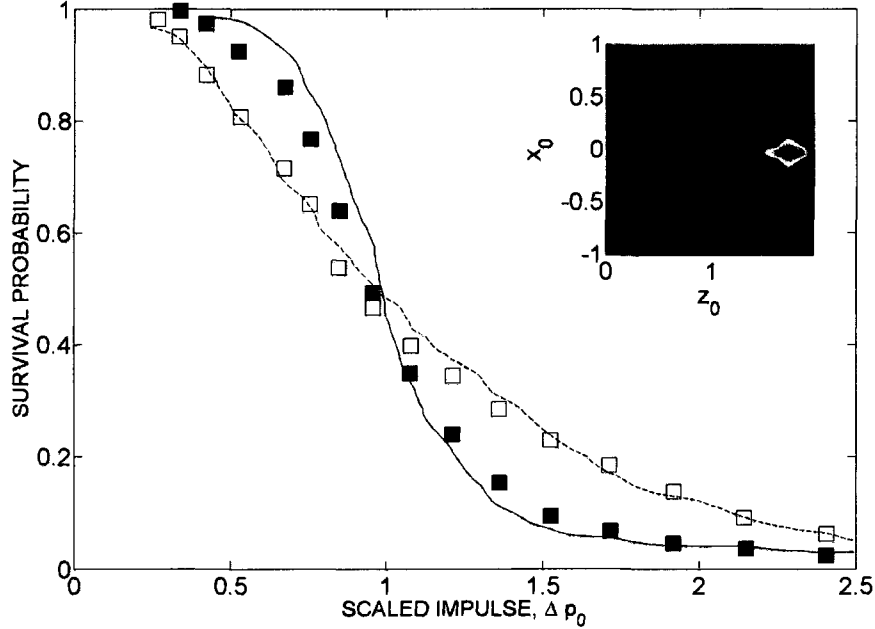
Figure 2.15 : Survival probabilities for $n_i \sim 350$ quasi-1D potassium atoms as a function of the scaled impulse $\Delta p_0$. The experimental data are for probe HCPs applied parallel (■) and transverse (□ ) to the atomic axis (see insets). The lines show the results of CTMC simulations. Also shown (inset) is the calculated spatial probability density of the quasi-1D state.

## 2.6 Phase Space Localization and Stable Islands

The present work is motivated by the increased interest in recent years to control and manipulate atomic wavefunctions[37, 38, 39]. The ease with which desired targeted final states can be produced is governed by the initial momentum and position distributions of the electron. In essence, the more tightly the initial state is localized in phase space the more straightforward it is to access some selected final state[40, 41, 42].

## 2.6.1 Transient Phase Space Localization
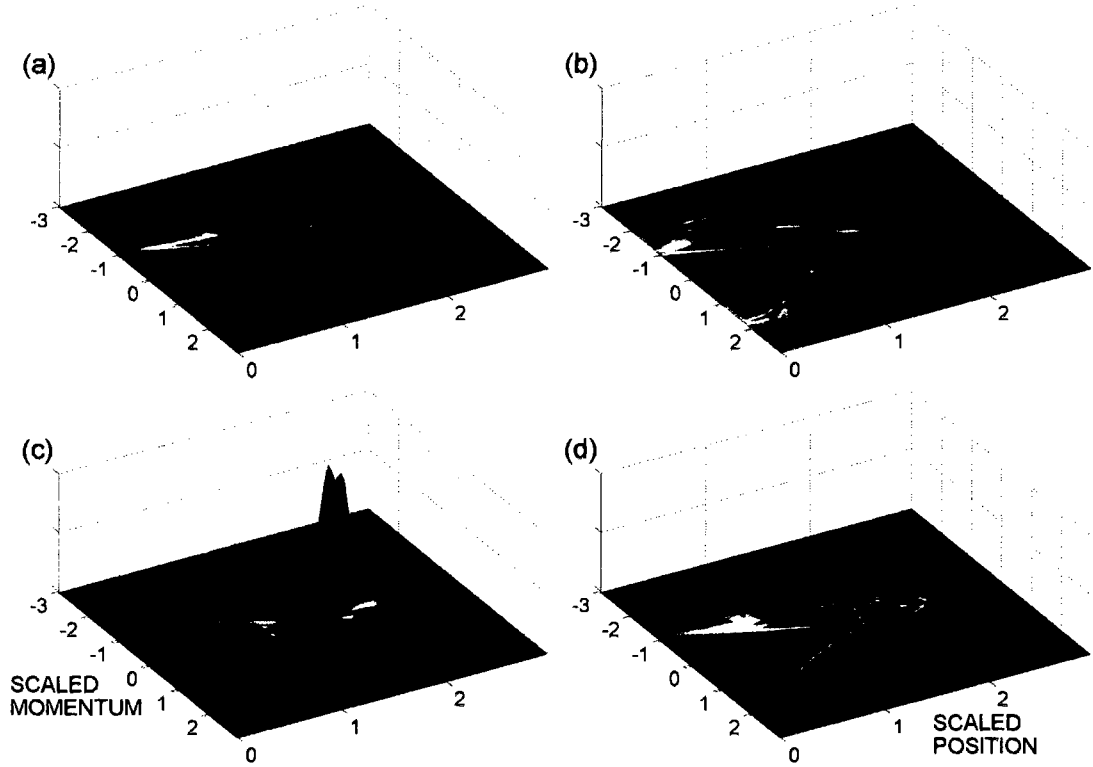


Figure 2.16 : Transient phase space localization of a quasi-1D atom. Phase space probability density (a)before the localization kick, (b)at the scaled time $t_0 = t/T_n = 1.5$, (c) at the time of optimum localization, $t_0 = 2$, (d) at equilibrium state, long after the pulse application.

It is possible to temporarily induce localization in phase space by applying a single HCP to a quasi-1D atom. The kick must be relatively small ($\Delta p_0 \lesssim 0.1$), and must be directed towards the nucleus. The kick produces a non-stationary wavepacket in phase space. Figure 2.16 shows the evolution of the wavepacket following the application of a kick with scaled impulse $\Delta p_0 = -0.085$ to a $n = 350$ quasi-1D atom. Frame (a) shows the initial quasi-1D state prior to application of the kick.

The probability density lies along the torus of constant energy associated with the $n = 350$ state. Frame (c) shows the wavepacket at the time of optimum localization. At this time, the wavepacket temporarily occupies a much smaller area in both z and momentum space, making this the optimum time to deliver additional pulses to further shape the wavepacket. Frame (d) shows the phase space distribution long after the localizing pulse. The state is now slightly broader and less defined due to the small energy transfer delivered by the localization kick. This is the penalty for temporarily confining the wavepacket.

The localization in phase space can be analyzed in more detail by considering the evolution of the $p_{z0}$ and $z_0$ distributions after the application of the localization pulse. These distributions are shown in Fig. 2.17. The first vertical line intersects the $p_{z0}$ distribution at the scaled time $t_0 = t/T_n = 2$. At this point the momentum distribution is squeezed to a width of less than 0.1 in scaled units.

## 2.6.2 The Periodically Kicked Rydberg Atom: Stable Islands in Phase Space

The above technique of achieving strong transient phase-space localization can be very useful for experimental atomic wavepacket engineering. However, the localized wavepacket quickly disperses once it passes the optimal localization time. Even though the scaled effective area occupied by the phase-space distribution oscillates during further time evolution, the degree of localization achieved subsequently is
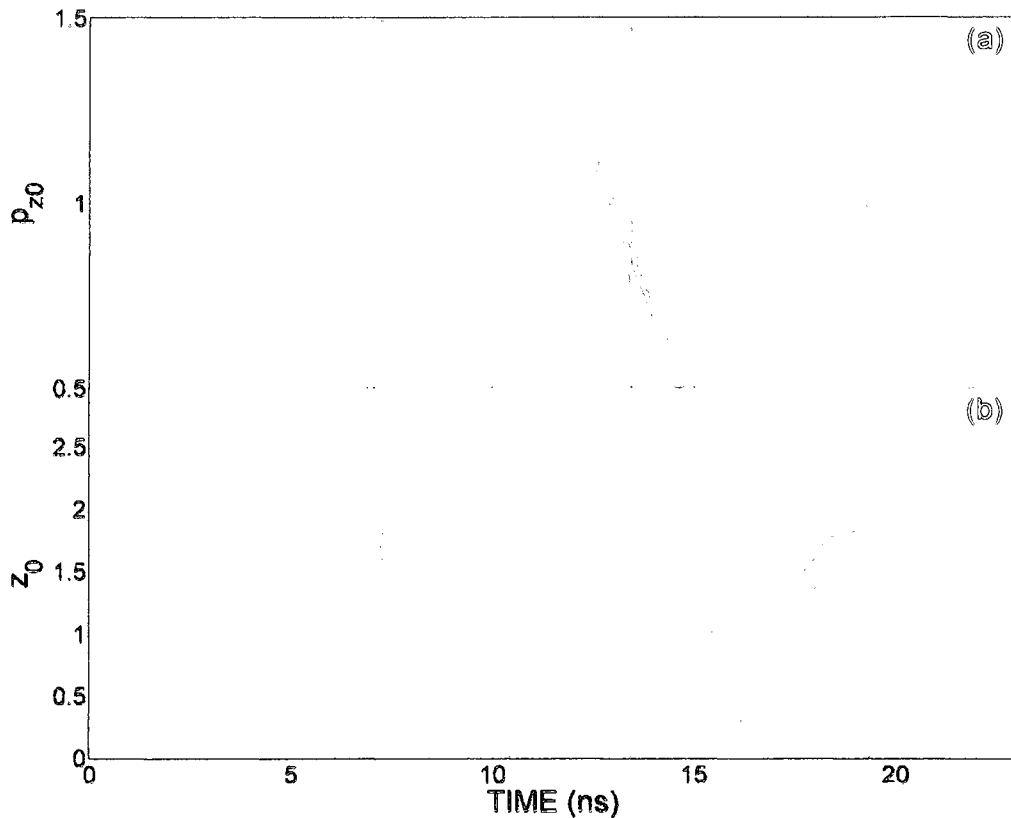
Figure 2.17 : Evolution of the (a)$p_{z0}$ and (b)$z_0$ distributions after application of a transient phase space localization pulse. The white vertical lines mark the scaled times $t_0 = 1$, 2 and 3.

never as tight. In real experimental environments, the wavepacket is dispersed even faster than predicted by theory due to the presence of noise and field inhomogeneities. Thus, in practice, there is only one scaled evolution time delay that can be used experimentally. To maintain transient phase-space localization for extended periods, dynamical stabilization, a technique to periodically trap a localized wavepacket in phase space must be used[43, 44, 34, 35].

Dynamical stabilization can occur when quasi-1D Rydberg atoms are exposed to

a train of identical equispaced HCPs with duration $T_p \ll T_n$. Each individual pulse, $\vec{F}_{HCP}(t)$, delivers an impulsive momentum transfer, or "kick" with strength

$$\Delta \vec{p} = - \int \vec{F}_{HCP}(t) dt \qquad (2.59)$$

to the electron[23]. The Hamiltonian for such a periodically kicked system can be written as

$$H = \frac{p^2}{2} - \frac{1}{r} - z\Delta \vec{} \sum_{k=1}^{N} \delta(t - kT) \qquad (2.60)$$

where $T$ is the period between HCPs in the train, and $N$ is the number of HCPs in the train. The resulting dynamics can be quite complicated, and is most easily analyzed by examining Poncare surfaces of sections in phase space. The objective of this type of analysis is to reveal areas in phase space that are stable and in which wavepackets can be trapped.

This analysis shows that, as expected, the resulting dynamics is quite sensitive to the period, amplitude, and direction of the applied pulse train. In particular, for kicks directed away from the nucleus, there are no stable regions present and the resulting dynamics is globally chaotic leading to rapid ionization through diffusion to the continuum. In the specific case for scaled frequency $\nu_0 = 1/T = 1.3$, and scaled impulse $|\Delta p_0| = 0.3$, this is demonstrated by the lack of structure in Fig. 2.18(b). However, when the pulses are directed toward the nucleus, $\Delta p_0 = -0.3$, the phase space structure, Fig. 2.18(a), is completely different. A series of stable closed tori, or
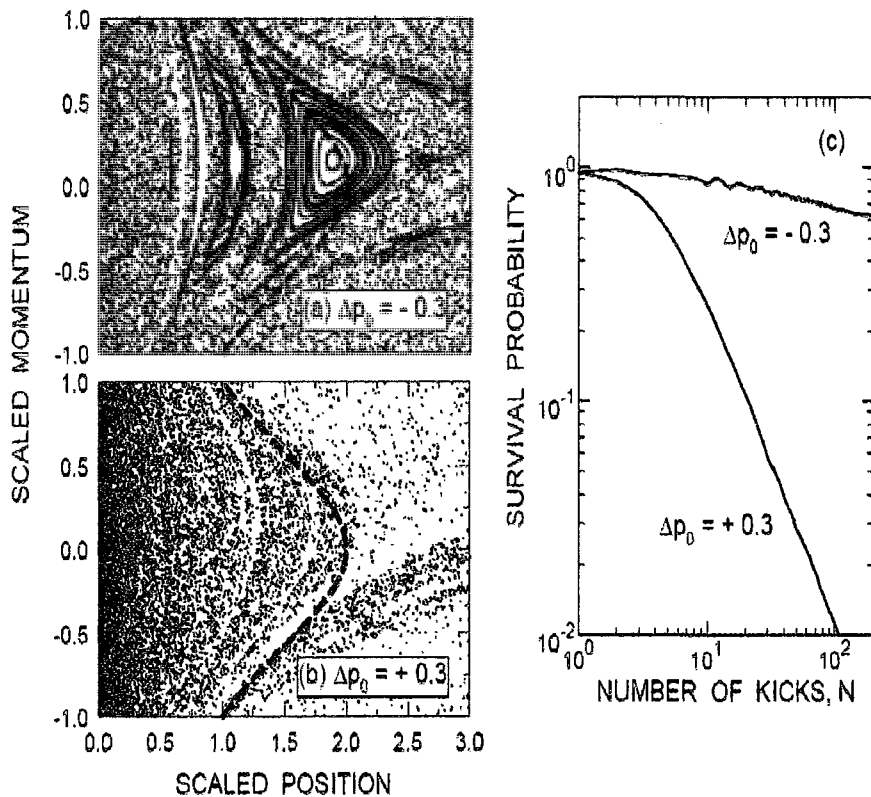
Figure 2.18 : Poincaré surfaces of section for the periodically kicked quasi-1D Rydberg atom with scaled frequency $\nu_0 = 1.3$ and scaled impulse $|\Delta p_0| = 0.3$. (a) kicks directed toward the nucleus ($\Delta p_0 = -0.3$) and in (b) kicks directed away from the nucleus (($\Delta p_0 = +0.3$)). In (a) and (b), the dashed lines show the position of the initial state. (c) Survival probability as a function of the number, $N$, of pulses toward and away from the nucleus.

"islands" are embedded in the chaotic sea. In addition, there is considerable overlap between these islands and the position of the initial state in phase space. This result is of great significance because those electrons whose initial phase-points lie within the stable region will remain trapped. This trapping in phase space leads to dynamical stabilization.

The most striking signature of dynamical stabilization is that the rate of diffusion into the continuum, or ionization, is suppressed as long as the electron remains trapped in the stable region in phase space. Figure 2.18(c) shows the survival probability as a function of the number of pulses, $N$, for HCP trains directed toward and away from the nucleus. As the number of pulses is increased, the fraction of electrons that are ionized is dramatically higher for those that were exposed to kicks away from the nucleus. For kicking towards the nucleus some electrons are stabilized and survival probability remains high even after a large number of pulses.

Dynamical stabilization is very critical in the present work. As will be discussed later in more detail, for example, once transient phase-space localization is achieved it can be recovered periodically by positioning the localized state atop a stable island associated with a subsequent periodic HCP train. In this manner, transient phase-space localization can be maintained for an extended period. Furthermore, by adjusting the parameters of the periodic HCP train, we can navigate the trapped localized wavepacket to different regions in phase space, offering a powerful tool for performing atomic wavepacket engineering.

# Chapter 3

# Experimental Apparatus and Techniques
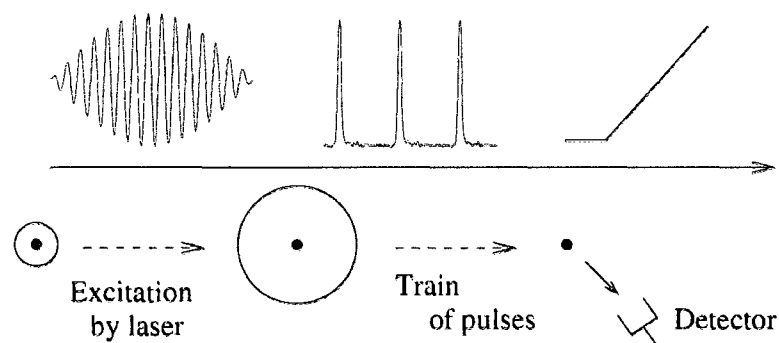


Figure 3.1 : The timing sequence for a typical experiment: (1)Photoexcitation to Rydberg level, (2) Application of HCPs, and (3) Application of field ionization ramp for detection.

Potassium atoms contained in a collimated thermal-energy beam are photoexcited to selected high-$n$ Rydberg states by an extra-cavity doubled tunable CW dye laser. Excitation occurs near the center of an interaction region composed of three pairs of copper electrodes which are independently biased to minimize stray electric fields. The laser output is formed into a series of pulses of $\sim$1-2 $\mu$s duration by an acousto-optic modulator (AOM). Immediately following the laser pulse, Rydberg atoms are subjected to a sequence of one or more half-cycle electric field pulses (HCPs). Following a delay of $\sim$5-10 $\mu$s, the number and $n$-state distribution of the surviving

Rydberg atoms is determined by selective field ionization (SFI), in which a linearly increasing ionization field is applied. Any electrons produced by field ionization are accelerated to and detected by a channel electron multiplier. Measurements in which no HCPs are applied are interspered uniformly throughout the data acquisition cycle to monitor the number of Rydberg atoms initially created by laser excitation. The survival probability is determined by calculating the ratio of electrons detected with and without HCPs.

## 3.1   Vacuum System

The vacuum system consists of two connected, differentially-pumped stainless steel chambers. The regions are referred to as the source chamber and the main chamber. The smaller source chamber contains a potassium oven that is surrounded by a water cooled enclosure. This chamber is pumped by a 4" Varian diffusion pump, and is separated from the main chamber by a 0.5mm aperture which allows the potassium beam to enter the main chamber while minimizing contamination. The main chamber contains the interaction region where Rydberg atoms are created, studied, and then field ionized. It is pumped by a single 6" diffusion pump.

A combination of mechanical and diffusions pumps is used to exhaust the chambers. The pressure in both chambers is monitored using a TK-150 Bayard-Alpert type ionization gauge. The pressure in the main chamber during experimental operation is typically below $1 \times 10^{-7}$ torr. The laser beam enters and exits the main chamber

through quartz windows set at Brewster's angle.

## 3.2  Potassium Beam Oven

The atom of choice for the present work is potassium. The main advantages of using potassium in this role are twofold. First, its electronic configuration is relatively simple, with a quasi-hydrogenic valence electron orbiting a noble gas like core. Second, becuase of its relatively low ionization potential of 4.34 eV, the wavelengths of light necessary to excite it from the ground state to the Rydberg levels are readily achievable using commercially available frequency-doubled rhodamine 6G dye lasers.

The oven is essentially a two piece stainless steel enclosure, inside which is sealed a 5-gram ampoule of potassium. A 0.020" diameter laser drilled collimating exit aperature is mounted to the front of the oven, and is aptly referred to as the "nose". The oven is heated to ~300°C using six cartridge type resistive heating elements. Four of these heaters are embedded in the main body of the oven with the remaining two in the nose. Each of these two groups of heaters is independently controlled. The temperatures of the main oven and the nose are measured independently using thermocouples. A temperature gradient of 30°C is maintained between the nose and body to prevent potassium from condensing on the nose and clogging the aperature.

The entire oven is enclosed in a water-cooled copper shield. This arrangement prevents the radiative transfer of heat from the oven to main chamber. In addition,

the vacuum chamber is kept relatively clean because the heated potassium vapor condenses readily onto the inside surface of the copper jacket. After exiting the nose aperture, the potassium beam passes through a second 0.5 mm diameter collimating apperture resulting in a beam diverge of less than 0.5°. The beam flux is measured using a hot tungsten wire ionization detector. The density of beam estimated to the be $\sim 10^8/cm^3$, with an average thermal velocity of $\sim$500m/s. There are two potassium isotopes present in the beam in natural abundance (93.3% $^{39}K$, 6.7% $^{41}K$).

## 3.3 Laser System

The wavelength required to excite the potassium 4s ground state to a Rydberg state with $n$ $\sim$350 is 2856.4 Å. Wavelengths in this range can be generated by a frequency-doubled Rhodamine 6G dye laser. The laser system employed in this work is a Coherent 699-21 single frequency dye laser pumped by 7.5W of 532 nm light from a Verdi V8 solid state laser. The typical output power from the dye laser is $\sim$ 1W. Its output beam is directed into a Spectra-Physics Wavetrain tunable CW frequency doubler. The Wavetrain uses a BBO crystal in a ring configuration and a Pound-Drever active resonator stabilization method to provide a doubling efficiency of 5-10% over a large spectral range. With its active stabilization, the doubler can follow any reasonable changes in frequency of the input beam.

The frequency of the dye laser is actively stabilized by locking it to a temperature-controlled Fabry-Perot etalon. Changes in laser frequency away from the lock point

are corrected by slightly changing the length of the cavity. Fast deviations are corrected by a piezoelectric-translator(PZT)-mounted mirror resulting in a frequency jitter of less than ~250 kHz. The laser can be scanned over a 30GHz range by rotating a vertex-mounted galvanometer driven quartz plate about Brewster's angle. Although the reference cavity is temperature stabilized, temperature drift is still sufficient to shift the reference cavity lock point by 40MHz/hr in the fundamental (80MHz/hr UV), which is unacceptable for the present work. To minimize the long-term drift, the laser is locked to a frequency stabilized Helium-Neon laser using a second temperature controlled Fabry-Perot etalon. A fraction of the visible radiation emerging through the end mirror of the dye laser is superposed with the output of a polarization-balanced, frequency-stabilized He-Ne laser and directed through a sealed temperature-stabilized confocal Fabry-Perot etalon (FSR 750MHz, Finesse~125). The mirror spacing in the etalon is repetitively scanned at 50Hz using a PZT, producing two series of sharp transmission peaks, one associated with each input wavelength. Changes in the separation between the first pair of neighboring peaks in the scan are monitored and used to generate an error signal that restores the dye laser to the desired frequency. Since this method depends only on the separation of the two peaks and not on their absolute position within the scan, the lock point is insensitive to small thermal drifts of the etalon. The frequency stability is limited by that of the HeNe laser to 1MHz/8 hours in the fundamental ( 2MHz UV). By changing the lock point, the frequency can be scanned over an 800MHz range and

can be controlled externally using a DC input voltage in the range -5V to +5V.

The laser wavelength is monitored using a scanning Michelson interferometer. The system counts the fringes of the unknown wavelength and compares this number to the fringe count of a reference laser, in this case a polarization stabilized HeNe laser. The accuracy of the wave meter is approximately 1GHz at the operating wavelength.

The CW output of the dye laser is chopped into short pulses, typically of $\sim$ 1-2 $\mu$s duration, using an acousto-optic modulator (AOM). The AOM consists of a PZT transducer mounted on a high purity fused quartz block. The transducer generates a high frequency RF acoustic traveling wave inside the quartz. The resulting periodic variation of the refractive index produces a diffraction grating, which can deflect up to 90% of the light out of the zero order. To produce light pulses, rf drive is pulsed periodically deflecting light into the first order which is then directed into the apparatus.

## 3.4   Interaction Region

Excitation occurs near the center of an interaction region bounded by three pairs of independently biasable copper electrodes, each 10cm×10cm. The output of the laser is focused to a spot diameter of $\sim$150 $\mu$m at the atomic beam using a 0.5m focal length UV lens. Even with all electrodes grounded, fields of $\sim$2mV/cm remain at the center of the interaction region. These residual fields primarily result from potassium
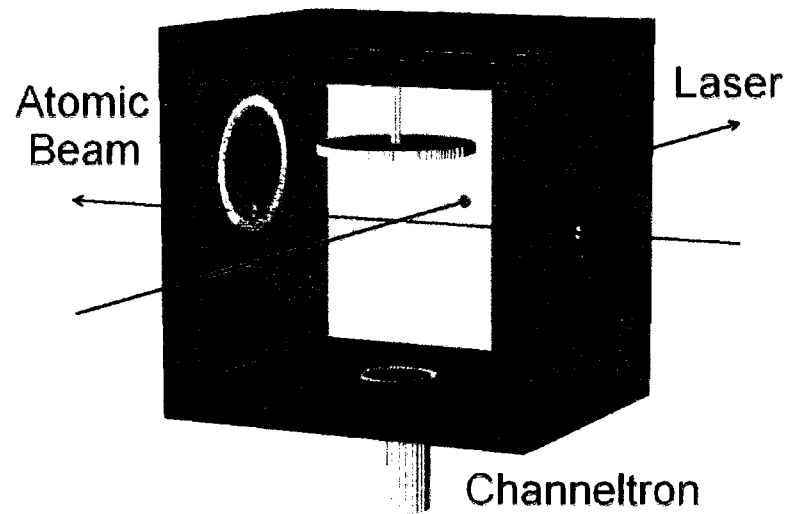
Figure 3.2 : Interaction region.

deposition on the copper electrodes, which generates patch fields due to the difference in work function between copper and potassium (2.3eV for K and 4.5eV for Cu). The use of large electrodes well separated from the experimental volume minimizes the effect of the patch fields associated with these non-uniformities. To minimize motional electric fields, the magnetic field is reduced to < 20mG by use of a $\mu$-metal shield that surrounds the interaction region. The electric fields are locally reduced to <50 $\mu$V/cm by application of small bias potentials to the electrodes that are determined using a technique based on the Stark effect[45]. Except for the bottom plate, all side plates are held at small selected offset potentials obtained using a voltage divider network. This reduces sensitivity to small drifts in the offsets generated by the biasing circuits. The bottom electrode is connected to a ramp generator for selective field ionization.

Electrons resulting from field ionization are accelerated by the ramp and exit the interaction region through a 1" diameter mesh-covered opening in the bottom plate. After exiting the interaction region, the electrons are accelerated to $\sim 100$ eV and detected by a Dr. Sjuts channeltron (electron multiplier). To insure a stable and accurate field zero or field offset during laser excitation, the extraction ramp baseline voltage must not only be very stable over several hours but must also have a near-zero slew rate between laser excitation and the application of the field ionization ramp. During the experiment, the output of the ramp generator is continuously monitored with a GaGe Compuscope 1602 PCI card on a computer running GaGescope professional edition oscilloscope software. The Compuscope 1602 samples at 2.5MS/s and performs a 16 bit analog-to-digital conversion of the analog input signal with a 75dB signal to noise ratio. Real time averaging of the signal is performed using the GaGescope software to eliminate the effects of card-generated noise. The baseline voltage is typically observed to be stable to 0.15mV over an 8 hour period.

## 3.5 Half-Cycle Pulse Generation

The HCPs are generated by applying voltage pulses to one of two circular copper electrodes, each 4cm in diameter, that are positioned to provide fields along the $x$ or $z$ axes. The HCP electrodes are mounted on the end of sections of semi-rigid copper clad RG-141 coaxial cable that are terminated by a 50 $\Omega$ resistor. This arrangement minimizes the stray capacitance of the HCP electrode, allowing fast pulse rise times
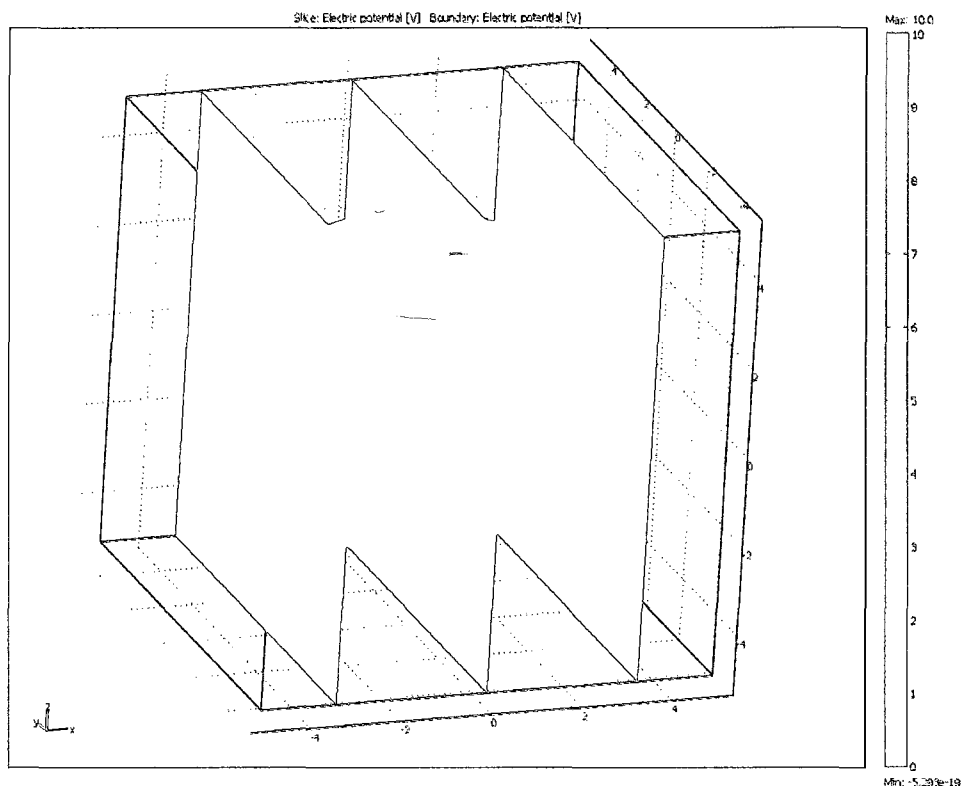
Figure 3.3 : Electric potential inside the interaction region at the time of HCP application. Three slices are shown to demonstrate potential variation in all three spatial dimensions.

(200ps) to be achieved. Positioning the "$z$ electrode" inside the interaction region reduces the symmetry of the system, thus limiting the excitation of resonant cavity modes, which are estimated to be significantly above ~3GHz. The output pulses from the pulse generators are ac-coupled to the HCP electrodes using a Picosecond Pulse Labs 5542 bias-tee to prevent small drifts in the output baselines from introducing stray fields in the experimental volume. The bias-tee combines the ac-coupled HCP signal with the field zero bias voltage. This bias-tee ac-coupler has a flat frequency

response from 10kHz to >50GHz and reduces the rise time of the applied signals by only 7ps. The results of a finite element method solution to Laplace's equation with a HCP applied are shown in Fig. 3.3. It is clear from this result that a strong electric field is produced in the $z$-direction below the HCP Electrode. Near the center of the interaction region, the field is relatively homogeneous. However, the two secondary slices show that traveling significantly away from the center of the region results in a decrease in field strength.

Four externally-triggered fast pulse generators are used to produce the HCPs: a Picosecond Pulse Labs (PSPL) 10,050 pulser, two Hewlett-Packard (HP) 8131A pulsers, and an Advantest D3173 pulse pattern generator. The PSPL 10,050 provides a single 10V pulse and is capable of a 100 kHz rep rate. The pulse rise time is 45ps and fall time is 110ps, with pulse durations from 100ps to 10ns, adjustable in 2.5ps steps. The amplitude is adjusted using broadband attenuators with a bandwidth of DC to 6GHz. The HP8131A is a GPIB-controllable 500MHz pulse generator with two independent outputs. The rise and fall time of the pulses is fixed at ~200ps. The pulse widths are adjustable from 400ps to 500ns in 10ps increments. The amplitude of these pulses is adjustable from 0.1V to 5.0V in 0.01V increments. The HP8131A is capable of running in two modes: single pulse mode or pulse train mode.

The Advantest D3173 pulse pattern generator is an extremely versatile instrument capable of producing a near limitless variety of unidirectional fixed-amplitude pulse

sequences. Despite the complex variety of pulses that can be generated by this instrument, the theory of its operation is quite straightforward. There are two main components to the system: a variable-frequency clock generator and a 64 kilobyte block of high speed addressable digital memory. For each of the 65,536 memory locations, a one or zero can be stored. After the device is triggered, on each clock cycle, each subsequent one or zero stored in memory is transferred to the output similar to the operation of a standard digital shift register. The maximum clock frequency available on the device is 3.2 GHz, yielding a minimum pulse width of 312 ps. This instrument now allows the production of such complicated pulse sequences as frequency chirped pulse trains and so-called "colored" noise which is random noise that contains a well defined band of frequencies.

The complex waveforms required here are produced by combining the outputs of several signal generators using a Mini-Circuits broadband (200kHz-2GHz) power combiner. Semi-rigid RG-141 cable is used throughout because of its very good frequency response and very low attenuation. All the signal generators are separately triggered using a Stanford Research Systems (SRS) DG 535 delay generator. The SRS pulser is a GPIB-controllable precision delay generator capable of adjusting the separation between its two outputs to an accuracy of better than 50ps.

Pulses are measured directly at the electrodes using a Tektronics P6156 DC - 3.5 GHz voltage probe and a Tektronics 7603 sampling oscilloscope equipped with an S-2

type sampling head (<75 ps rise time). Uncertainties in the field calibrations and measurements of pulse profiles introduce an uncertainty of ~10% of the applied field. High frequency components in the pulses are removed using a PSPL 200 ps rise time filter to minimize excitation of resonant modes in the interaction region, which are expected to be significantly above 3 GHz.

## 3.6 High-$n$ Spectroscopy

For the current work, it is necessary to excite Rydberg atoms with a precise value of $n$. The energy levels of very-high-$n$ potassium Rydberg atoms can be represented as

$$E(n,l) = -\frac{R}{(n - \delta(n,l))^2} \tag{3.1}$$

where R is the Rydberg constant and $\delta(n,l)$ is the quantum defect. The quantum defect can be computed using a modified Rydberg-Ritz formula

$$\delta_n \cong a + \frac{b}{(n-a)^2} + \frac{c}{(n-a)^4} + \frac{d}{(n-a)^6} + \frac{e}{(n-a)^8} \tag{3.2}$$

where the $l$ dependant parameters $a$, $b$, $c$, $d$, and $e$ are empirically determined coefficients for $^{39}K$. The $l$-dependence of the quantum defect is a consequence of core penetration. The final excitation wavelengths are given by the equation

$$\frac{hc}{\lambda} = E(n,p) - E(4,s) \tag{3.3}$$

For lower values of $n(\leq 50)$, the resolution of the wavemeter ($\pm 2$GHz) is sufficient to distinguish between adjacent $n$-states. However, in the region near $n\sim 350$, the
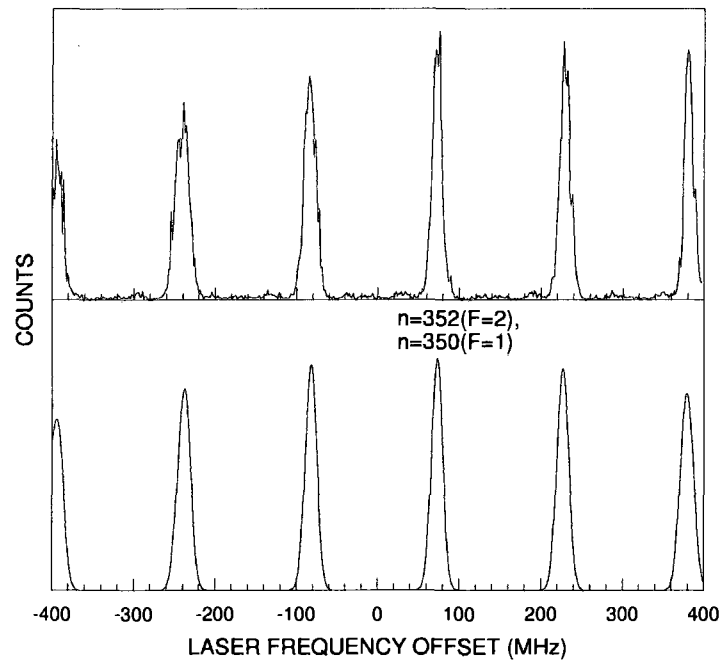
Figure 3.4 : The Rydberg atom excitation spectrum in the vicinity of $n$=350 in near zero field. The frequency offset is in the fundamental (visible). The top figure is an experimental spectrum and the bottom is a calculated spectrum

resolution is not sufficient to allow the accurate identification of individual $n$-states. Therefore, the laser frequency offset is scanned. The resulting frequency spectrum, shown in Fig. 3.4, can be used to identify individual $n$-states, by comparing the experimental level spacings with those calculated from the above formulas. The line width of the states is mostly due to Doppler broadening from the divergence in the atomic and laser beams ($<$0.5 degrees). Figure 3.4 also includes a calculated frequency spectrum for comparison. Not readily apparent in the figure is the presence of two

hyperfine series separated by 461.7MHz, resulting from the excitation of the 4s (F=1) and 4s (F=2) ground state hyperfine levels of $^{39}K$. The relative intensities of each of these lines are proportional to the degeneracy (2F+1) of the two hyperfine levels. The $n$-levels for the two hyperfine states are indicated at the top of the figure. In the vicinity of $n$=350, the best overlap occurs for $n$=352, F=1 and $n$=350, F=2.

## 3.7 Selective Field Ionization

Selective field ionization (SFI) is a technique which allows measurement of the number of surviving Rydberg atoms, but also gives information about the excited state energy distribution. In SFI, a linearly increasing electric field is applied to the Rydberg atoms. Because atoms in different Rydberg states ionize at different applied fields, measurement of the ionization signal as a function of the applied field provides information on the energy distribution of the atoms present at the time of application of the field. If the field rises linearly with time, the observed time dependence of the ionization signal parallels its field dependence.

The detailed physics of ionization by pulsed electric fields is treated in more detail elsewhere(see ref[7]). The field at which ionization occurs depends on both $m$ and the slew rate of the applied field, which governs the path to ionization. Field ionization occurs over two distinct regimes. In small fields ($< \frac{1}{3n^5}$) where states from adjacent Stark manifolds do not yet cross, the parabolic $nn_1n_2m$ states evolve adiabatically in the field. In large fields ($> \frac{1}{3n^5}$) avoided crossings occur between states of the

same $m$ and different $n$. Ionization occurs over a range of field strengths beginning at $\sim \frac{1}{16n^4}$. As the applied SFI ramp increases, atoms with higher values of $n$ therefore ionize before atoms with lower values of $n$. Thus measurement of the time of arrival distribution of electrons resulting from field ionization yields information about the distribution of Rydberg states present at the time of application of the ramp. Free electrons produced by HCP-induced ionization can also be extracted by the electric field ramp and can contaminate the SFI spectrum. Therefore, it is imperative to leave a time delay between the time of HCP application and the time of SFI extraction to allow the free electrons time to drift from the interaction region.
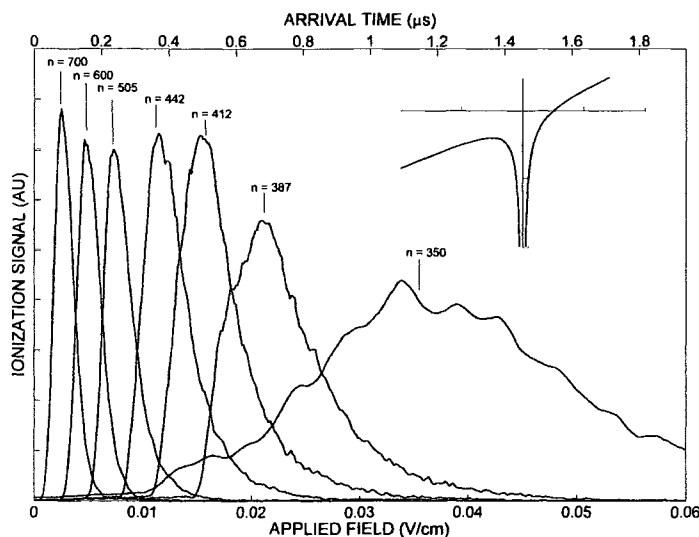


Figure 3.5 : Sample SFI spectra.

For very-high-$n$ atoms, field ionization occurs at very small fields. Thus the time required for liberated electrons to reach the detector depends on the field in which ionization occurs. Therefore for accurate measurement of excited state distributions, a series of SFI calibration spectra must be obtained by tuning the laser to excite specific high-$n$ states and measuring the resulting profile. An example of such spectra is found in Fig. 3.5.

# Chapter 4

# Rydberg Atom Wavepackets in One Dimension
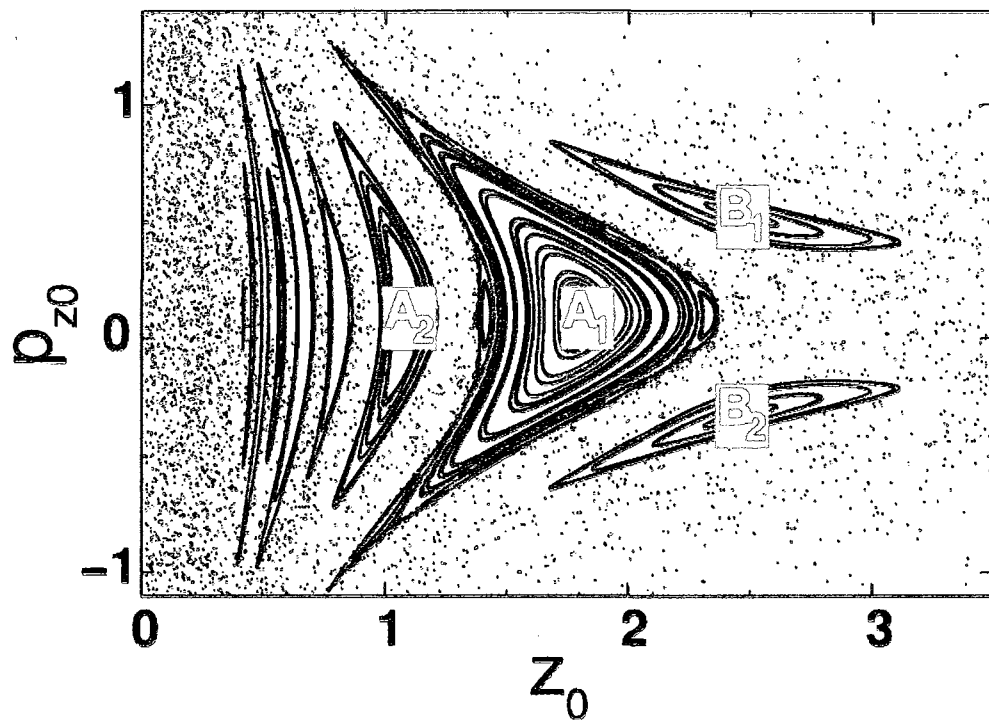


Figure 4.1 : Poincaré surface section scaled to $n_i = 350$ for the periodically kicked hydrogen atom for $\nu_0 = 1.3, \Delta p_0 = -0.2$. The stroboscopic snapshots are taken immediately after each kick. Several stable islands are evident.

## 4.1 Selective Loading of Stable Islands in Phase Space

As discussed in section 2.6.2, application of a train of equispaced unidirectional HCPs to a quasi-1D atom gives rise to a series of sizable islands of stability in an otherwise chaotic phase space. Once a wavepacket is loaded into a stable island, transient phase space localization can be maintained for extended periods. Practical realization of this "dynamical stabilization" is only possible if a wavepacket can be efficiently loaded into the island. For effective loading, a wavepacket must overlap the area of the island at the start of the periodic train of HCPs. Better overlap leads to an increase in the efficiency of loading which we have demonstrated using a carefully-tailored sequence of HCPs.

To position the wavepacket in phase space to allow maximum overlap, two "preparation" pulses are used followed by the train of HCPs that generates the islands of stability. A typical pulse sequence for selective island loading is depicted at the top of Fig. 4.2. A final probe pulse can be added to the sequence to experimentally analyze the final wavepacket. This sequence allows the use of two convenient parameters for controlling the overlap of the wavepacket with the island. The first parameter is the period of the HCP train, $T_T$, which controls the position of the island on the $z$-axis. The second is the time delay between the preparation pulses and the HCP train, $t_D$. Application of this protocol for selective island loading is remarkably efficient with $\sim$90% of the initial quasi-1D Rydberg atoms becoming trapped within it.

Fig. 4.2 illustrates the dynamics underlying the present protocol. We start with
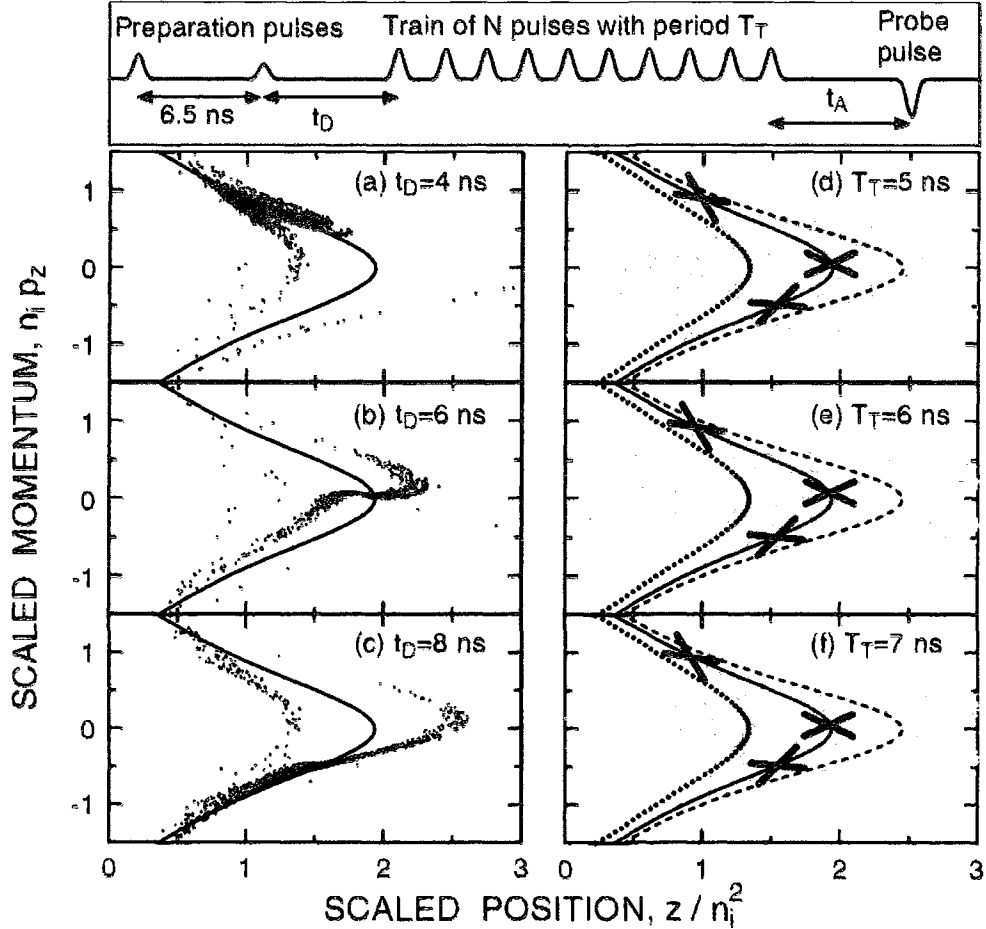
Figure 4.2 : Top: Profile F(t) of applied HCP sequence. (a) − (c) Phase-space portraits of the wave packet following different delay times $t_D$. The solid line shows the torus for the unperturbed initial state. (d) − (f) Poincaré surfaces of section for the 3D kicked hydrogen atom and trains of kicks with scaled strength $\Delta p_0 = -0.1$ and various periods $T_T$. The cuts are taken immediately after each kick and correspond to $\rho_0 \sim 0.5 \pm 0.2$, $p_{\rho_0} \sim 0 \pm 0.2$. The dashed, solid, and dotted lines show, for a 3D atom, the stationary tori that correspond to scaled energies of -0.4, -0.5, and -0.7, respectively. The crosses mark the centers of the wave packets shown in (a) − (c).

potassium atoms in the lowest-lying red-shifted states in the $n_i = 350$ Stark manifold.

(Due to Doppler shifts associated with small beam divergences, photoexcitation leads

to production of an incoherent mixture of $\sim$36 Stark states centered on the parabolic quantum number $n_1 = 320$, a mix that is used in our simulations). These quasi-1D states are oriented along the $+z$ axis, (i.e. the $z$ component of the electric dipole moment $d = -\langle\psi|z|\psi\rangle = -\langle z\rangle$ is negative). The first weak "localizing" HCP provides a scaled impulse $\Delta p_{L_0} = n_i\Delta p_L = -0.085$ directed towards the nucleus. This creates a wavepacket that, after a time delay of 6.5ns ($\sim T_{n_i}$), undergoes strong transient localization into a region of phase space that is smaller than the size of the target island and is located near the outer classical turning point ($z = 2n_i^2$), (see section 2.6.1), with a mean $z$ component of momentum $p_z \sim 0$. A second HCP with scaled strength $\Delta p_0 = n_i\Delta p/2 = -0.05$ provides an initial "positioning" in momentum space as will be discussed later. CTMC simulations showing the subsequent evolution of the wavepacket after the preparation pulses are presented in Fig. 4.2 (a)-(c) for different time delays $t_D$. The centers of these wavepackets are marked with crosses in Fig. 4.2 (d)-(f).

Poincaré surfaces of section showing the islands of stability into which the wavepacket is loaded are also presented in Fig. 4.2 (d)-(f). These surfaces of section were generated for a hydrogen atom subjected to $\delta$-function impulses using the Hamiltonian

$$H^{train}(t) = H^{at} + z\Delta p \sum_{k=1}^{N} \delta(t - kT_T) \tag{4.1}$$

where N is the number of kicks applied, and $H^{at}$ is the atomic Hamilitonian. In the comparisons with experiment below, the dynamics is governed by the Hamiltonian

$H = H^{at} + zF(t)$. The actual time varying HCP electric field profile, not $\delta$-shaped kicks are used. The stroboscopic snapshots used in generating these surfaces were taken immediately after each kick.

The largest of the stable islands, known as a period-one island and denoted $A_1$ in Fig. 4.1, is the focus of this protocol. The physical origin of this island can be understood by noting that a kick, $\Delta\vec{p} = \hat{z}\Delta p$, leads to a change in energy of $\Delta E = \Delta p^2/2 + p_{zi}\Delta p$, where $p_{zi}$ is the initial $z$ component of electron momentum. For stabilization to occur, the electron energy must be nearly constant following each kick. Thus we require that $p_{zi} \approx -\Delta p/2$, which means that the final electron momentum after the kick will be $p_{zf} \approx +\Delta p/2$. The dominant islands in Fig. 4.2 are therefore centered at $p_{z0} = \Delta p_0/2 = -0.05$. The purpose of the second preparation pulse is to center the wavepacket on this value. Phase points that are initially offset from the center of the island follow quasi-periodic orbits, and on the Poincaré surface of section appear to rotate around the central point in the island. We will later exploit this "rotational" motion. The period of the HCP train, $T_T$, controls the position of the center of the island with respect to the initial energy manifold given by $n_i^2 H^{at} = -0.5$. For $T_T = 5$ns, corresponding to a scaled frequency $\nu_0 = \nu_T/\nu_{n_1} = 1.3$, where $\nu_T$ is the kick frequency and $\nu_{n_i}$ is the Keppler frequency, the center of the island is located to the left of the initial torus (Fig. 4.2 (d)). As $T_T$ increases, the center moves towards larger values of $z$ such that for $T_T = 6$ ns ($\nu_0 = 1.06$) it nearly intersects the initial torus (Fig. 4.2 (e)). Whereas for $T_T = 7$ns ($\nu_0 = 0.93$) it is situated to right of the

initial torus (Fig. 4.2 (f)). The effect of varying the delay between the preparation pulses, $t_D$, is demonstrated in Fig. 4.2 (a)-(c). By varying $t_D$ the initial wavepacket can be placed essentially anywhere along the initial torus. By combining these two control parameters, it is possible place the initial wavepacket at any position within the stable island.

To demonstrate this capability, we consider selectively placing the wavepacket near the periphery or "shore" of the island (depicted in Fig. 4.3 as a solid red line). If we choose the control parameters $t_D = 4$ ns and $T_T = 6$ ns, the wavepacket will be located at the upper edge of the island as shown in Fig. 4.2. Fig. 4.3 shows that as the number of kicks, $N$, is increased, the wavepacket circumnavigates the edge of the island. After $N = 9$ HCPs the wave packet returns to its starting point with remarkably little dispersion.

The motion of the wavepacket around the border of the island implies oscillatory behavior in the average electron momentum, $\langle p_z \rangle$, as $N$ increases. The evolution of the $p_z$ distribution, shown in Fig. 4.4 as a function of N, shows clear oscillations with the pattern repeating every ninth kick as expected. Since, as noted earlier, the energy transfer, $\Delta E$, produced by a HCP, and thus the survival probability, depends on $p_{zi}$, these changes in $\langle p_z \rangle$ can be observed experimentally using a probe HCP applied at a fixed delay $t_A$ ($= T_T$) after the last pulse in the train.

As shown in Fig. 4.5, the measured survival probability undergoes strong oscillations as N increases that mirror the predicted changes in $\langle p_{zi} \rangle$. The results are
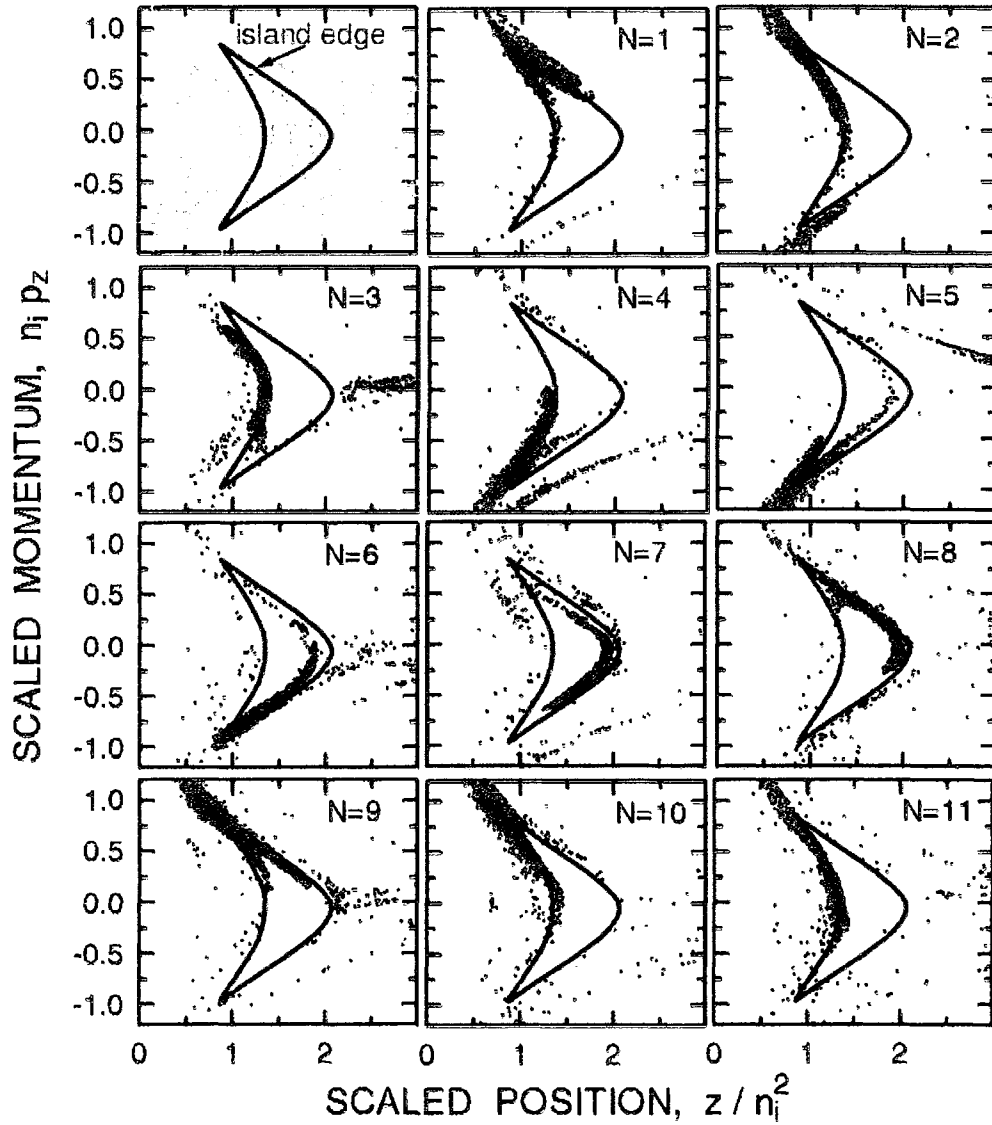
Figure 4.3 : Phase-space portraits showing the evolution of kicks for $T_T = 5$ ns and $t_D = 4$ ns. The wave packet is selectively placed at the periphery of the main island, denoted by the thick solid line. The corresponding Poincaré surface of section is shown at the top left frame. The cuts are the same as in Fig. 4.2

in reasonable accord with the CTMC simulations, which assume that states with

$n \gtrsim 800$ are ionized by stray residual fields in the apparatus and that there are 10%
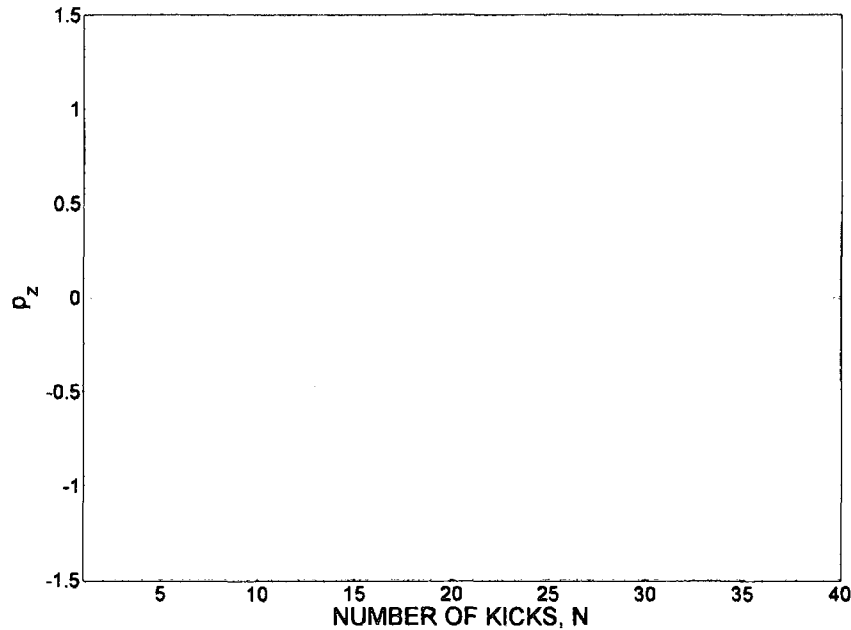
Figure 4.4 : Evolution of the $p_z$ distribution as a function of N for control parameters $T_T = 5$ ns and $t_D = 3.5$ ns.

noise fluctuations in the period and amplitude of the train. The damping of the measured oscillations is somewhat more rapid than predicted, which can be attributed to small field inhomogeneities present in the experimental region.

Selective loading is demonstrated by Figs. 4.5 (a)-(c),which correspond to three different values of the control parameters $T_T$ and $t_D$. Those for Figs. 4.5(a) and (c) were chosen to place the wave packet on the shoreline of the main island but with initial z components of electron momentum of opposite sign (see Fig. 4.2). The ensuing variations in the average electron momentum $\langle p_z \rangle$ are therefore $\pi$ out of phase, which is reflected in the predicted and measured oscillations in the survival
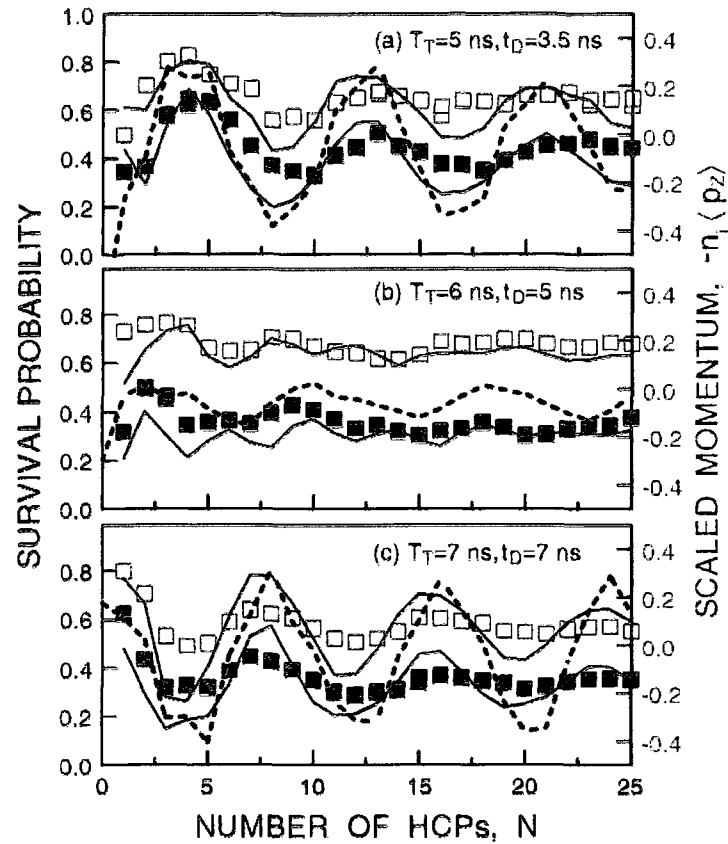
Figure 4.5 : N dependence of the average scaled electron momentum $n_i\langle p_z \rangle$ (dashed line) survival probabilities measured using probe pulses of scaled strength $\Delta p_{A_0} = n_i\Delta p_A = 0.7$ (open squares) and 1.05 (solid squares) for different values of $T_T$ and $t_D$. The solid lines show CTMC simulations that use the experimental pulse profile.

probability. The control parameters for Fig. 4.5 (b) were selected to position the wave packet close to the center of the island. Little variation in $\langle p_z \rangle$ is therefore expected and the oscillations in survival probability are greatly reduced.

Wave packet motion around the periphery of the main island also leads to periodic changes in electron energy (and $n$). The evolution of the electron energy distribution,
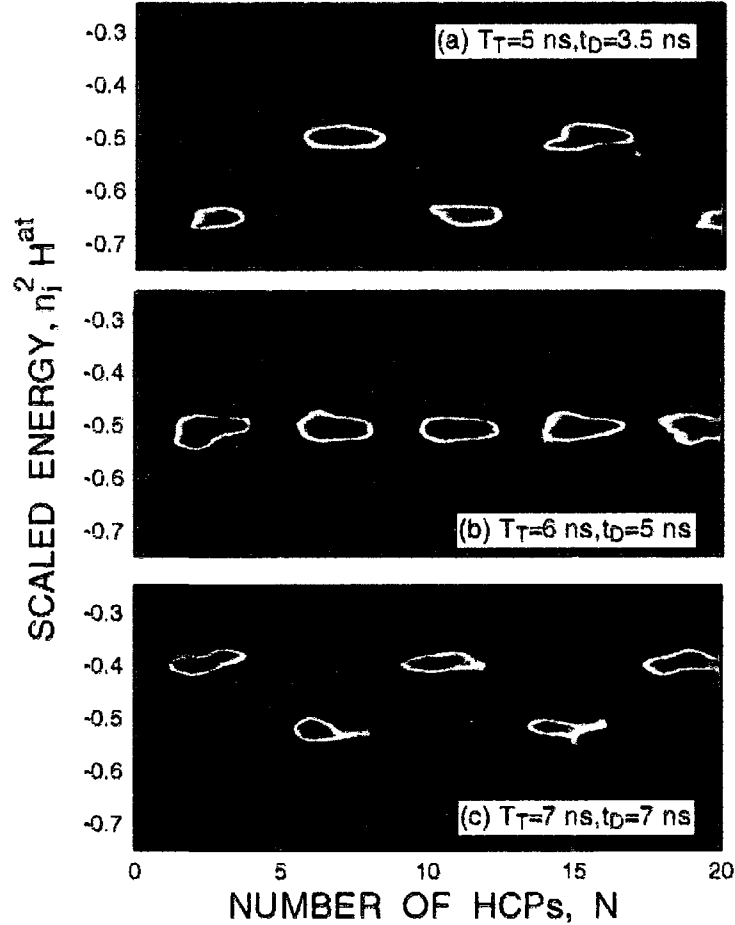
Figure 4.6 : $N$ dependence of the calculated electron energy distribution for different values of $T_T$ and $t_D$ and initial wave packet placement at different locations on the periphery (a),(c) and at the center (b) of the island.

expressed in scaled units $H_0^{at} = n_i^2 H^{at}$, is shown in Fig. 4.6 for the same control parameters as utilized in Fig. 4.5. Strong periodic oscillations are seen in Figs. 4.6(a) and (c), which persist to large $N$. The widths of the energy variations $(-0.7 < H_0^{at} < -0.45$ and $-0.55 < H_0^{at} < -0.35)$ are equal to the energy widths of the corresponding stable islands [Figs. 4.2(d) and (f)]. As expected, the energy fluctuations are minimal

when the wave packet is placed in the center of the island [Fig. 4.6(b)].

The variations in the mean energy $\langle H^{at} \rangle$ with $N$ can be observed by probing the evolution of the wave packet after the train of pulses is turned off. The period of this evolution for a nonstationary wave packet is to leading order, given by the classical Kepler period $T_{\langle n \rangle} = 2\pi(-2\langle H^{at} \rangle^{-3/2})$, where $H^{at}$ depends on $N$. The period is monitored using a probe HCP applied at different time delays $t_A$ after the HCP train.
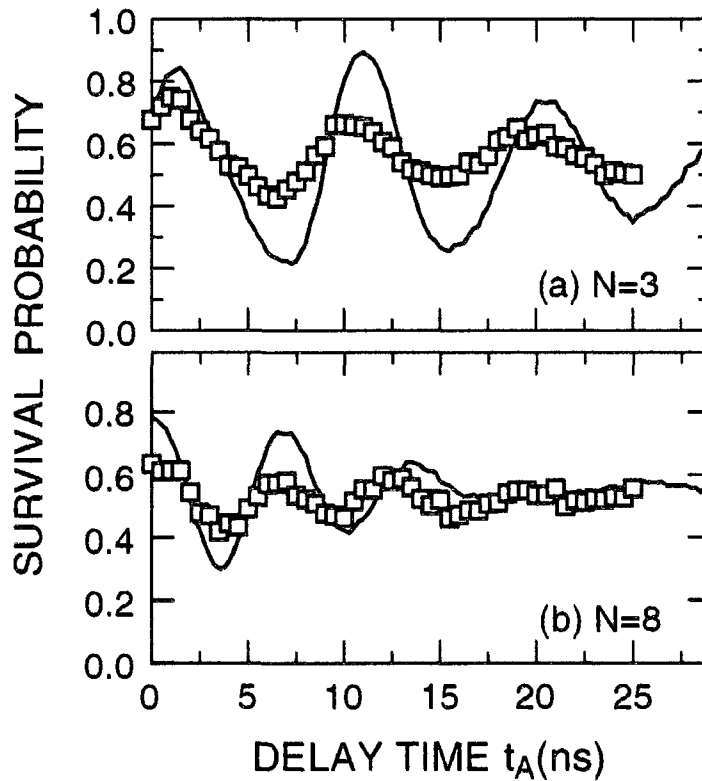


Figure 4.7 : Time evolution of the wave packet after $N = 3$ and $N = 8$ HCPs for $T_A = 7$ ns and a probe pulse of scaled strength $\Delta p_{A_0} = 0.8$. The experimental data (squares) are compared with CTMC simulations (solid lines) that employ the same assumptions as for Fig. 4.5

Typical experimental results are presented in Fig. 4.7. Periodic variations in survival probability are seen, the period changing from $T_{\langle n \rangle} \sim 9.5$ ns for $N = 3$ [Fig. 4.7(a)] to $T_{\langle n \rangle} \sim 6.0$ ns for $N = 8$ [Fig. 4.7(b)]. These periods are in good agreement with those predicted by CTMC simulations, although the predicted amplitudes of oscillation are somewhat larger than those measured, presumably as a result of field inhomogeneities in the experiment and of uncertainties in the initial mix of Stark states excited. These results demonstrate the remarkable level of control over atomic wavepackets that can be achieved in high Rydberg levels ($n \gtrsim 350$). Using a carefully tailored sequence of HCPs we have successfully placed phase space localized wave packets near the shore and near the center of a stable island and followed their subsequent motion within the island. Such time-resolved control over the position of the wave packet in combination with the suppression of its spreading holds promise for realizing more complex protocols for steering wave packets to preselected regions of phase space or for switching population between islands.

## 4.2 Transporting Rydberg Electron Wavepackets with Chirped Trains of Pulses

The previous section demonstrated that using a tailored sequence of HCPs, a wavepacket can be selectively loaded into islands of stability in phase space, leading to a dynamically stabilized non-dispersing wavepacket. Recent theoretical work suggests that, once a wavepacket is succesfully loaded into such a stable island, by adiabatically

varying the frequency of the HCP driving train the wavepacket can be transported

to arbitrarily pre-selected regions of phase space[46]. This effect is based on the fact

that the position of the stable island in phase spaces depends on both the amplitude

and frequency of the driving train.
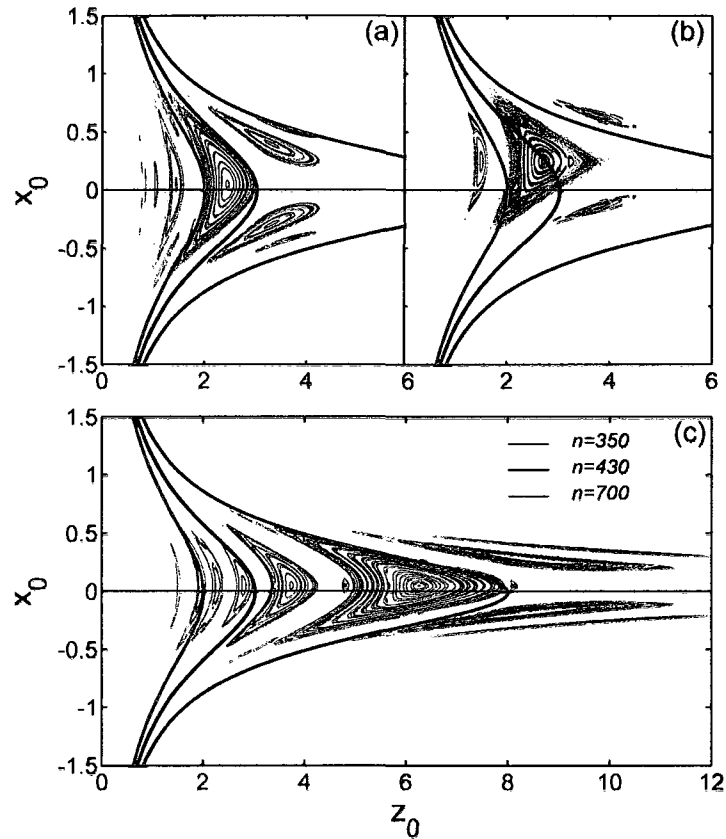


Figure 4.8 : Stable islands in phase space for a periodically kicked quasi-1D atom. (a)$\Delta p_0 = -0.1$, $\nu_0 = 1.3$. (b)$\Delta p_0 = -0.5$, $\nu_0 = 0.77$. (c)$\Delta p_0 = -0.1$, $\nu_0 = 0.2$. Also included are tori representing the position of stationary states for several different $n$ levels (solid lines).

The positions of stable islands for several different driving trains are shown in

Fig. 4.8. Frame (a) shows the Poincaré surface of section for a driving train with scaled impulse, $\Delta p_0 = -0.1$ and scaled frequency, $\nu_0 = T_n/T = 0.77$, where $T$ is the period of the train, and $T_n$ is the electron orbital period. Notice the presence of a large island of stability centered at $z_0 = 2.2$ and $p_{z0} = 0.05$. This is the largest of the islands and its dynamics corresponds to a single pulse per orbit[44], and is therefore called a period-1 island. The position of this island along the $z$-axis depends on the period of the driving train. As the period is increased to $\nu_0 = 0.2$, the position of the period-1 island moves to $z_0 = 6.2$, as shown in Fig. 4.8. The resulting island for a train with scaled impulse, $\Delta p_0 = -0.5$ and scaled frequency, $\nu_0 = T_n/T = 0.77$ is shown in Fig. 4.8(b). Notice that the position along the $z$-axis is the same as in Fig. 4.8(a), however, the vertical position of the island has shifted to $p_{z0} = 0.25$, which is of course $\Delta p/2$.

It is clear that the position of a stable island can change by changing the parameters of the HCP train, but the remaining question is can a wavepacket, once loaded into an island, follow the position of the island. The result is that if the rate of change of the period is sufficiently slow, a wavepacket initially localized in the island can respond adiabatically and remain trapped in the island as it "moves", thereby allowing it to be transported to a different location in phase space, to a different location in coordinate space, $z$, and to different quantum numbers $n$. The adiabaticity criterion [47] suggests that this can be accomplished if $\delta T \ll T$ where $\delta T$ is the change in time interval between adjacent kicks, or chirp. This is demonstrated in Fig. 4.9, where a
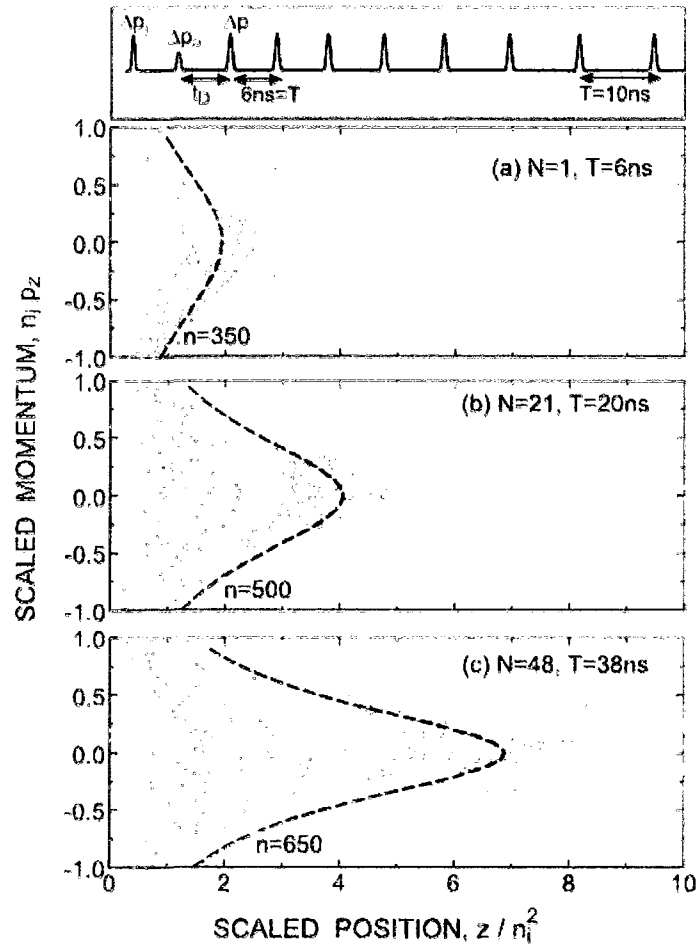
Figure 4.9 : Upper panel: profile of applied HCP sequence. The pulse spacing in the chirped train is incremented linearly as $t_{j+1} - t_j = 6\mathrm{ns} + 0.67(j - 1)$ ns. Lower panels: Dark points, phase space distribution of the present wave packet, projected on the $z$, $p_z$ plane, immediately before the 1st, 21st, and 48th kick in the chirped HCP train. The axes are labeled in scaled units. Light points, corresponding Poincaré surfaces of section for the 3D kicked hydrogen atom with $T = 6$, $T = 20$, and $T = 38$ ns, and $\delta$-function kicks with scaled strength $\Delta p0 = -0.1$. The cuts are taken immediately before each kick. The dashed lines indicate stationary tori corresponding to states with $n = 350$, $500$, and $650$

classical ensemble of phase space points that simulates the wave packet created here is transported from $z_0 \simeq 1.8$ to $z_0 \simeq 6.5$. The spacing between adjacent pulses is incremented linearly as $t_{j+1} - t_j = 6\text{ns} + (j-1)\delta T$ using $\delta T = 0.67$ ns $\ll T_n$.

The efficiency of the present protocol is maximized by carefully loading the island starting with a quasi-one dimensional (quasi-1D) state localized along the z axis. The pulse sequence, shown in Fig.4.9, is comprised of a "localizing" HCP $\Delta p_L$, a "positioning" HCP $\Delta p_P$ and a chirped train of N identical HCPs. The first localizing HCP provides a kick of scaled strength $\Delta p_{L0} = n_i \Delta p_L = -0.085$ directed towards the nucleus. This creates a wave packet which after a time delay of $\sim 6.5$ ns $(T_{n_i})$ undergoes strong transient localization [48] into a region of phase space located near the outer classical turning point $((z, p_z) \sim (2n_i^2, 0))$ that is smaller than the dominant island. The positioning pulse, $\Delta p_P$ (applied at the time of optimum localization) is used, in conjunction with the time delay $t_D$ (see Fig. 4.9) to optimally position the wave packet within the island [49] at the start of the chirped HCP train. The values employed $(\Delta p_{P0} = n_i \Delta p_P = -0.05, \tau_D = 7.4$ ns) were optimized through both experiment and simulation (see section 4.1).

The chirped HCP train was provided by a programmable pulse pattern generator (PPG) that divides time into a series of bins and in each outputs a voltage of 0 or $V$ (see section 3.5). The bin width was set at 0.67ns and $V$ was chosen to deliver a scaled impulse $\Delta p_0 = n_i \Delta p = -0.1$. The electron is initially in a stationary quasi-1D Rydberg state [50] oriented along the $z$ axis.
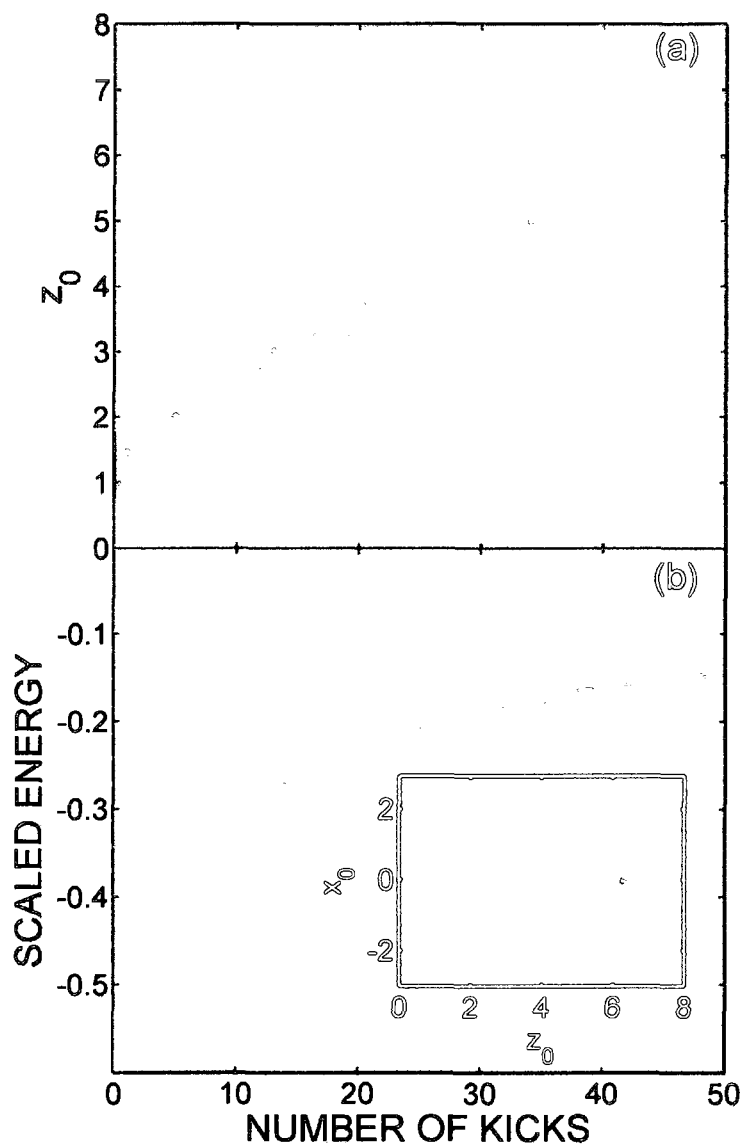
Figure 4.10 : Calculated evolution of the (a) spatial and (b) electron energy distributions of quasi-1D $n_i = 350$ Rydberg atoms during a linearly chirped train of $N = 50$ HCPs of strength $\Delta p_0 = -0.1$ and period $t_{j+1}t_j = 6$ns $+0.67(j - 1)$ns. The inset shows the final electron spatial distribution.

The calculated evolution of the electron position, momentum and energy distributions during the chirped train is shown in Fig. 4.10. Even though the initial chirp rate $\delta T/T$ is sizeable ($\sim 0.1$), the overlap between the islands associated with successive pulse spacings is sufficient to allow the electron wave packet to remain trapped moving linearly up in $z$ as $N$, and the pulse separation, increases. The final two-dimensional spatial distribution following 50 HCPs is shown in the inset in Fig. 4.10. This was calculated 0.5 $\mu$s after the last HCP to allow the product wave packet to reach its quasistationary state. Remarkably, the final state is nearly as strongly polarized as is the initial quasi-1D state. As $N$ increases, the atom also moves steadily up in $n$ but the electron energy distribution remains narrow [see Fig. 4.10(b)]. More than 95% of the parent atoms are predicted to survive the HCP sequence and be transported to very-high-n states.

The calculated energy distribution following 50 HCPs is strongly peaked at $n \sim 660$ with a width at half height of $\Delta n \sim \pm 30$, which is significantly narrower than those found for previous HCP protocols [49]. SFI studies confirmed this behavior. For reference, Fig. 4.11(a) shows SFI spectra recorded with no applied dc field and the photoexcitation laser tuned to produce selected high-$n$ states. As expected, as $n$ is increased the spectra move towards earlier times, i.e., ionization occurs at lower fields. SFI spectra obtained following application of different numbers of HCPs are presented in Fig. 4.11(b). These move steadily towards earlier times as $N$ increases, consistent with transfer to higher-$n$ states. Their widths remain comparable to those
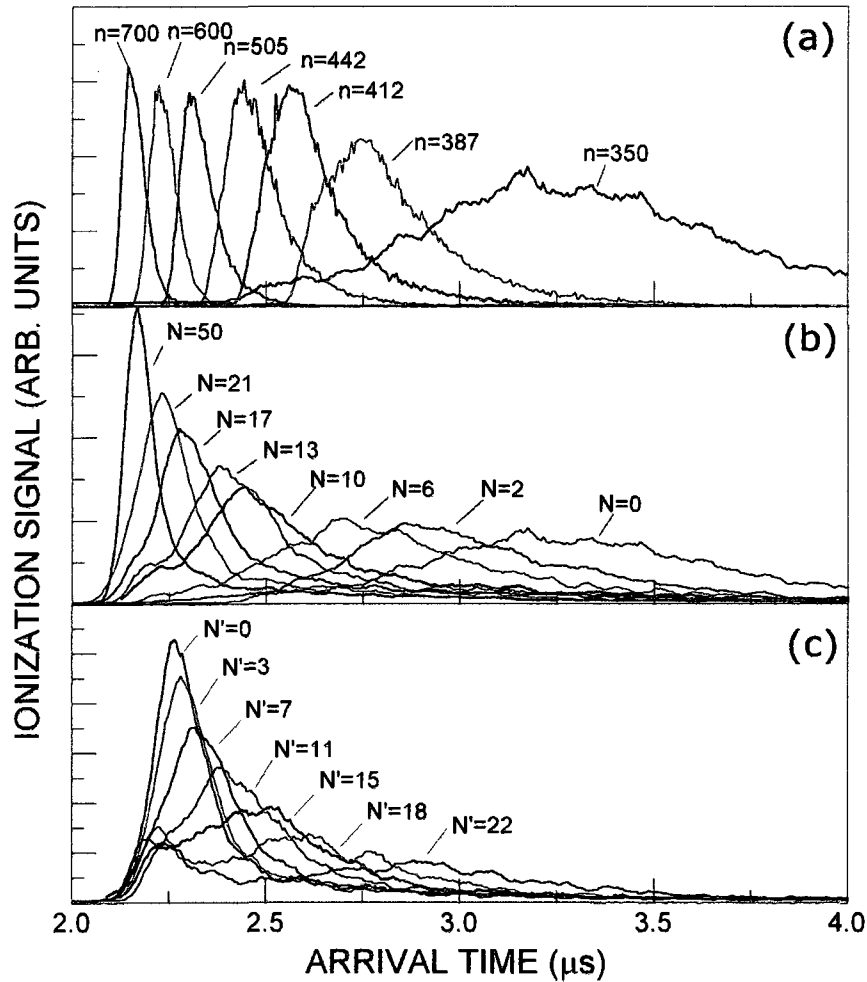
Figure 4.11 : (a) SFI calibration spectra recorded with no applied dc field and the laser tuned to excite states with the values of $n$ indicated. (b) SFI spectra recorded following application of the numbers $N$ of HCPs indicated in the down-chirped train shown in Fig. 4.10. (c) SFI spectra recorded following application of the number $N'$ of up-chirped HCPs indicated (see text).

seen following excitation of single Rydberg states pointing to a narrow final $n$ distribution. By extending the chirp to larger values of $T$ it should, in principle, be possible to generate localized groups of states with arbitrarily high $n$. This could not

be verified experimentally as stray fields and field inhomogenities in the apparatus begin to ionize atoms with values of $n$ above $\sim$ 800 - 900. For large $N$ a small tail is evident on the SFI features that extends to later times, indicating that a small fraction of the parent atoms escape the island. Such escape could account for the measured overall survival probability, typically $\sim$ 80% - 90% , being somewhat lower than predicted by simulation and can be attributed to uncertainties in the alignment of the initial states, i.e., in the orientation of the initial Stark field, induced by stray fields.
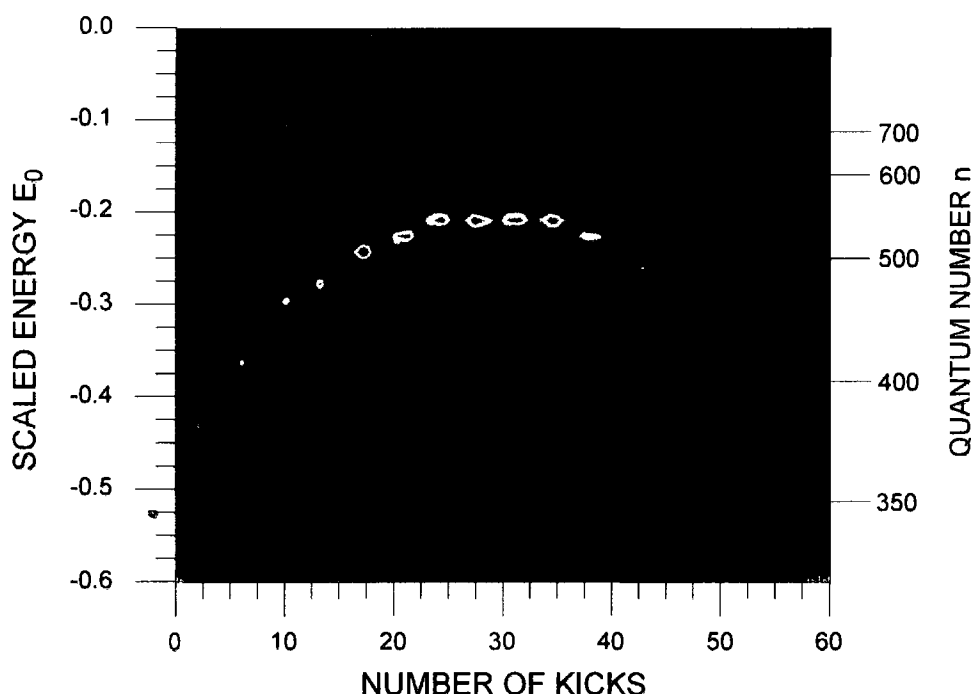
Figure 4.12 : Calculated evolution of the electron energy distribution for quasi-1D $n_i = 350$ atoms subject to a chirped HCP train in which the pulse separation is linearly increased for the first 25 HCPs, held constant for 10 HCPs, and then linearly decreased (see text). The spacing between the first two pulses was 6 ns and was incremented in units of ± 0.67 ns.

Coherent state manipulation using a chirped HCP train is also reversible. This was demonstrated by first driving parent $n_i \sim 350$ Stark states to higher-$n$ ($n \sim 540$ states using the first 25 HCPs in the "down-chirped" train shown in Fig. 4.9. This was followed by 10 pulses with constant separation $T = 22$ ns before applying 25 "up-chirped" HCPs with linearly decreasing separation ($\delta T = 0.67$ ns). The calculated evolution of the electron energy distribution during this pulse sequence is shown in Fig. 4.12. As the pulse separation decreases the wave packet is driven steadily towards states of lower $n$, but remains narrow in energy. Overall, more than 90% of the parent atoms survive the pulse sequence. Once again, this evolution in the energy distribution was confirmed experimentally using SFI [see Fig. 4.11]. Towards the end of the pulse train, however, an early-time SFI feature becomes apparent indicating that some atoms are left in very-high-n states. For low-$n$ states ($n < 450$) the SFI profile after $N' = 22$ HCPs is similar to that for $N = 2$ (the time-reversed partner would be $N = 3$). Overall, approximately 70% - 80% of the parent atoms survive the entire pulse sequence, $\sim$ 70% of which return to $n < 450$ states (i.e., the combined return probability is $\sim$50%).

The narrow width of the final momentum distribution was confirmed experimentally by applying a probe HCP immediately following the last pulse in a train of $N = 25$ chirped pulses. As shown in Fig. 4.13, the survival probability falls steadily with increasing probe strength displaying a reasonably sharp steplike drop near $\Delta p_0 \simeq 0.7$, which is significantly steeper than that seen for the initial station-
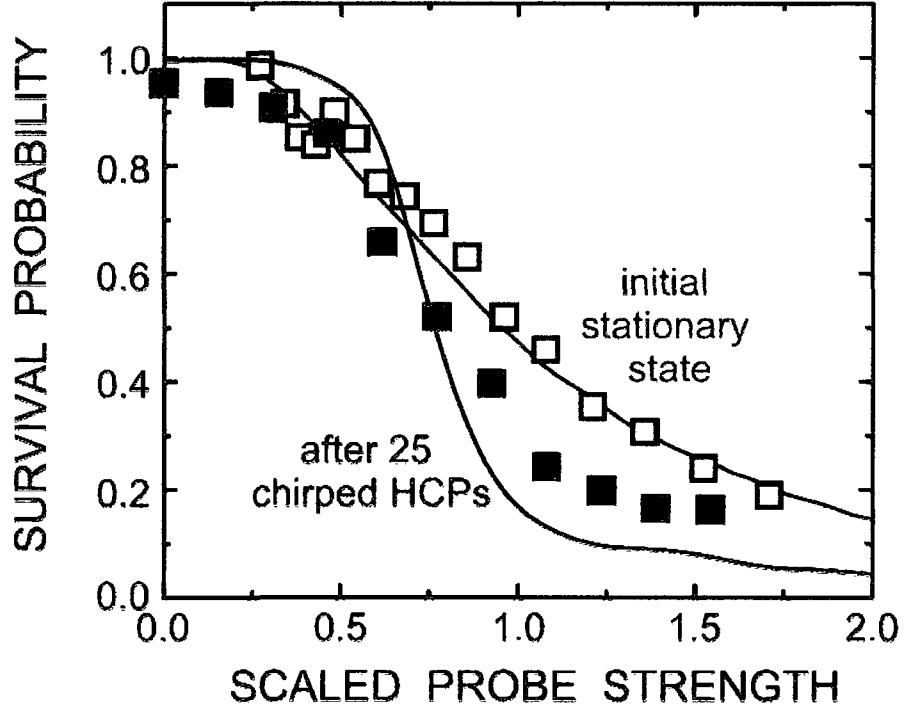
Figure 4.13 : Dependence of the survival probability on the scaled strength $\bar{n}\Delta p_{probe}$ of a probe kick, where $\bar{n}$ is the average principal quantum number of the states being probed, when the probe impulse is both applied directly to the initial $n = 350$ quasi-1D state and following the first 25 HCPs in the train shown in Fig. 4.9 such that $\bar{n} = 540$. The experimental results (symbols) are compared with CTMC simulations (lines) assuming that stray fields and field inhomogenities in the experiment ionize atoms with $n > 800$.

ary state. The steplike decrease provides clear evidence that transport by a chirped HCP sequence preserves the localization of the wave packet in both position and momentum[48]. Again, a reduction in initial alignment can account for the difference between theory and experiment.

Application of the present protocol is not restricted to quasi-1D atoms nor does it necessarily require prelocalization. Transport without prelocalization was explored

through both simulation and experiment using K(351p) atoms (rather than quasi-1D atoms) for which there is reasonable initial overlap with the main island. While the efficiency with which parent atoms can be transported to the targeted (higher) $n$ states is reduced, the results showed that some 25% can still be transferred to the desired levels.

## 4.3 Transferring Rydberg Wavepackets Between Period-1 and Period-2 Stable Islands

As discussed in the two previous sections, the classical phase space of periodically driven systems is generically characterized by a series of stable islands embedded in a chaotic sea[51, 52, 53, 2]. While phase flow between islands that are separated by the chaotic sea is classically forbidden, quantum dynamics allows such transfer by way of "Dynamical tunneling" [54, 55]. In this section we present a *classical* protocol by which the phase space distribution can be efficiently transferred between islands across the chaotic sea without invoking any quantum effects. Key to the protocol is the transient deformation of the phase space by a near adiabatic modulation of the driving field. We demonstrate, both theoretically and experimentally, the efficiency of this protocol using atoms in high Rydberg states subject to a sequence of half-cycle pulses (HCPs). One prerequisite for the realization of transport between islands is the creation of an initial state that is well localized within a given island.

Classically, localization or trapping of phase space density results from the (nearly)

impenetrable borders of the islands, the Kolmogorov-Arnold-Moser (KAM) tori for the periodically driven Rydberg atom[51, 52, 53, 2]. Quantum mechanically, trapping in an island corresponds to formation of a nondispersive wave packet[42, 56, 57] and results from the modification of the Rydberg eigenenergy spectrum by the periodic external perturbation[42, 58]. The driving field helps to preserve phase matching between quasieigenstates of the periodically driven system, i.e., the Floquet eigenstates of the period-1 time evolution operator (Floquet operator)[58]. The spectrum of the corresponding quasienergies is, in part, equispaced, which allows for nondispersive wave packets within classical islands of stability. As in the case of the harmonic oscillator, such nondispersive wave packets behave like classical particles and their dynamics can be controlled and manipulated in much the same way as those of a classical particle. Due to the modified eigenenergy spectrum, dispersion is slow, and localized wave packets can be maintained for extended periods. Furthermore, for $n \sim 350$ the Heisenberg (or quantum break) time[51, 52] is of the order of microseconds. Thus within the experimentally accessible observation time ($\sim 1\mu s$), quantum and classical dynamics should closely mirror each other.

## 4.3.1 The Physics of Period-2 Islands

Several protocols to manipulate nondispersive wave packets based on their underlying classical dynamics have been suggested[59, 39]. This can be accomplished by adiabatically changing the position of the classical resonances at the centers of the

stable islands. For weak fields, the largest island occurs when the frequency of the unperturbed electron Kepler orbit $\nu_n = 1/(2\pi n^3)$ is synchronized with the frequency $\nu$ of the external driving ($\nu \sim \nu_n$). This period-1 island is remarkably robust against slow changes in the external driving field and is therefore the preferred starting point for steering Rydberg wave packets to different regions of phase space by chirping the period or the strength of the driving field[60].

In this section we describe a technique for transferring a wavepacket from this period-1 island to a pair of period-2 islands across the chaotic sea. This is accomplished by taking advantage of a protocol that employs two superposed trains of identical pulses, each with the same period, whose relative time shift $\tau$ is adiabatically varied. A notable feature of such time shift chirping is that it is possible to keep the principal action $n$ (approximately) constant while slowly changing the stroboscopic value of the conjugate angle variable, the "mean anomaly"[61]. In contrast, simply chirping the period of a train of pulses leads to the opposite result, i.e., the action is changed while the angle remains approximately constant. The two chirping protocols thus complement each other and provide powerful tools with which to control Rydberg wavepackets. The physical processes underlying the present protocol can be understood with the aid of theoretical simulations.

As discussed in section 2.6.2, the response of a Rydberg atom to a periodic train of $N$ identical half-cycle pulses with profile $F_{HCP}(t)$ directed along the z axis is governed by the Hamiltonian

$$H(t) = \frac{p^2}{2} - \frac{1}{r} + zF_{train}(T, \Delta p, t) \qquad (4.2)$$

where $\vec{r}(x, y, z)$ and $\vec{p}(x, y, z)$ are the postition and momentum of the Rydberg electron, and

$$F_{train}(T, \Delta p, t) = \sum_{j=1}^{N} F_{HCP}(t - t_j)$$

$$= \sum j = 1^N F_{HCP}(t - jT)$$

$$\simeq -\sum j = 1^N \Delta p \delta(t - jT) \qquad (4.3)$$

with $T = t_{j+1} - t_j$ being the period of the train. Here we consider quasi-1D Rydberg atoms oriented along the $z$ axis subject to kicks directed toward the nucleus, i.e., with $\Delta p < 0$.

Figures 4.14(a) and (d) demonstrate typical phase space portraits (Poincaré surfaces of section) for the kicked atom when driven by trains of HCPs with period $T = 6$ ns and $T' = 12$ ns respectively, with each pulse delivering kicks of scaled strength $\Delta p_0 = n_i \Delta p = -0.1$. These exhibit a mixed phase space consisting of stable islands embedded in a chaotic sea. The stroboscopic snapshots used in generating these figures were taken immediately before each kick. Since we focus here on quasi-1D motion along the z axis, the cuts used are for the limit $\rho = \sqrt{x^2 + y^2} \to 0$ and $p_\rho = (xp_x + yp_y)/\rho \to 0$. The axes are labeled in scaled units $z_0 = z/n_i^2$ and $p_{z0} = p_z n_i$, where $n_i = 350$. The stable islands are associated with electron motion that is syn-
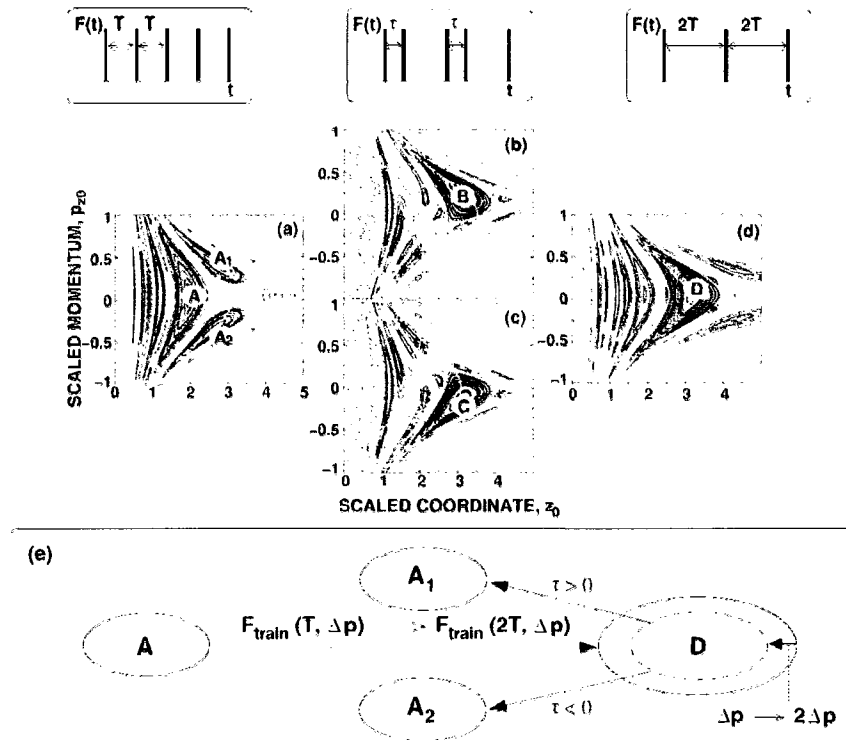
Figure 4.14 : (a) - (d) Poincaré surfaces of section of the periodically kicked Rydberg atom. (a) A single train is applied with a scaled kick strength of $\Delta p_0 = -0.1$ and period $T=6$ ns. The stroboscopic snapshots are taken immediately before each kick. (b), (c) Two identical HCP trains with $\Delta p_0 = -0.1$ and period $T'=12$ ns and a relative time delay $\tau=3$ ns are applied. The stroboscopic snapshots are taken immediately before each kick in the first (b) and second (c) train. (d) Same as (a) but for a period $T' =12$ ns. The phase space coordinates are scaled to $n_i=350$. The upper panels show the associated pulse timing sequences with each HCP represented by a $\delta$ function. The gray dashed lines in (a) show Kepler orbits with principal actions of $n_{A_1} \simeq 435$ and $n_{A_1} \simeq 465$. In (b) the Kepler orbit with $n = n_{A_2}$ and in (c) and (d) that with $n = n_{A_1}$ is drawn. In (e), the steps involved in the protocol for transporting phase space density from island $A$ to $A_1$ or $A_2$ via $D$ are schematically indicated.

chronous with the periodic train leading to dynamical stabilization. Otherwise the electron follows a chaotic trajectory and eventually becomes ionized[43]. Immediately before each kick, the largest islands in Figs 4.14 (a) and (d) are centered, respectively,

at $(z_0, \ p_{z0}) \sim (2,-\Delta p_0/2)$ (labeled as A) and $(z_0, \ p_{z0}) \sim (3.3,-\Delta p_0/2)$ (labeled as D). Thus the effect of a kick of magnitude $|\Delta p_0|$ in the $-z$ direction on an electron located near the center of either island is to change its z component of momentum from $p_{z0} = +|\Delta p_0|/2$ to $p_{z0} = -|\Delta p_0|/2$, i.e., the z component of its momentum is reversed while its energy remains essentially unchanged. Clearly, synchronization of the kick frequency $\nu$ and the Kepler frequency $\nu_n$ is a prerequisite for the formation of a stable island. When the frequency is reduced by a factor of 2, the center of the island moves away from the nucleus toward larger $z$, because only a smaller Kepler frequency (or larger $n$) meets the synchronization condition.

At the higher driving frequency two stable islands [labeled as $A_1$ and $A_2$ in Fig. 4.14(a)] also appear. These are associated with Kepler orbits of higher $n$ than for island A and are termed period-2 islands. If an electron is located in the island $A_1$, its momentum is positive. Therefore, a kick toward the nucleus decelerates the electron and its energy is reduced. After half a Kepler period, the electron reaches the island $A_2$ with negative momentum. Application of another kick at this time accelerates the electron and the energy is increased. The losses and gains in energy following successive kicks cancel and the net energy transfer vanishes. This causes the electron to periodically transition between Kepler orbits with $n \sim 435$ and 465. This periodic energy variation is a signature of the dynamics of an electron trapped in a period-2 island.

Due to the increase in complexity of the dynamics, period-2 islands are less stable

than those of the period-1 islands such as A and D. As a consequence, the period-2 islands $A_1$ and $A_2$ cover less area in Poincaré surface of sections than islands A and D. It is thus more challenging to trap a wavepacket in period-2 islands. Once a wavepacket is loaded, however, its evolution can be rather easily monitored using a probe HCP because the centers of the islands $A_1$ and $A_2$ correspond to opposite signs of $p_z$. For a probe kick directed along the $+z$ axis, a wavepacket positioned in the island $A_1$ ($p_z > 0$) will gain energy, leading to ionization, whereas a wavepacket positioned in island $A_2$ ($p_z < 0$) will lose e ergy, and little or no ionization will occur. The resulting changes in survival probability as the wavepacket oscillates between $A_1$ and $A_2$ thus provide a clear signature of the population of period-2 islands. Furthermore, once the train of HCPs is turned off, the wavepacket will evolve at a rate characteristic of the period of the final $n$ manifold. Since the period-2 orbit invloves two different energy manifolds, the periodic transistions between $A_1$ and $A_2$ can be seen by monitoring the time evolution of the final state using a probe HCP applied after a variable time delay[56].

### 4.3.2 Transfer between islands: Response to a superposition of two trains of pulses

The main objective in this section is to establish a protocol to transfer an electronic wavepacket that is trapped in a period-1 island centered at A to the period-2 islands centered at $A_1$ and $A_2$. All of these islands correspond to the "same" train

of pulses, e.g. with the same kick strength $\Delta p_0 = -0.1$ and period $T = 6$ ns. In section 4.2, a protocol was demostrated to navigate wavepackets in phase space by adiabaticaly chirping the period of the pulses in a train. This chirping technique allows a wavepacket trapped in island A to be transported to island D by adiabatically chirping the interval $t_{j+1} - t_j$ between successive HCPs in the train from $T = 6$ ns to $T' = 12$ ns. However, and adiabatic modulation of a single train of pulses that starts and ends with the same values of $T$ and $\Delta p$, will return the wavepacket to its original location in phase space. Transfer from a period-1 to a period-2 island thus requires the introduction of a new control variable, which we obtain by superposing a second train of pulses onto the first.

To understand the protocol, it is instructive to first analyze the phase space structure for a Rydberg atom subject to the following superposition $F_s$ of two identical pulse trains each of which is periodic with period $T'$:

$$F_s(T', \Delta p, \tau, t) = F_{train}(T', \Delta p, t) + F_{train}(T', \Delta p, t - \tau) \qquad (4.4)$$

where $\tau$ is the relative time shift between the trains. This superposition is also periodic in time with period $T'$ and contains two pulses per period. Correspondingly, the phase space portrait evolves in time. Figures 4.14 (b) and (c), respectively, show Poincaré surface of sections immediately before each kick in the first train at times $t = jT'$ and before each kick in the second train at times $t = jT' + \tau$ for $\tau = 3$ ns. During the time interval $\tau$ the Poincaré surface of section changes from that in

Fig. 4.14(b) to that in Fig. 4.14(c) before returning to that in Fig. 4.14(b) a time $2T - \tau$ later.

The present protocol is based on the fact that the superposition in Eq. (4.4) has the following limits:

$$F_s(T', \Delta p, \tau \to 0, t) = F_{train}(T', 2\Delta p, t) \tag{4.5}$$

$$F_s(T', \Delta p, \tau \to T, t) = F_{train}(T, \Delta p, t) \tag{4.6}$$

As $\tau \to 0$, $F_s$ collapses to a single train of pulses of period $T' = 2T = 12$ ns as used to generate Fig.4.14(d) but with twice the amplitude. This leads to little change in the PSS because $\Delta p$ is small. The size of the island D is slightly reduced but its position is largely unchanged. Conversely, as $\tau \to T = T'/2$ we recover a pulse train identical to that used to generate Fig.4.14(a). As $\tau$ is varied from 0 to $T$, the period-1 island D is "morphed" into the period-2 islands $A_1$ and $A_2$ through the intermediate structure shown in Figs.4.14 (b) and (c), i.e. through the islands labeled B and C. In summary, by chirping the frequency of the HCP train, introducing a second superposed HCP train, and varying the time delay $\tau$, a wavepacket initially localized in the period-1 island A can be adiabatically transferred to the period-2 islands $A_1$ and $A_2$. A diagram of the path followed by the wavepacket during this protocol is illustrated in Fig.4.14(e).

The complete HCP used in the present protocol is shown in Fig. 4.15 and consists of the following elements that can be realized experimentally.
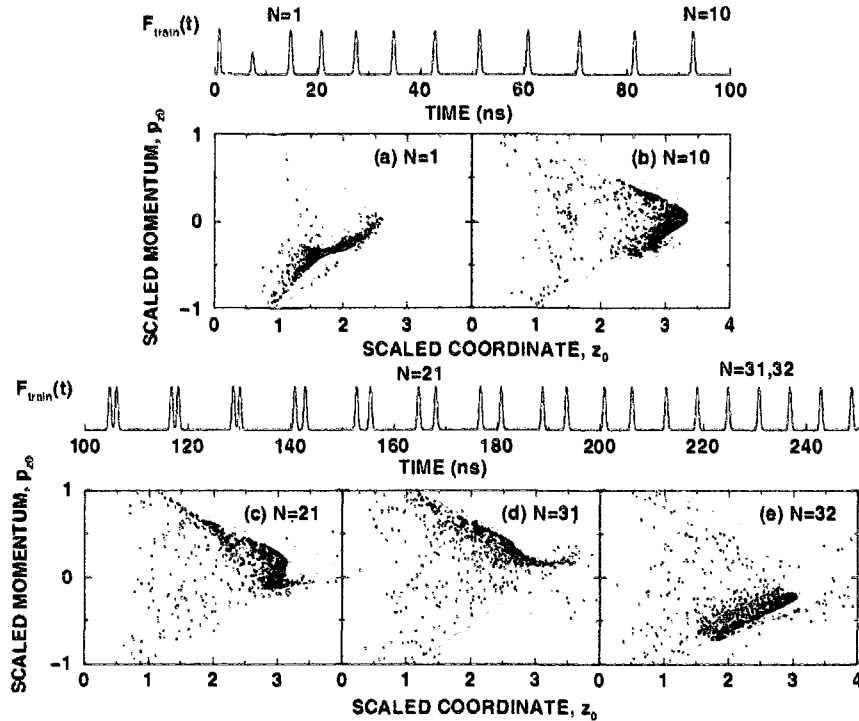
Figure 4.15 : Calculated evolution of the phase space distribution of the wavepacket for an initial mix of maximally polarized Stark states. The phase space distributions are taken at the times when the 1st, 10th, 21st, 31st, and 32nd HCPs reach their peak values. The shaded areas represent the stable eslands associated with the transient train of pulses in which the wavepacket is evolving. The colored line shows the porfile of the applied HCP sequence.

(1) Starting from a mix of quasi-1D $n_i = 350$ Stark states a transiently localized wavepacket is prepared and loaded into island A, as described in section 2.6.2, using the two weak localizing kicks. The first has a scaled stength of $\Delta p_{0L} = -0.085$. The second is applied after a delay of 6.5 ns and is of strength $\Delta p_{0T} = -0.05$.

(2) The main HCP train begins 7.4 ns later and has a scaled strength of $\Delta p_0 = -0.1$. The period of this train is incremented over the ten pulses labeled $N = 1 - 10$

according to $t_{N+1} - t_N = T + \delta T(N - 1)$, where $T = 6$ ns and $\delta T = 0.67$ ns. That is, the period is linearly increased from $T = 6$ ns to $T' = 12$ ns in increments of 0.67 ns (an interval which is set by experimental considerations). This transfers the wavepacket from island A (with $n_i \sim 350$) to island $D$ with $n \sim n_{A_1} \sim 435$.

(3) A second identical periodic train of HCPs with period $T' = 12$ ns is then superposed with an initial relative time shift $\tau = 2\delta T = 1.3$ ns. Since this separation is short compared to the electron orbital period, their combined effect is similar to that of a single pulse of twice the strength. As noted above, this leads to only small changes in the position and shape of island D. The time shift and period of these trains are kept constant for three periods (six pulses extending from $N = 11$ to 16).

(4) The wavepacket is then transferred from island D to the period-2 islands $A_1$ and $A_2$ by linearly increasing the time shift $\tau$ from 1.3 to 6 ns, again in increments of $\delta T = 0.67$ ns, over the next 12 pulses $N = 17$ - 29.

(5) Finally, for pulses $N = 30, 31,...$ the train is held fixed with $T = 6$ ns to maintain the product wavepacket in the period-2 islands.

### 4.3.3 Period-2 Island Simulations: the maximally polarized state

Figure 4.15 displays the results of CTMC simulations that show the time evolution of the wavepacket during the HCP sequence outlined above. The initial state is represented by a microcanonical ensemble of phase points that encompasses a mix of the 18 extreme redshifted states in the $n_i = 350$, $m = 0$ Stark manifold. Because

stable islands of the periodically kicked atom are observed only along the $z$ axis, this choice of initial states maximizes the overlap between the initial wavepacket and the target stable island, thus optimizing trapping efficiency. The number of parabolic states included in the initial distribution is chosen according to the effective laser linewidth. However, the precise number is not important as long as the width of the wavepacket does not exceed the transverse dimension of the stable island.
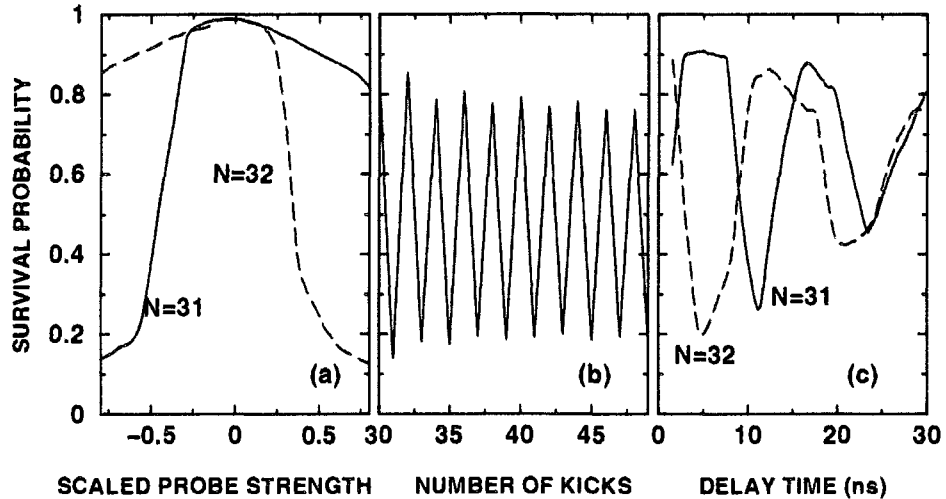


Figure 4.16 : Dependence of the calculated survival probabilities on (a) the strength and direction of the probe kicks, (b) the number of kicks $N$ in the HCP train, and (c) the delay time $\tau_{delay}$ between the end of the HCP train and applicatin of the kick. In (a) the probe HCP is applied 6 ns after the 31st (solid) and the 32nd (dashed) kicks. In (b) the train of HCPs is turned off after N kicks and the probe HCP with strength $\Delta p_{probe} = -0.8$ is applied 6 ns later. In (c) the probe HCP $\Delta p_{probe} = 0.5$ is applied after the 31st (solid) and 32nd (dashed) kicks.

The final trapped wavepacket can be examined using a probe HCP that is applied at a preselected time delay $\tau_{delay}$ following the last HCP pulse in the train. Measurements of the survival probability as $\Delta p_{probe}$ is varied provide information

on the momentum distribution of the product wavepacket[62]. This is illustrated in Fig.4.16(a), which shows the calculated survival probabilities as a function of $\Delta p_{probe}$ for a probe pulse applied 6 ns after the $N =31$ and 32 kicks. Following the 31st kick, the wavepacket is positioned within island $A_1$ having $p_z > 0$, and evolves toward island $A_2$ ($p_z < 0$) during the 6 ns delay. A negative probe pulse $\Delta p_{probe} < 0$ therefore accelerates the electron, leading to large ionization probabilities. In contrast, for $\Delta p_{probe} > 0$ the electron loses energy, greatly reducing the chance of ionization. The sudden fall-off in the survival probability around $\Delta p_{probe} = -0.5$ points to strong wavepacket localization. Following $N = 32$ kicks, the survival probability is almost a mirror image of that for $N = 31$ kicks, demonstrating that the wavepacket is localized within the island $A_2$ having $p_z < 0$.

Beyond $|\Delta p_{probe} = 0.5|$, the difference between the survival probabilities following $N = 31$ and $N = 32$ kicks becomes quite large (the difference is $\sim 70\%$). This large contrast provides a clear signature that can be used to examine how long a wavepacket can be kept trapped inside the period-2 islands. This is illustrated in Fig. 4.16(b) for a fixed scaled probe strength $\Delta p_{probe} = -0.8$ and a fixed delay time $\tau_{delay} = 6$ ns. The survival probability is calculated as a function of the number of kicks prior to the probe. The result mirrors the dynamical behaviour of the the average momentum $\langle p_z(t) \rangle$ of the wavepacket during the HCP sequence. As shown in Fig. 4.16(b), even after 50 kicks, the survival probability still oscillates between values of 0.2 and 0.8, indicating that the wavepacket is well trapped within the period-2 islands.

As noted above, the period-2 orbit involves two different energy manifolds $n_{A_1}$ and $n_{A_2}$ ($> n_{A_1}$). This energy difference can be examined using a probe HCP of fixed strength applied after different time delays following the last HCP in the train. Once the HCP train is turned off, the wavepacket evolves freely, and the survival probability exhibits periodic behavior with period $T_n = 2\pi n^3$ that is characteristic of the average principal action $n$ of the final wavepacket. Thus the periodic variations in survival probability can be mapped onto the average principal action. Prior to the 31st kick, the wavepacket is located in island $A_1$ with $p_z > 0$. During the HCP the wavepacket is is decelerated and then follows the Kepler orbit with the smaller energy $n = n_{A_1}$. In contrast, after the 32nd kick, the wavepacket is returned to the higher-energy manifold $n = n_{A_2}$. Therefore the time evolution of the wavepacket, and consequently of the survival probability, (Fig. 4.16), following $N = 31$ kicks is somewhat faster than that after the $N = 32$ kicks. The oscillation periods of approximately 12.5 and 15.3 ns correspond to population of states with $n_{A_1} \simeq 435$ and $n_{A_2} \simeq 466$.

### 4.3.4  Period-2 Islands: Experimental Realization

The protocol for transferring a wavepacket trapped in a period-1 island to period-2 is-lands outlined above requires the precise production of a complicated pulse sequence. Only with the availability of the high frequency pulse pattern generator (PPG, described in section 3.5) was this experiment possible.

Figure 4.17 shows the results of this experiment. The measured quantities are the
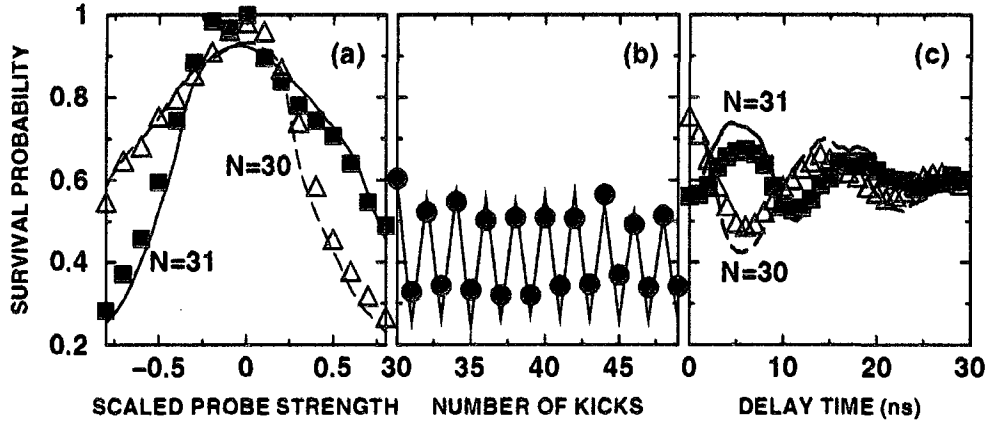
Figure 4.17 : Dependence of the measured and calculated survival probabilities on (a) the strength and direction of the probe pulse, (b) the number of kicks $N$ in the HCP train, and (c) the delay time $\tau_{delay}$ between the end of the HCP train and application of a probe pulse. The parameters are the same as used in Fig. 4.16. The open triangles show survival probabilities measured after the 30th kick, filled squares the 31st kick. Calculated survival probabilities after the 30th and 31st kick are shown in (a) and (c) by dashed and solid lines respectively. The initital wavepacket used in the CTMC simulations is a mix of 36 Stark states with $n_i = 350$, $m = 0$ centered around $k = -175$ oriented along the same axis as the applied HCPs.

same as those calculated in Fig. 4.16. The survival probability is shown as a function of strength and direction of the probe pulse, Fig. 4.17(a), the number of kicks in the HCP train, Fig. 4.17(b), and the time delay $\tau_{delay}$ between the end of the HCP train and the probe pulse, Fig. 4.17(c). Although the results are qualitatively very similar to those in Fig. 4.16, the observed effect is less dramatic. There are a number of factors that might account for this. The results in Fig. 4.16, were derived using a mix of the extreme maximally polarized redshifted states in the Stark manifold which have an average dipole $\langle d_0 \rangle \sim -1.5$. Although the laser frequency can, in principle, be tuned to excite these states, this is diffcult because the associated oscillator strengths

are very small. Also, the effective laser linewidth is broadened by beam divergence and Doppler effects to $\sim$12 MHz and therefore overlaps a number of Stark states, many of which have larger oscillator strengths and can be more effciently excited[50]. These are centered around $k \sim -291$ and have an average scaled dipole moment of $\langle d_0 \rangle \sim -1.25$. $^{39}K$ also has two ground state hyperfine levels $4s(F = 1)$ and $4s(F = 2)$, that are shifted relative to one another by 462 MHz. Excitation from these levels gives rise to two different Rydberg series, i.e., two different excitation spectra. The present excitation wavelength is selected such that, in zero field, peaks from the two spectra overlap, leading to excitation of $n = 350$ states from the $F = 2$ level and fewer $n = 347$ states from the $F = 1$ level. Thus, given their similar Stark splittings in a field, the same mix of Stark states should be created for both. The potassium beam, however, also contains $\sim$7% of $^{41}K$. Depending on the size of the isotopic shifts, Stark states with even an opposite orientation of the average dipole moment might be created, which could signifcantly decrease the overall average dipole moment. Furthermore, while stray fields in the experimental region can be reduced to less than $50\mu$Vcm$^{-1}$, their presence can lead to uncertainties in the magnitude and direction of the applied Stark field. These factors point to an average dipole moment somewhat below the value $\langle d_0 \rangle \sim -1.25$. Consistently good agreement between the experimental data and CTMC simulations is obtained, assuming an ensemble of initial states with an averaged scaled dipole moment of $\langle d_0 \rangle \sim -0.75$, i.e., with a mix of $k$ values centered at $k \sim -175$. A reduced dipole moment leads to a less asymmetrical

dependence of the survival probability on probe direction and strength following even and odd numbers $N(N > 30)$ of applied kicks (Fig. 4.17). As expected, however, the asymmetry is reversed upon reversing the direction of the probe. As evident from Fig. 4.17(b), the predicted strong period-2 variations in survival probability are clearly seen. Little damping of these oscillations is evident with increasing N, indicating that a sizable fraction of the initial wave packet is transferred to, and remains trapped within, the period-2 islands. Furthermore, Fig. 4.17(c) shows that the time evolution of the final product state depends markedly on whether the pulse train contains an even or odd number of kicks, demonstrating that two different energy manifolds are indeed involved in the period-2 motion.

# Chapter 5

# Rydberg Atom Wavepackets in Two Dimensions
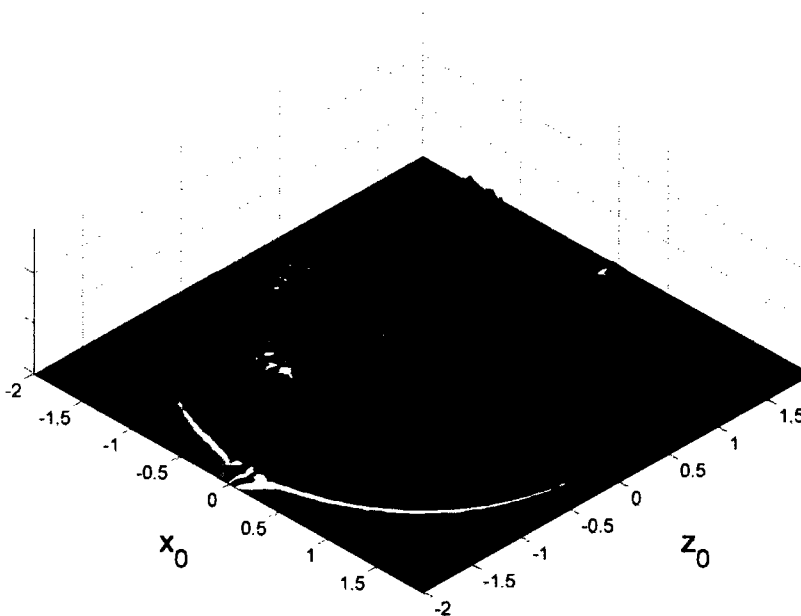


Figure 5.1 : Spatial probability density of $n = 306$ near-circular state.

## 5.1 Early attempts at two-dimensional wavepackets

The most simplistic approach to creating a localized wavepacket in two dimensions is

to first begin with the well characterized quasi-1D state (see section 2.5). By applying

an HCP to the quasi-1D state directed orthogonal to the axis of orientation, the initial

state will be projected into a two-dimensional elliptical state. The final ellipticity is determined by the size of the orthogonal HCP and the initial momentum distribution of the quasi-1D state along the axis of orientation ($z$-direction). This can be done in a more controlled fashion by taking advantage transient phase space localization (see section 2.6.1) before applying the orthogonal kick 6.5 ns later at the time of transient phase space localization.
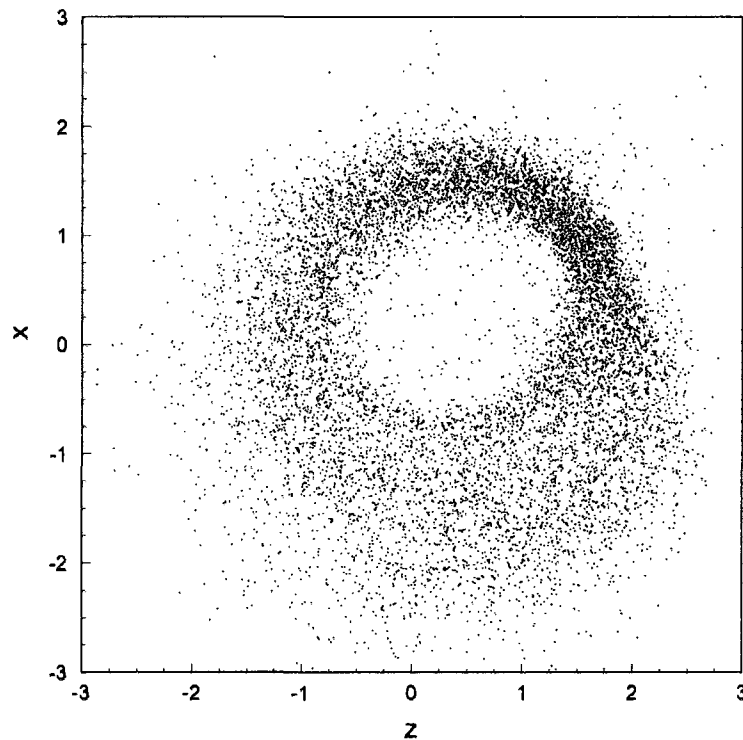


Figure 5.2 : Spatial point density plot showing the final spatial distribution following application of a $\Delta p_0 = 0.75$ orthogonal HCP to a transiently localized $n = 350$ quasi-1D atom.

Exploration of this technique to transfer the initial quasi-1D state to a higher angular momentum state has been met with rather limited success. Figure 5.2 shows

the equilibrium spatial distribution following application of such an orthogonal HCP. While the resulting wavepacket clearly has a much higher average angular momentum, the distribution of angular momentum is quite broad. In addition, the energy distribution is also very broad, and the resulting wavepacket packet dephases in less than two orbital periods, thus prohibiting the use of this wavepacket as a parent state for further manipulation and control. It is clear that another protocol for transforming the quasi-1D state into a localized 2D state is required.

## 5.2    Production of Bohr-Like Circular Wavepackets

### 5.2.1    Theory of the production of near-circular wavepackets

A solution to this problem is suggested by Fig. 5.3. The quasi-1D parent state is a very low angular momentum state. If the angular momentum could be transformed, the resulting system would then be a well defined near-circular state (essentially an ideal candidate for 2D dynamical studies). This angular momentum transformation can be achieved using an effect known as Stark precession. Stark precession can be illustrated by following the evolution of a single elongated Coulomb orbit when exposed to a transverse electric field $F_z^{pump}$. The dynamics of the electron is governed by the Stark Hamiltonian

$$H^{Stark}(t) = H^{at} + zF_z^{pump} = \frac{p^2}{2} - \frac{1}{r} + zF_z^{pump} \qquad (5.1)$$

where $H^{at}$ is the field free atomic Hamiltonian. To first order in $F_z^{pump}$, the angular
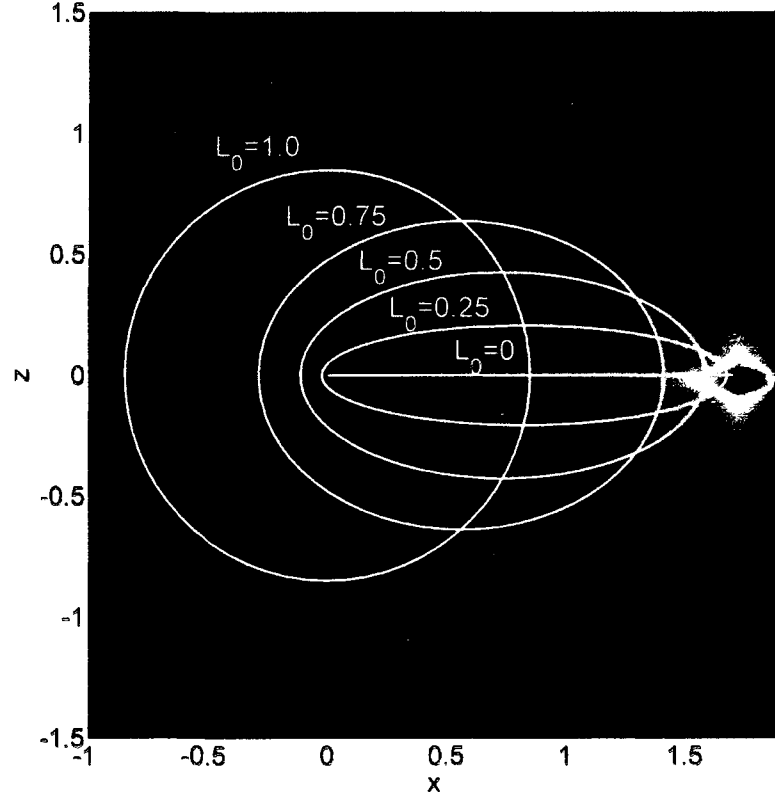
Figure 5.3 : Spatial probability density of $n = 306$ quasi-1D atom. Superimposed are elliptical orbits with varying scaled angular momentum, $L = 0.0 - 1.0$.

momentum $\vec{L} = \vec{r} \times \vec{p}$ and the Runge-Lenz vector $\vec{A} = \vec{p} \times \vec{L} - (1/r)\vec{r}$ precess about the axis of the pump field according to the Bloch equations[61, 63]

$$\frac{d}{dt}\left(\vec{L} \pm n\vec{A}\right) \simeq \frac{\pm\omega_s(t)}{2}\left(\vec{L} \pm n\vec{A}\right) \times \hat{z} \tag{5.2}$$

where $n = 1/\sqrt{-2H^{at}}$ and $\omega_s(t) = 3nF_z^{pump}(t)$ is the Stark frequency which coincides with the energy splitting between adjacent Stark states. If the pump field is static, the $z$-components of $\vec{L}$ and $\vec{A}$, $L_z$ and $A_z$ are constants of the motion. However,

the dynamics of the other components, $L_x$, $L_y$, $A_x$, $A_y$, resemble that of a harmonic oscillator.
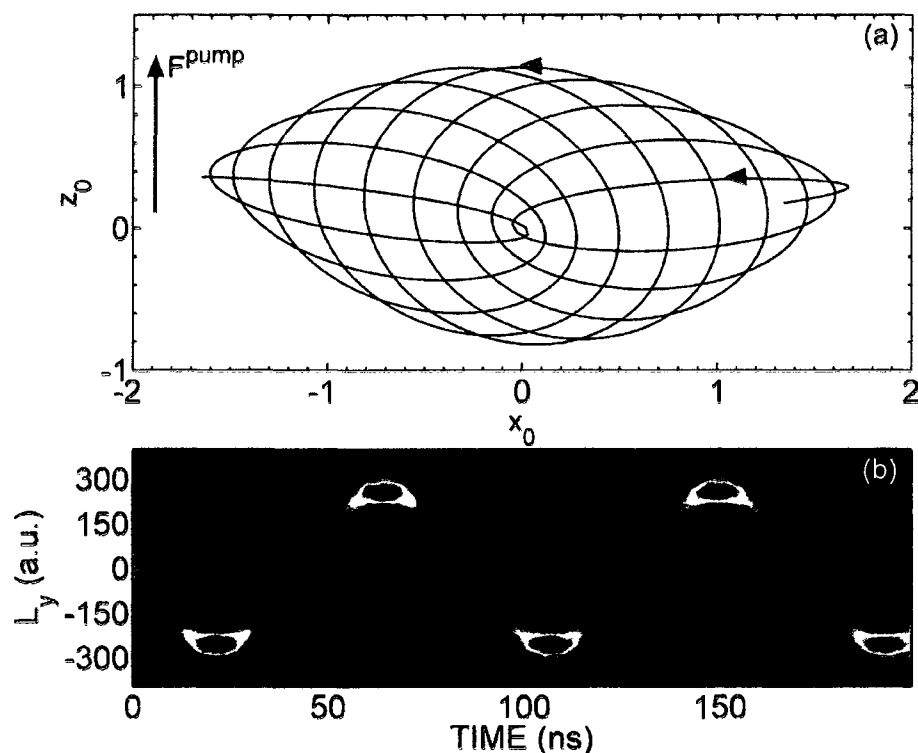


Figure 5.4 : Stark precession in a static field. (a) trajectory of a classical electron in a coloumb orbit precessing in a transverse electric field. (b) $L_y$ distribution of a quasi-1D atom in a transverse electric field.

Figure 5.4(a) shows the evolution of a classical electron trajectory in a static pump field. The electron is initially in a highly elliptical orbit. This classical orbit is analogous to the initial probability density of a quasi-1D state. Notice that as the electron evolves, the orbit changes from being highly-elliptical to nearly circular on a time scale of half of a Stark period. As the electron continues to evolve, the orbit

again becomes elliptical, but with the Runge-Lenz vector in the opposite direction.

The evolution of the $L_y$ distribution of an $n \sim 306$ quasi-1D atom in a transverse Stark field is illustrated in Fig. 5.4(b). The value of $L_y$ is initially near zero. However, as the atom evolves in the field, the distribution oscillates sinusoidally between extreme values in $L_y$ of -270 and +270 which corresponds, respectively, to an electron traveling anticlockwise or clockwise around a near circular orbit. The distribution remains narrow during this process. Rapidly switching off the pump field at the times of extreme values in $L_y$ "freezes" the distribution, leaving the atom in a near circular state. This operation is similar to the "$\pi/2$ pulse" used to manipulate nuclear spins[64]. Remarkably as the resulting wavepacket evolves it undergoes strong transient localization in azimuth.

This is illustrated in Fig. 5.5 which shows calculated snapshots of the spatial probability density at the time of optimum localization following application of a field $F_z^{pump}$ that is turned off after 22 ns, i.e. when $L_y$ first reaches its largest negative value. A localized wavepacket is evident that moves anticlockwise in a near circular orbit.

As seen in Fig. 5.6, which shows the time evolution of both the electron angular and radial distributions, the wavepacket remains well-localized for several orbits. It evolves with near constant radius and, since its angular position depends linearly on time, with constant angular velocity and momentum. The localization of the wavepacket in azimuth initially improves with time becoming optimum $\sim 7 - 12$ ns
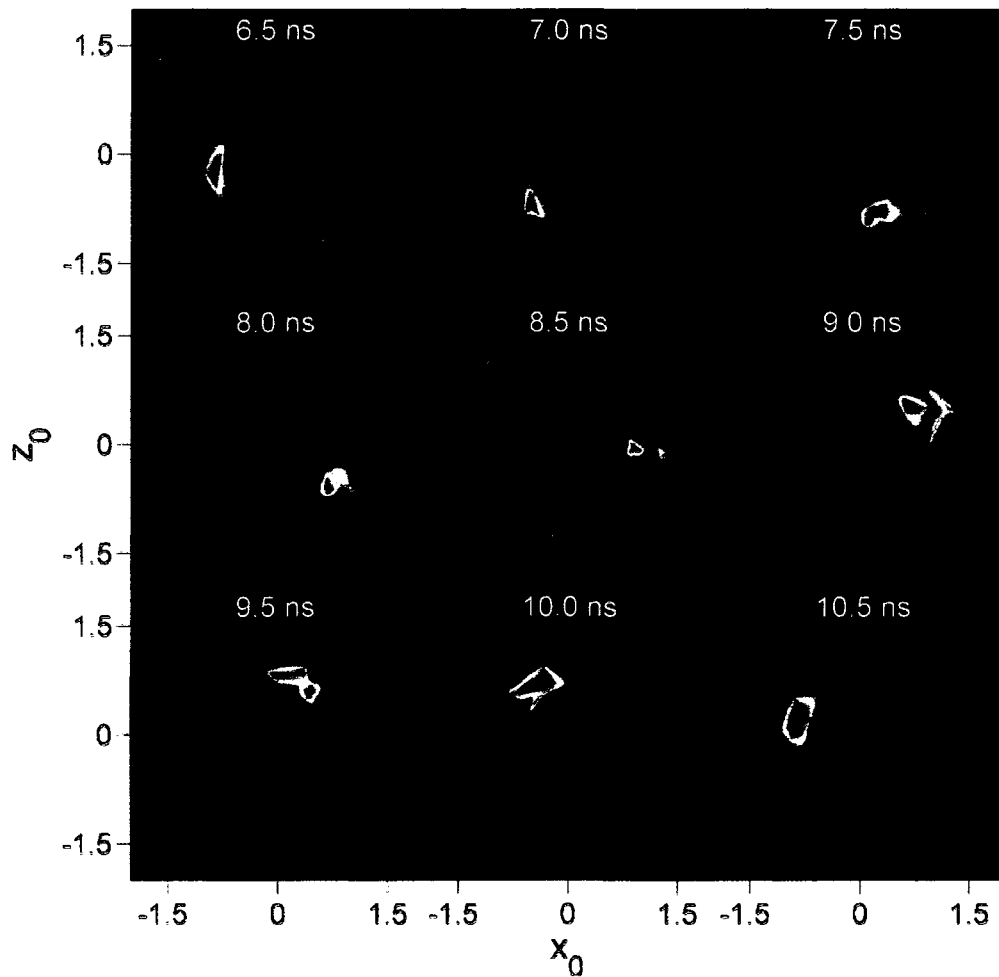
Figure 5.5 : Snapshots showing the evolution of the resulting near-circular wavepacket following application of a pump field $F_z^{pump} = -20$ mV/cm for 22 ns to quasi-1D $n_i = 306$ atoms. These are taken at the times shown following the turn-off of $F_z^{pump}$

after turn-off of the pump field. At this time, the full width half maximum of the angular distribution is about 1 radian. The position of the center of the wavepacket moves in an approximately circular orbit given by

$$(x(t), z(t)) \simeq n^2(\cos(\omega_n t + \delta), \sin(\omega_n t + \delta)) \tag{5.3}$$
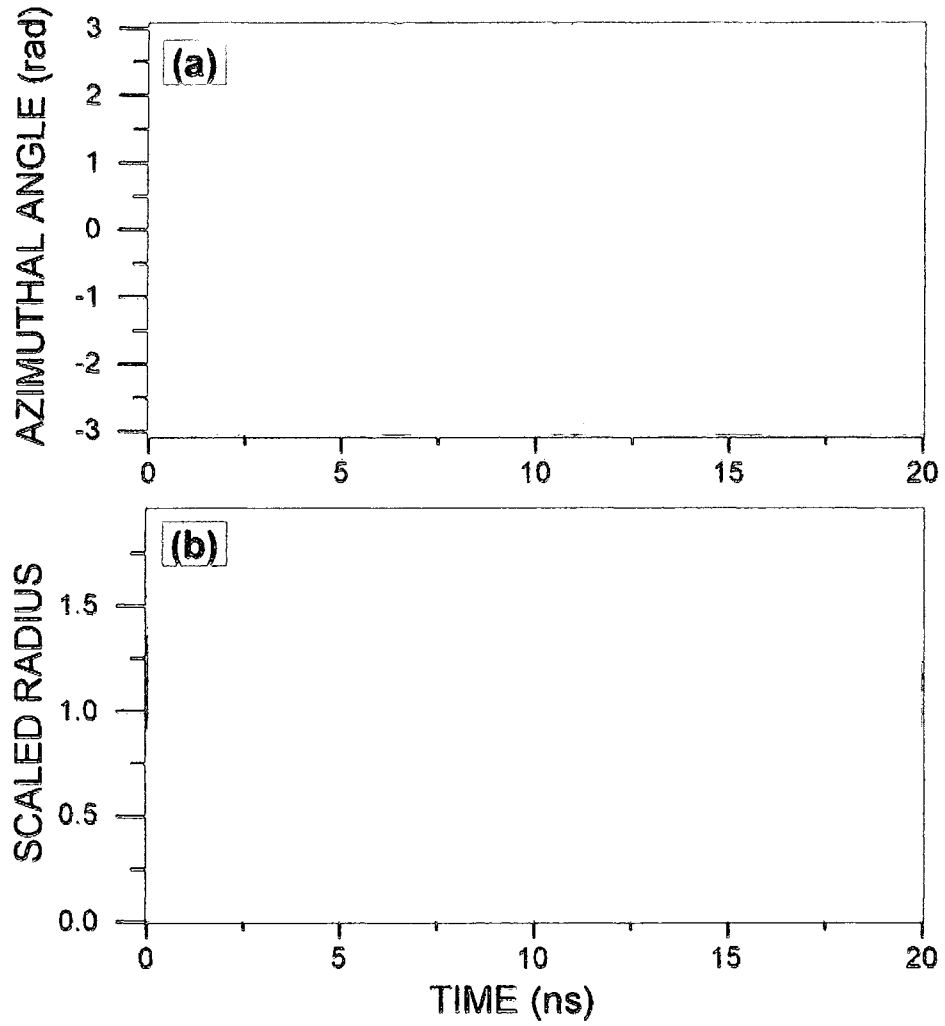
Figure 5.6 : Time dependence of (a) the angular and (b) the radial distributions of the wavepacket following turn-off of a pump field of -20 mV/cm applied for 22 ns.

where $\delta$ is a constant phase shift, and $\omega_n = n^{-3}$ is the angular frequency. The momentum components, given by

$$(p_x(t), p_z(t)) \simeq n^{-1}(-\sin(\omega_n t + \delta), \cos(\omega_n t + \delta)) \tag{5.4}$$

are 90° out of phase with the spatial coordinates.
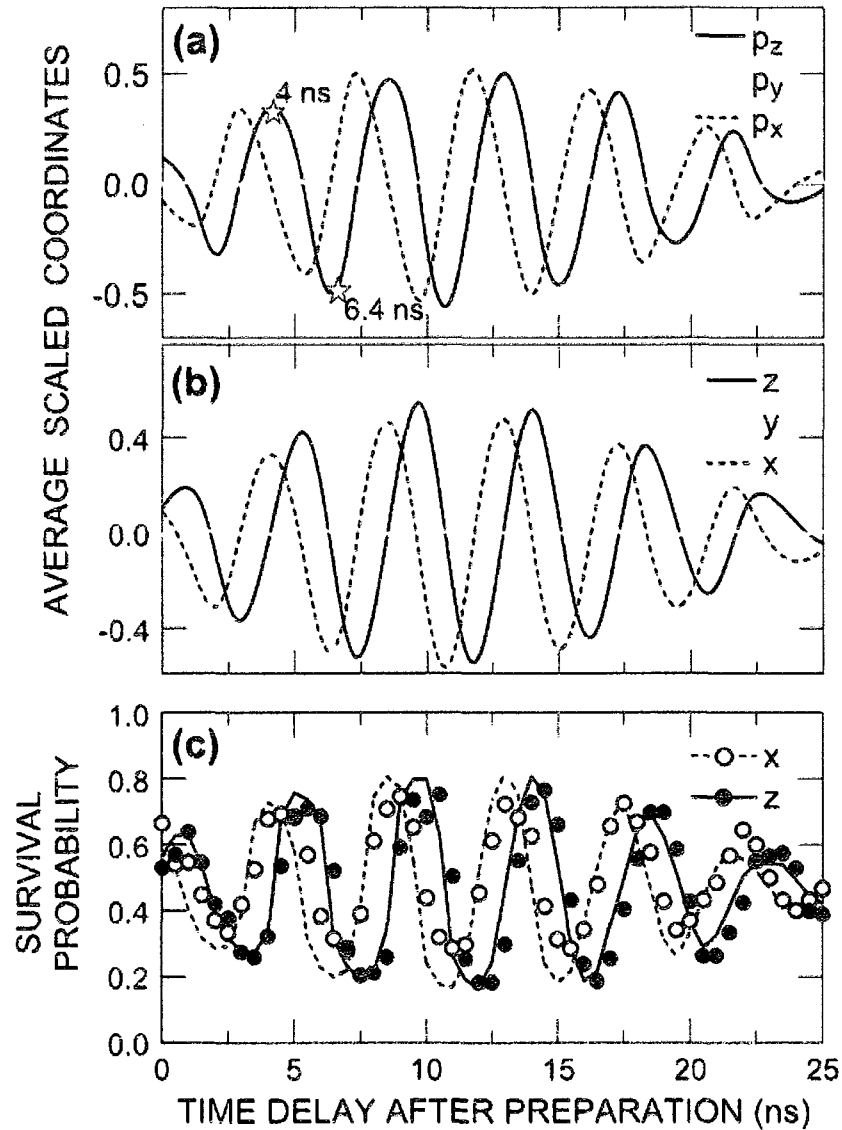


Figure 5.7 : Time dependence of (a) the momentum coordinates, (b) the position coordinates, and (c) the experimental (symbols) and calculated (lines) survival probabilities following turn-off of a pump field $F_z^{pump} = -20$ mV/cm applied for 22 ns. The stars in (a) indicate the times at which the momentum is probed in Fig. 5.9.

Figures 5.7 (a) and (b) show the time evolution of the calculated expectation values of momentum and position respectively. These values closely mirror Eqs. 5.3 and 5.4. Both $\langle y(t) \rangle$ and $\langle p_y(t) \rangle$ remain very close to zero, however, strong oscillations are observed for $\langle x \rangle$, $\langle z \rangle$, $\langle p_x \rangle$, and $\langle p_y \rangle$, which is consistant with motion in the $xz$ plane.

## 5.2.2 Experimental Realization of Bohr-like wavepackets in near-circular orbits
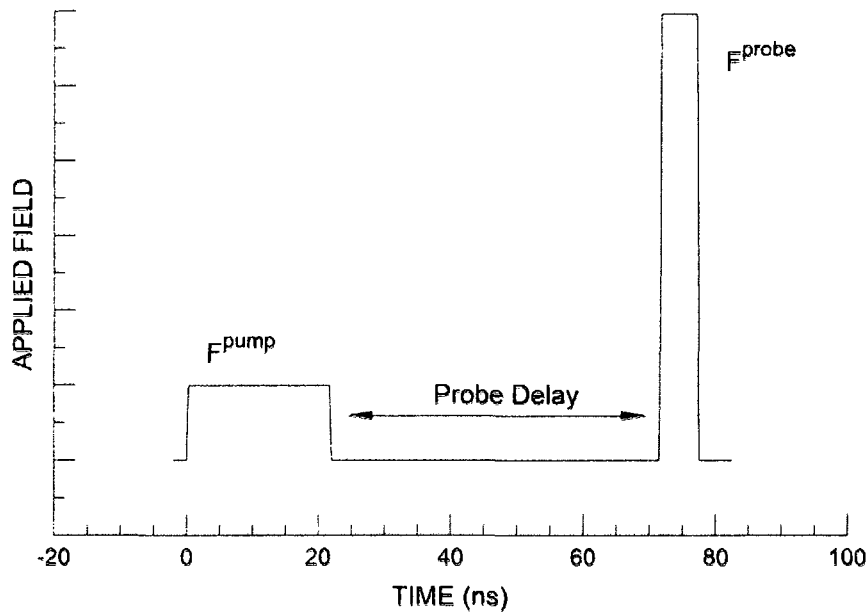


Figure 5.8 : Pulse sequence used to experimentally observe the evolution of the near circular wavepacket.

To create Bohr-like wavepackets experimentally, an $n = 306$ quasi-1D atom was prepared along the $+x$ direction. A pump field of -20 mV/cm is applied suddenly

along the $z$ direction. The rise time of the applied field was less than 300 ps. After a predetermined time, the field is rapidly turned off ($t_{off} < 300$ ps). The subsequent evolution of the wavepacket is monitored using probe pulses applied along the $x$ or $z$ directions as shown in Fig. 5.8. The remaining atoms (and thus survival probability) are then detected using selective field ionization. Applying a probe "field step" at $t = t_p$, i.e. rapidly turning on a constant electric field, indirectly probes the electron position coordinates by ionizing those electrons whose coordinates $z(t_p)$ [or $x(t_p)$] are such that their energy $-1/(2n^2) + z(t_p)F_z^{probe}$ [or $-1/(2n^2) + x(t_p)F_x^{probe}$] lies above the top of the field ionization barrier ($-2|F^{probe}|^{1/2}$) generated by the probe pulse[65]. In this case a probe field of 100 mV/cm and 6 ns duration ($T_n$) is used.

Figure 5.7(c) shows both the experimental (symbols) and calculated (lines) results of such an experiment when probing along both the $x$ and $z$ directions. In both cases, strong oscillations in survival probability are observed. The experimental data are in excellent agreement with the CTMC simulations. Also, as expected, the survival probability as a function of probe delay ($t_p$) closely mirrors the evolution of the spatial coordinates, $\langle x(t) \rangle$ and $\langle z(t) \rangle$. Equation 5.3 shows that a 90° phase shift between orthogonal coordinates is one of the signatures of circular motion. This phase shift is visible present in the data. The oscillations persist for several orbits but ultimately dephase due to the distribution of excited states within the wavepacket (see Sect. 5.2.3).

The experiment described above provides information about the evolution of the

average spatial coordinates. It is possible, however, to obtain further verification of near circular motion by probing the momentum distribution of the wavepacket using a short (impulsive) HCP. Ionization caused by the HCP depends on the momentum distribution of the wavepacket at the time of the pulse application. If the electron is located on the $+x$ axis moving in the $+z$ direction, a pulse in the $+z$ direction will accelerate the electron and increase its energy, when even relatively small probe pulses will cause significant ionization. In contrast, if the electron is located on the $+x$ axis and traveling in the $-z$ direction the same small pulse in the $+z$ direction will decelerate the electron leading to stronger binding to the core. In this case, only when the pulse is large enough to accelerate the electron in the reverse direction, will the electron gain enough energy to be ionized. As a result, much larger probe pulses are required to induce significant ionization. The times at which these conditions occur are marked with stars on Fig. 5.7(a). The first star (located at 4 ns) marks a time where the wavepacket is located on the $+x$ axis and is traveling in the $+z$ direction. The second star (6.4 ns) marks the time where the wavepacket has evolved to the opposite position in the orbit ($-x$ axis, traveling in the $-z$ direction). At each of these times, a short duration (800 ps) probe pulse is applied in the $+z$ direction, and the survival probability is measured as a function of probe strength.

Figure 5.9 shows the results of such an experiment. The insets on the figure show the spatial distributions of the wavepacket at the time the probe pulses are applied. The white arrow on each inset shows the direction of motion of the wavepacket. As
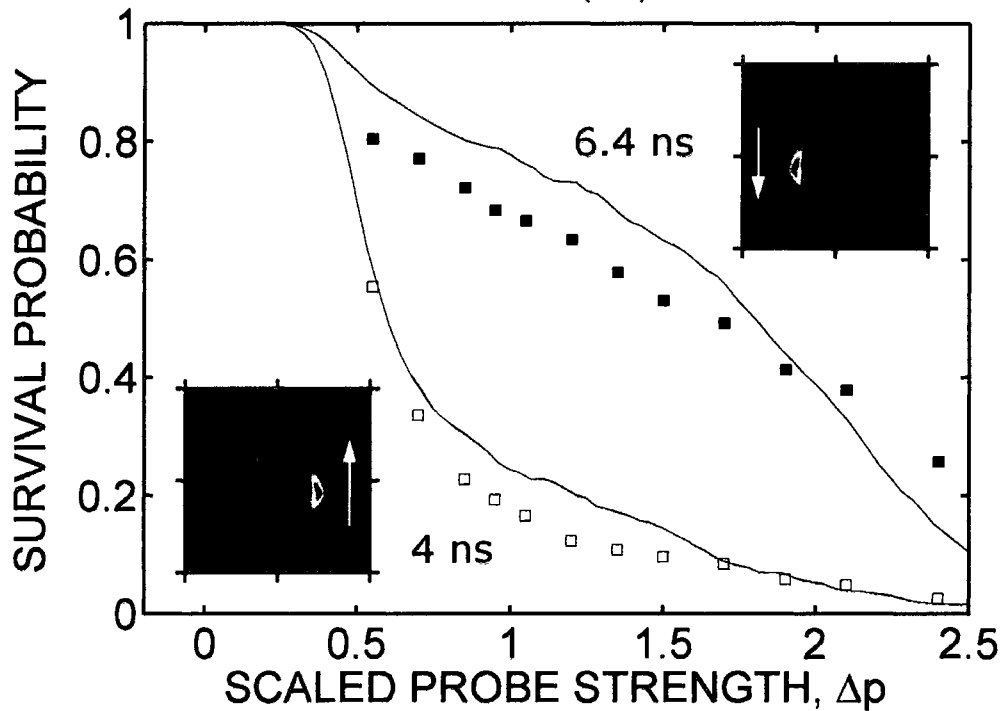
Figure 5.9 : Survival Probability versus the strength $\Delta p$ of a probe pulse applied in the $+z$ direction when the wavepacket is on the $+x$ axis moving in the $+z$ direction (4 ns) and on the $-x$ axis moving in the $-z$ direction (6.4 ns). The preparation of the wavepacket is identical to the conditions in Fig. 5.7. Both experimental (symbols) and CTMC results (lines) are shown.

expected, the two different times yield very different ionization profiles. When the probe pulse is applied at 4 ns, the survival probability decreases sharply as $\Delta p$ is increased. In the second case, 6.4 ns, as the probe strength is increased, the survival probability drops more slowly. In this case a scaled impulse of $\Delta p = 2.0$ is required to reach 50% ionization whereas in the earlier case, this ionization level is reached with a probe strength of only $\Delta p = 0.6$. These measurements indicate that the momentum distribution is localized, consistent with near circular motion.
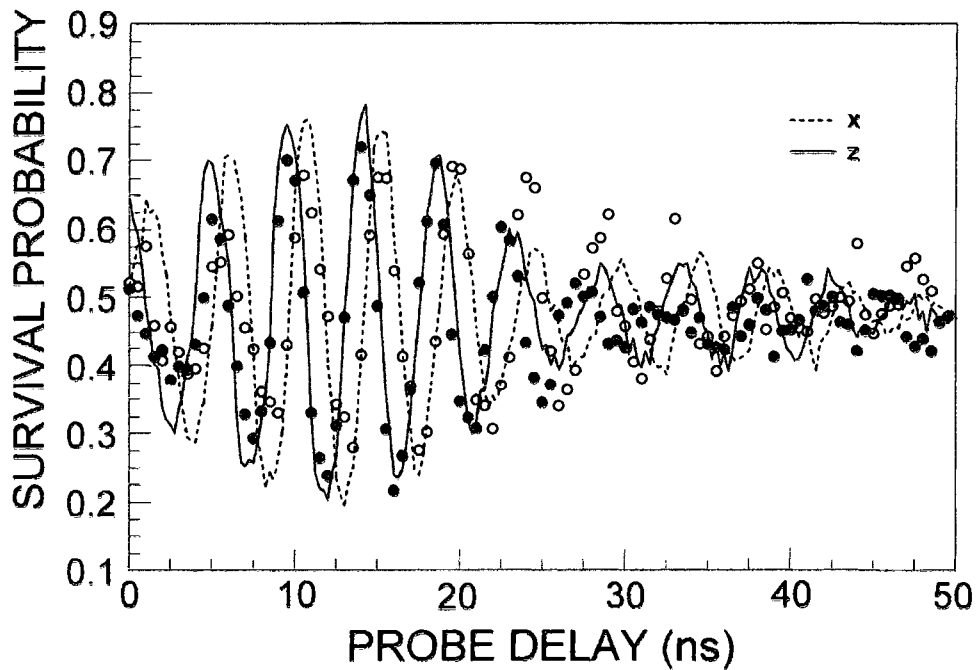
Figure 5.10 : Survival probability vs probe delay in the $x$ and $z$ direction following application of a 66 ns duration 20 mV/cm pump field. Both experimental (symbols) and CTMC results (lines) are shown.

If the duration of the 20 mV/cm pump field is increased to 66 ns (as opposed to the 22 ns duration used in the preceeding discussion), then the resulting value of $L_y$ is +270 instead of the extreme negative value -270, corresponding to a wavepacket moving clockwise about the core in the $xz$ plane. Experimentally this was confirmed by probing in the $x$ and $z$ directions as in Fig. 5.7(c), except with a pump field duration of 66 ns. The results, shown in Fig. 5.10, are very similar to those in Fig. 5.7(c). Careful inspection shows that sinusoidal oscillation in the $x$ direction now leads the $z$ data by 90°. This result is consistent with a reversal in the direction of rotational motion.

### 5.2.3 Wavepacket dephasing and the effect of the pump pulse shape

When the pump field $F_z^{pump}$ is suddenly turned off, thus locking in the maximum angular momentum distribution, it is not unexpected that the resulting orbit will be near circular. However, it is not clear that the wavepacket resulting from this angular momentum transformation should undergo transient localization. Prior to the pump field application, there is no preparatory pulse causing transient localization[1]. Yet after the pump pulse, a transiently-localized non-stationary wavepacket is formed. As will be discussed, this localization results from small position-dependent changes in the electron energy associated with the (sudden) turn off of the pump field which translates into a position dependence in the subsequent orbital frequencies, $\omega(\phi_i)^{-3}$. When that part of the ensemble orbiting at the higher frequencies catches up with that part orbiting more slowly the ensemble becomes transiently localized forming a Bohr-like wavepacket in a nearly circular orbit[66].

Focusing of the distribution occurs as the faster moving (lower-$n$) components catch up with the slower moving (higher-$n$) components. The time required to reach maximum localization, or focusing, depends on the width of the energy distribution following pump field turn-off. In addition, the time for which the wavepacket remains localized also depends on the energy distribution.

---

[1] An attempt to pre-localize the Rydberg atom electron prior to application of the pump pulse $F_z^{pump}$ actually resulted in a reduced wavepacket lifetime. The application of the localization pre-pulse introduced energy broadening which increased the rate of dephasing.

The final energy distribution depends very strongly on the shape of the applied pump field, $F_z^{pump}(t)$. Because $H^{Stark} = H^{at} = E$ for zero field (which is the case both before and after the pump field), the pulse shape dependence of $\Delta E$ can be derived from the dynamics of the Stark interaction using the equation

$$\frac{dH^{Stark}}{dt} = z(t)\frac{dF_z^{pump}(t)}{dt} \qquad (5.5)$$

We begin this analysis by considering the simplest case of a square shaped pump pulse, $(t_{rise} = t_{fall} = 0)$. The value of $H^{Stark}$ (defined as $H^{Stark} = z(t)F_z^{pump}(t)$), for a quasi-1D state elongated in the $x$-direction (for which $z \simeq 0$) remains essentially unchanged during the sudden turn on of the pump field. However, after precession, the orbit emcompasses a range of $z$ coordinates and the Stark interaction becomes strongly dependent on the fall time $t_{fall}$. When the pump field is turned off suddenly at $t = t_{off}$, the wavepacket is spread around a circular orbit $(z(t_{off}) = n^2 \sin\phi$, where $\phi = \arctan z/x)$, the final energy of the electron is

$$E^{sudden}(\phi) = -\frac{1}{2n_i^2} + F_z^{pump} z(t_{off}) \simeq -\frac{1}{2n_i^2} + F_z^{pump} n_i^2 \sin\phi \qquad (5.6)$$

The $\phi$ dependence of the energy, $E(\phi)$, leads to a final energy distribution of width $\Delta E$. The largest energy change occurs when $\phi = \pm\pi/2$ resulting in a width of

$$\Delta E = 2|F_z^{pump}|n_i^2 \qquad (5.7)$$

The time $t_L$ at which the circular wavepacket achieves maximum localization (and

therefore the overall lifetime) can be increased by decreasing the strength of the pump field, $|F_z^{pump}|$. This results because the final energy energy width, $\Delta E$ is linearly dependent on $|F_z^{pump}|$, thus $t_L \propto 1/\Delta E \propto 1/|F_z^{pump}|$.

The verification of this theoretical prediction is a rather straightfoward experiment. As the magnitude of the pump pulse, $|F_z^{pump}|$, is varied the width of the pulse must also vary to maintain a constant area so that the final $L_y$ distribution remains constant. The results for two different pump pulses are shown in Fig. 5.11. The pump pulse used in Fig. 5.11(a) and (b) is the same that is used in Sect. 5.2.2, a magnitude of $F_z^{pump} = -20$ mV/cm with a duration of 22 ns. The result of applying a pump pulse with a magitude of $F_z^{pump} = -10$ mV/cm with a duration of 43 ns is shown in Fig. 5.11(c). Just as before, the experimental results show outstanding agreement with CTMC results. Also the strong sensitivity of $t_L$ on the magnitude of the pump field is quite evident. With the -20 mV/cm pump field, the wavepacket reaches maximum localization at $\sim 12$ ns. But when the pump pulse amplitude is reduce by half, the localization time increases to near 30 ns.

The measurements of $t_L$ as a function of pump pulse strength are shown explicitly in Fig. 5.12 along with the results of CTMC calculations. The optimum localization time measurements were taken at pump probe magnitudes $|F_z^{pump}| = $ -5, -10, and -20 mV/cm. Again, excellent agreement is seen between the measured values and the CTMC results. Both the measured and calculated localization times show the expected $1/|F_z^{pump}|$ dependence predicted by calculations of energy width $\Delta E$.
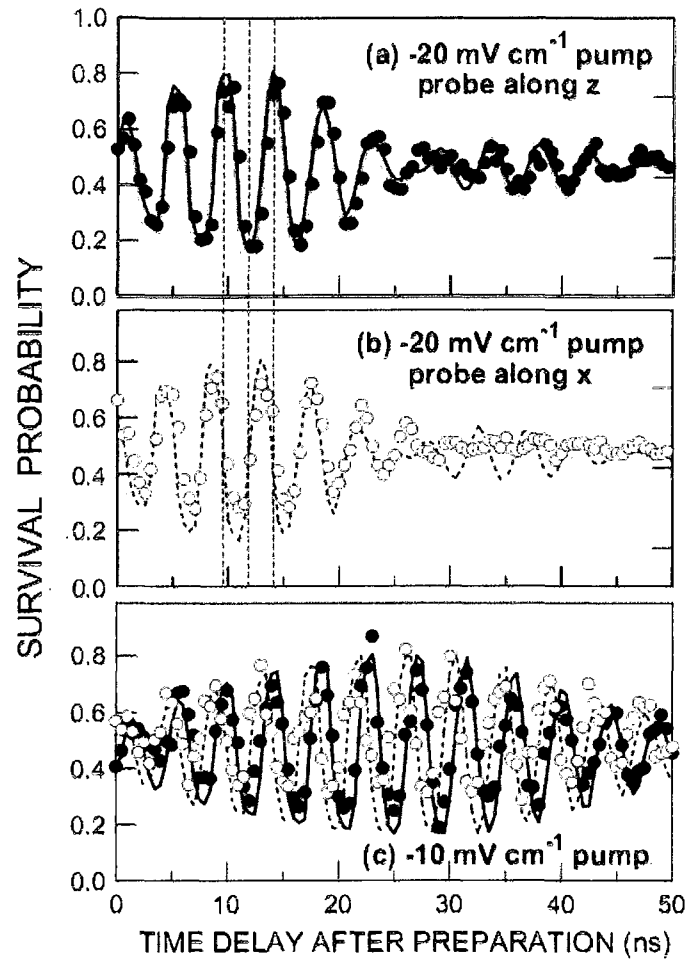
Figure 5.11 : Survival probability as a function of the time delay between the pump pulse turn off time and application of a 6 ns duration 100 mV/cm probe pulse. (a) $F_z^{pump} = -20$ mV/cm and the probe pulse applied along the $z$ axis. (b) $F_z^{pump} = -20$ mV/cm and the probe pulse applied along the $x$ axis. (c) $F_z^{pump} = -10$ mV/cm and the probe pulse applied along the $x$ and $z$ axes. Also shown in (a) and (b) are the expectation values of $x$ and $z$. The vertical lines are shown to visualize the 90° phase shift between $x$ and $z$ coordinates shown in (a) and (b). Both the pump and probe fields were turned on and off suddenly.

The analysis of the width of the energy distribution can be extended to include

finite rise and fall times. If the rise and fall times are short compared to the Stark
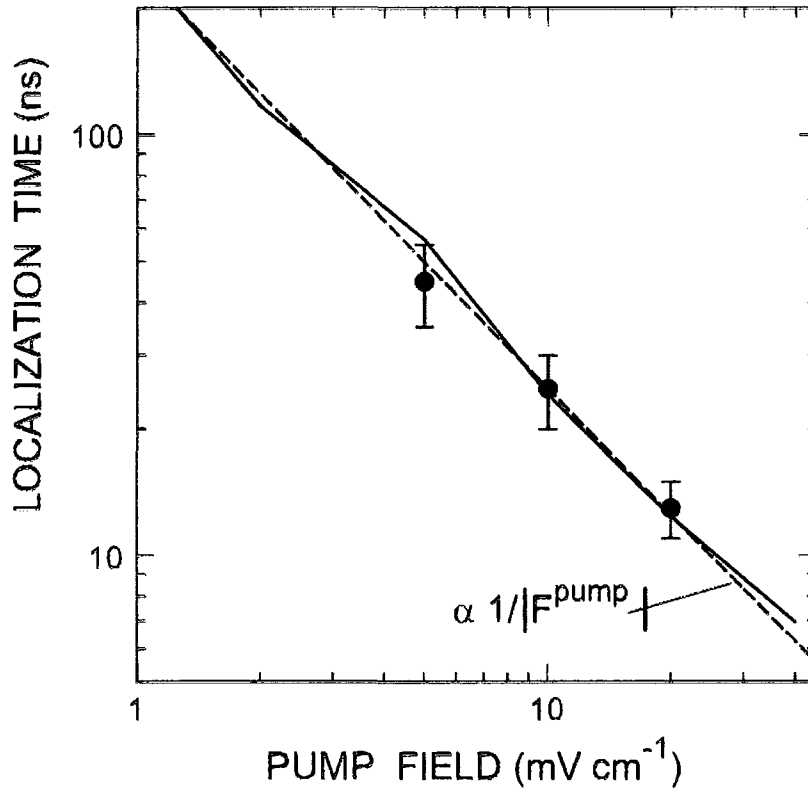
Figure 5.12 : Experimental (symbols) and calculated (lines) optimum localization times as a function of the strength of the pump pulse. Both pump pulse and probe pulse are turned on and off suddenly, $t_{rise} = t_{fall} < 500$ ps. The dashed line illustrates the $1/|F_z^{pump}|$ behavior.

period $T_S$ ($T_S = 85$ ns for $|F_z^{pump}| = -10$ mV/cm), the final energy width can be determined from the change in $H^{Stark}$ during the fall time $-t_{off}/2 < t - t_{off} < t_{off}/2$, i.e., integrating Eqn. 5.5 for a trajectory on a fixed circular orbit $z(t) = n_i^2 \sin(t/n_i^3)$. The shape of the pulse during the rise and fall is important to the final result. The most straightfoward approach is to use a simple linear rise and fall. However, measurements of the experimental pulse shapes show more curvature than a simple linear
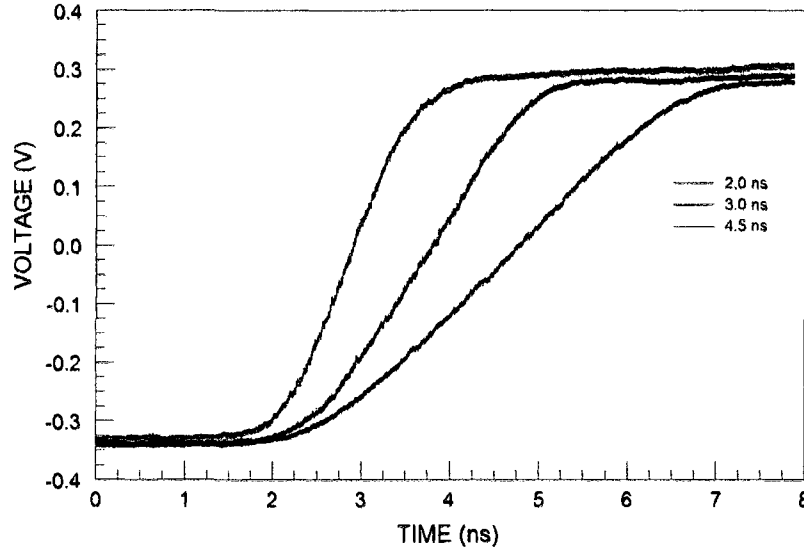
Figure 5.13 : Measured pump pulse rising edges for 2.0, 3.0, and 4.5 ns rise times.

rise(see Fig. 5.13). As a better approximation of the experimental pulse profiles a

sine-like fall ($F(t) \propto 1 - \sin \pi(t - t_{off})/t_{fall}$) is also considered. The following are the

summarized results from integration of Eqn. 5.5 assuming an approximately circular

orbit during the fall time. For a linear turn off,

$$n_i^2 \Delta E \simeq 2n_i^4 |F_z^{pump}| \left| \frac{\sin (\pi t_{fall}/T_{n_i})}{\pi t_{fall}/T_{n_i}} \right| \tag{5.8}$$

while a sine-like turn off yields

$$n_i^2 \Delta E \simeq 2n_i^4 |F_z^{pump}| \left| \frac{\cos (\pi t_{fall}/T_{n_i})}{1 - (\pi t_{fall}/T_{n_i})^2} \right| \tag{5.9}$$

Figure 5.14 shows the result of experimentally varying the fall time of the pump

pulse. As the fall time of the pump pulse is increased, the maximum localization
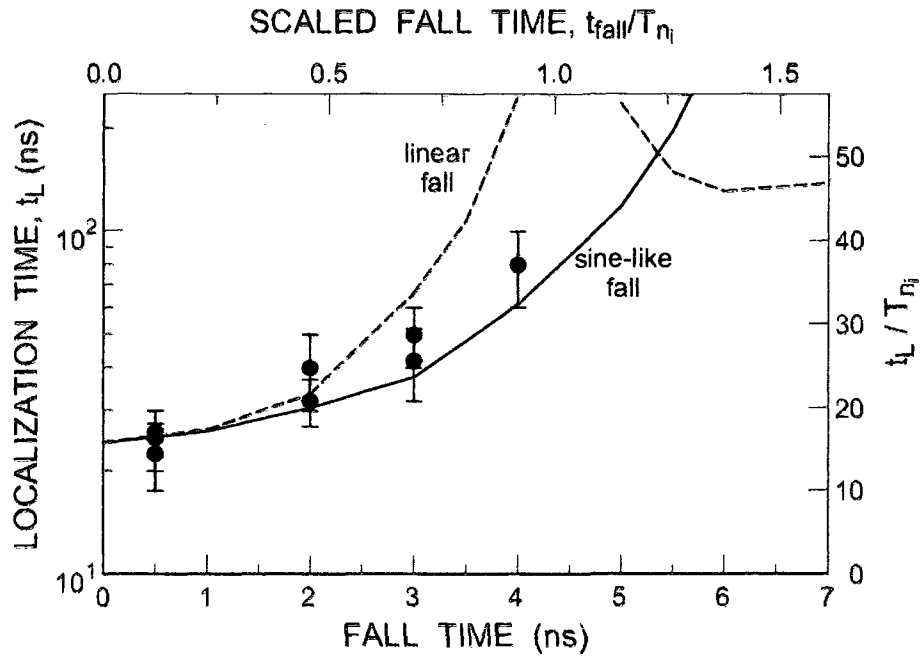
Figure 5.14 : Experimental (symbols) and calculated (lines) maximum localization times for $F_z^{pump} = -10$ mV/cm as a function of fall time for a linear (dashed line) and sine-like fall (solid line).

time increases rather dramatically. As expected, the experimental data are better predicted using the sine-like transition. However, overall the agreement between the experimental and calculated results is quite good.

## 5.3 Pulse-Induced Wavepacket Re-Localization

The above section discusses the formation and dephasing of the near-circular wavepackets resulting from the turn off of the transverse pump field $F_z^{pump}$. However, the static quasi-equilibrium state following the dephasing of such wavepackets is also of consider-

able interest as a laboratory for studying driven dynamics in two-dimensional atomic systems. The simplest first experiment along these lines is to examine the behavior resulting from the application of a single unidirectional HCP.
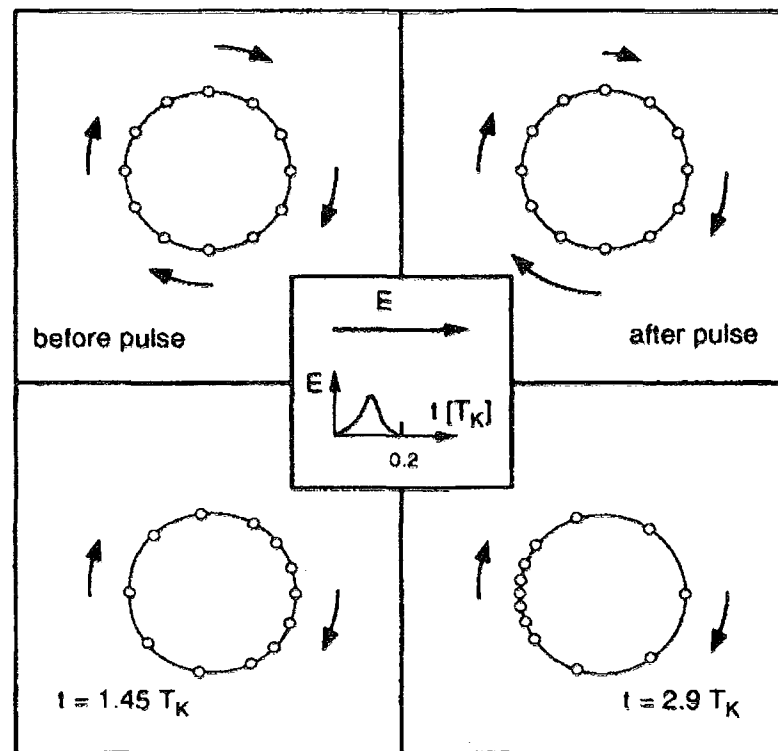


Figure 5.15 : An ensemble of classical electrons traveling along a circle before and after interacting with a short electric field pulse (HCP). Dispersion in velocities that result from the interaction causes the ensemble to bunch up in a small segment of the orbit. From ref. [67].

It has been proposed by Stroud, et. al., that a single HCP can induce localization in a uniformly distributed circular state[67]. The basic mechanism is illustrated in Fig. 5.15 using an ensemble of classical electrons. Each electron in the ensemble is initially distributed evenly throughout the orbit, and evolves with the same angular

velocity. Application of an electric field pulse causes a change in momentum to each electron which is proportional to its initial momentum component in the direction of the applied field. Because the electrons have a uniform angular velocity distribution, the subsequent change in momentum only depends on the initial position in the orbit. Immediately following the application of the pulse, the electron positions are unchanged but there now exists a range of momenta (and subsequently energies). This then leads to a bunching of the angular distribution as the faster moving particles catch up to the slower moving ones. This simple model is classical; however, it can be shown that the overall dynamics are preserved in the quantum mechanical description[67].

As mentioned above, the quasi-equilibrium state following turn off of the pump field is an excellent starting point for studying pulse induced wavepacket focusing. The probability density 150 ns after the pump field turn off is shown in Fig 5.16. This plot shows a near uniform distribution in azimuthal angle around the orbit.

Figure 5.17 shows the pulse sequence used to explore the effect of pulse induced wavepacket re-focusing. First, the angular momentum transforming pump pulse, $F_z^{pump} = -10$ mV/cm and 43 ns duration, is applied to a quasi-1D atom initially oriented in the $x$ direction. After allowing the wavepacket to dephase, a single HCP is applied directed along the $z$ axis towards the nucleus.

Figure 5.18 shows the time evolution of both the angular and radial distributions following application of an HCP with scaled strength of $\Delta p = -0.035$ 150 ns
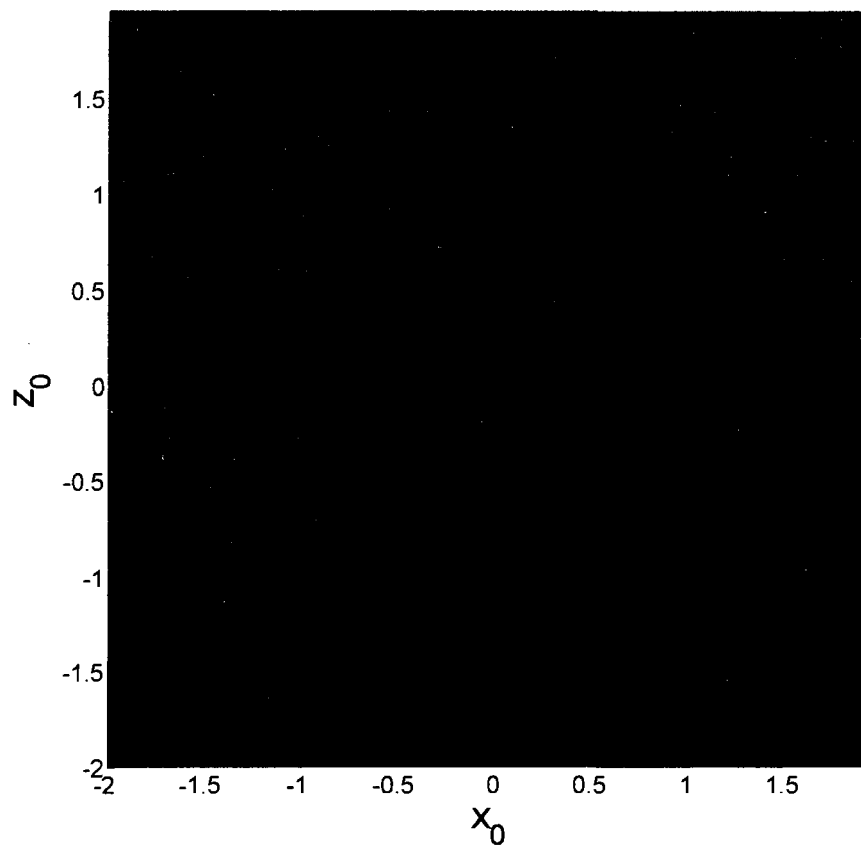
Figure 5.16 : Electron probability density of uniformly distributed near-circular state 150 ns after pump field turn off.

after the pump field turn off. Initially the angular probability density is uniformly distributed. Shortly after the HCP is applied, the angular distribution narrows indicating wavepacket localization. The angular distribution reaches a minimum in width (thus optimum localization) at 162 ns or after about three orbital periods. Just as in the previous example of a circular wavepacket, after the peak in localization occurs the wavepacket begins to dephase. Figure 5.18(b) shows that the radial distribution
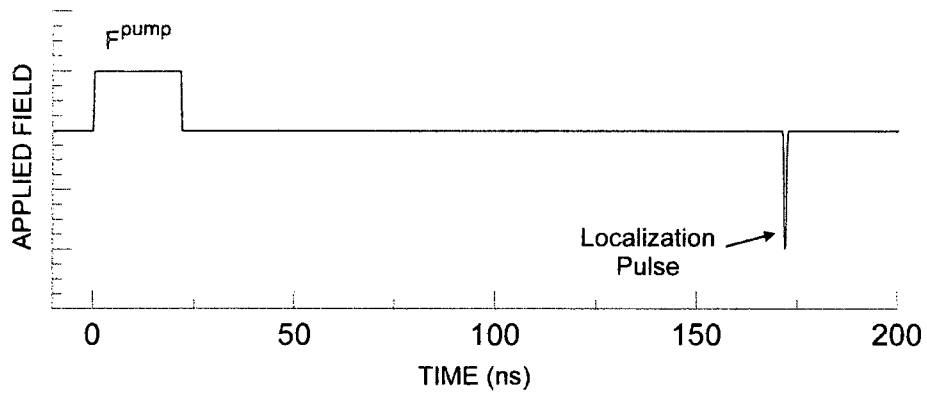
Figure 5.17 : Pulse sequence used to examine pulse induced focusing of quasi-equilibrium near circular states.
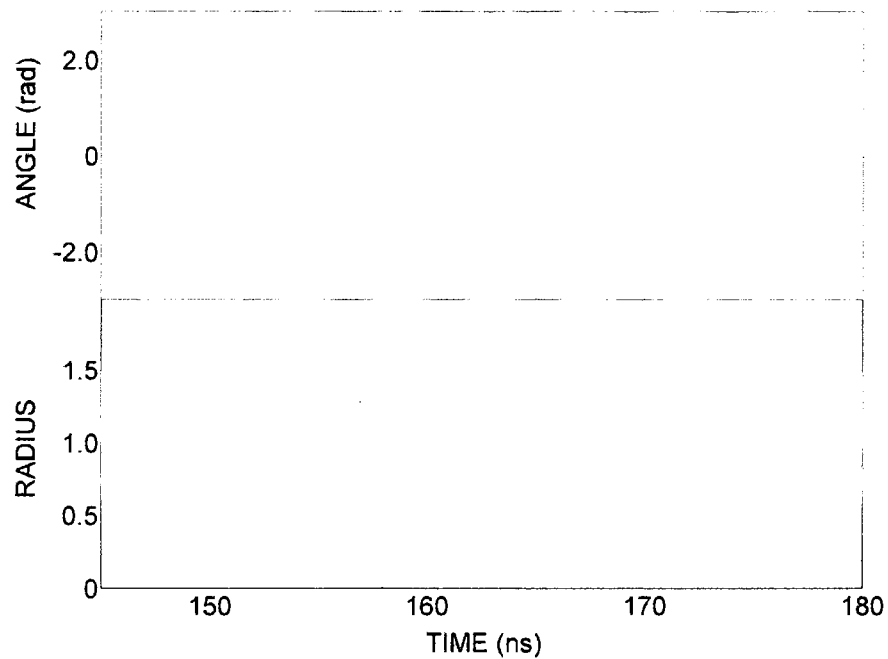


Figure 5.18 : CTMC calculations of the time dependence of (a) the angular and (b) the radial distributions of the wavepacket following application of a HCP of scaled strength $\Delta p_{L0} = -0.035$ at $t_D = 150$ ns to a near circular $n = 306$ state.

remains constant during this process.
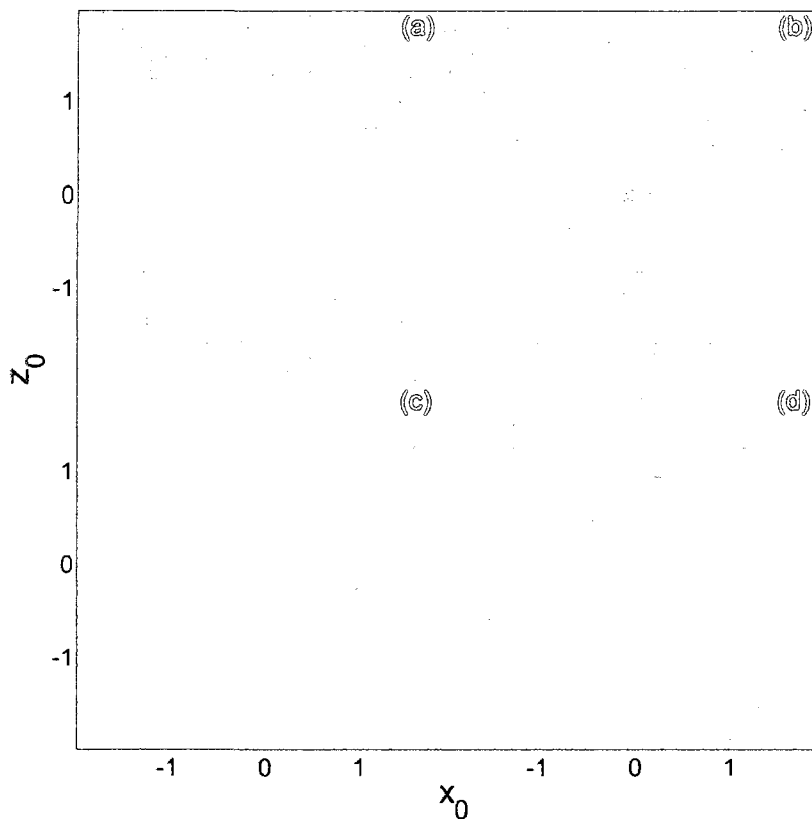


Figure 5.19 : Spatial probability density snapshots following application of a single localization pulse to the quasi-equilibrium circular state.

Snapshots of the calculated spatial probability density following application of the localization pulse are shown in Fig 5.19. Clear orbital motion of a localized wavepacket is evident and persists for several orbits. At later times, due to the energy distribution (somewhat broadened by the HCP), the wavepacket dephases leading to loss of angular localization.
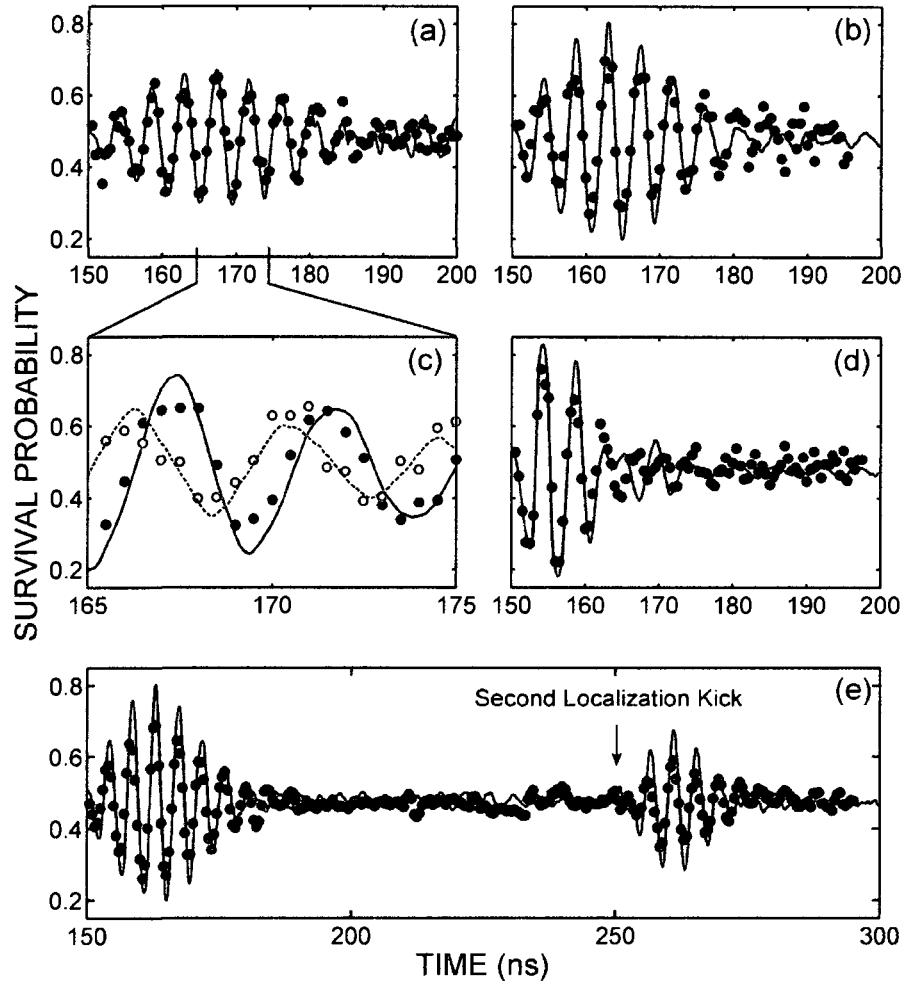
Figure 5.20 : Experimental (symbols) and calculated (lines) survival probabilities following application of localization HCPs with scaled strenghs $\Delta p_z$ of (a) -0.018 (b) -0.035 (d) -0.1 150 ns after turn-off of $F_z^{pump}$. The probe pulses were applied in the $x$ (red) and $z$ (black) directions. The expanded plot in (c) demonstrates the 90° phase shift between measurements in the two directions. (e) Re-localization induced by a second HCP of strength $\Delta p_z = -0.035$ applied 100 ns after an initial localizing pulse of the same strength.

This effect was investigated experimentally in the same manner as outlined in

Sect. 5.2.2. A probe pulse of 100 mV/cm and 6 ns duration was applied in both the $x$

and $z$ directions (large enough to ionize 50% of the Rydberg atom population). The position of the pulse was varied and the survival probabilty measured as a function of probe delay time. The results of this experiment are shown in Fig. 5.20 for a variety of HCP strengths. The buildup of strong periodic variations in the survival probability following application of the HCP is observed. This and the 90° phase shift between measurements with the probe field oriented along the $x$ and $z$ axes, i.e., in the evolution of $\langle x \rangle$ and $\langle z \rangle$, demonstrate strong azimuthal focusing and transient creation of a Bohr-like wave packet moving in near-circular orbit with angular frequency $\omega_n \sim 2\pi/T_n \sim n^3$. At late times azimuthal focusing is lost through dephasing. The focusing time, $t_{focus}$, or equivalently, the dephasing time, depends sensitively on the strength of the HCP varying as $\sim 1/\Delta p_z$ as expected. Strong HCPs lead to population of a relatively broad band of $n$ levels ($\Delta n \approx \pm n\Delta p_{z0}$). While this results in stronger and more rapid localization of the wave packet, its dephasing is also more rapid. Use of weaker HCPs results in a narrower band of final $n$ states reducing the dephasing rate but requiring longer for the wave packet to achieve optimum localization. The experimental data are in excellent agreement with CTMC simulations.

At sufficiently late times following the "localizing" HCP the wave packet dephases and becomes uniformly distributed in the azimuth when application of a further HCP can, as illustrated in Fig. 5.20(e), lead to regeneration of a transiently localized wave packet. Such regeneration can be continued for extended periods simply by applying further (alternating) HCPs. However, each HCP broadens the atomic $n$
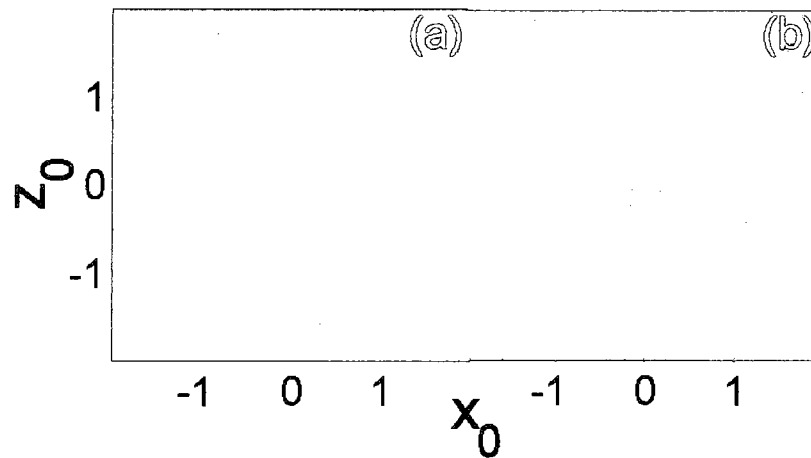
Figure 5.21 : Spatial distributions at peak angular localization following application of a third and fifth [(a) and (b)] re-localization HCP applied 350 ns and 550 ns after the pump field.

and $l$ distribution and the degree of localization and the times over which it can be maintained decrease as the number of HCPs is increased. This is evident in Figs. 5.21 which show the optimum localization achieved following a third and a fifth localization kick. After the third localization kick, the minimum azimuthal width is increased by more than 40% relative to that obtained after the first localization kick. Following the fifth localization kick, only minimal localization is observed.

## 5.4   Periodically Driven Circular Wavepacket Stabilization

In the previous section, it was demonstrated that it is possible to re-induce localization to a uniformly distributed near-circular state using just a single pulse. It was also

shown that it is possible to regenerate localized wavepackets by applying further kicks. However, each additional kick leads to a small amount of energy broadening which places an upper limit on the usefulness of this technique. The use of smaller kicks reduces this effect since the energy broadening induced increases with the strength of the applied kick. Therefore a periodic train of relatively small pulses might be an excellent way to maintain wavepacket localization for extended periods. However, a smaller applied kick requires a longer time to reach optimum localization. The solution to this problem is to simply apply the localization pulse train before the original wavepacket has a chance to dephase. In this case, extremely small pulses can be used which minimize the induced energy broadening. However, because the wavepacket is already tightly localized in the azimuthal angle, we do not require that the pulse train induce localization. This pulse train need only prevent the wavepacket from spreading.
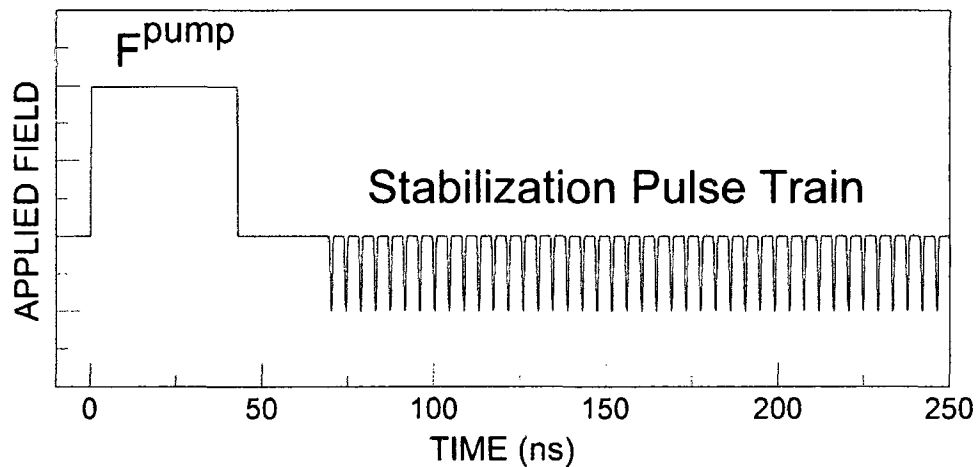


Figure 5.22 : Pulse sequence used to maintain localization for extended periods.

The pulse sequence used for maintaining wavepacket localization for extended periods is shown in Fig. 5.22. The pulse train is applied at the time of optimum localization following the turn-off of a 43 ns-duration 10 mV/cm pump field. The period of the applied train is 4.3 ns which is equal to the orbital period of the wavepacket. Each pulse in the train delivers a scaled stength of $\Delta p_{train} = -0.0035$ (a factor of ten less than what was used in Sect. 5.3).
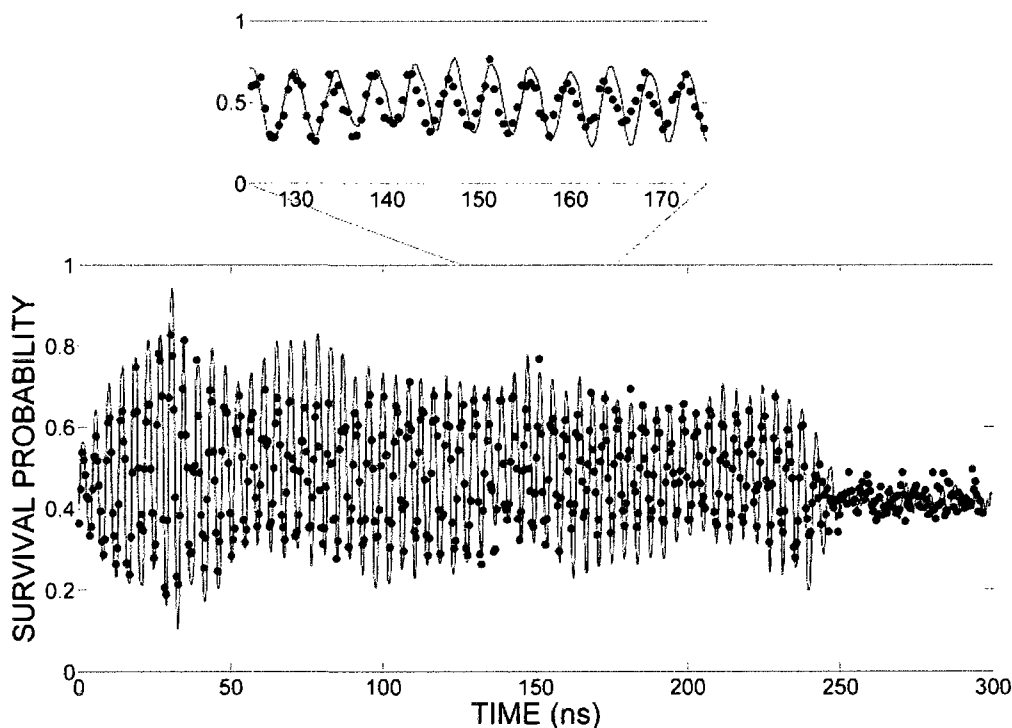


Figure 5.23 : Experimental (symbols) and calculated (lines) survival probabilities resulting from a probe delay experiment in the $z$ direction using a 50 pulse stabilization train applied 27 ns after the turn off of a 10 mV/cm pump field. The train had a period of 4.3 ns and an a scaled impulse of $\Delta p_{train0} = -0.0035$. The top plot shows an expanded section of the data.

The result of applying such an HCP train is shown in Fig. 5.23. The evolution of

the wavepacket position coordinate during the HCP train is monitored by the sudden application of a dc probe field, $F^{probe}$, directed along the $z$ axis. Pronounced periodic variations in the survival probability (and thus $\langle z \rangle$) are evident and continue for nearly 250 ns at which time the stabilization train is turned-off. In the absence of the applied train, the wavepacket quickly dephases. Measurements along the $x$-direction reveal similar behavior, but with the expected 90° phase shift which is indicative of uniform circular motion.

Attempts to extend these results to longer times showed a gradual reduction in amplitude of oscillations. The problem was solved by considering the evolution of the angular momentum of the wavepacket during the application of the stabilization train. Figure 5.24 shows the evolution of $\langle x \rangle$ and $\langle L_y \rangle$ during a 4.3 ns stabilization train with kick strength of $\Delta p_{train}$ = -0.0089 and -0.018. The DC component of the applied train causes the angular momentum of the wavepacket to precess with a corresponding reduction in the amplitude of oscillations in $\langle x \rangle$. Notice that by doubling the amplitude of the applied pulse train (and thus the DC component), the rate at which the angular momentum precesses also doubles.

This effect can be countered by applying a small dc offset during the train. Figure 5.25 shows the evolution of the angular momentum distribution with and without a cancelling offset field. The difference between the two cases is dramatic. Without the small offset field, the angular distribution oscillates between the maximum and minimum extreme values with a period of 1200 ns. However, when the small offset is
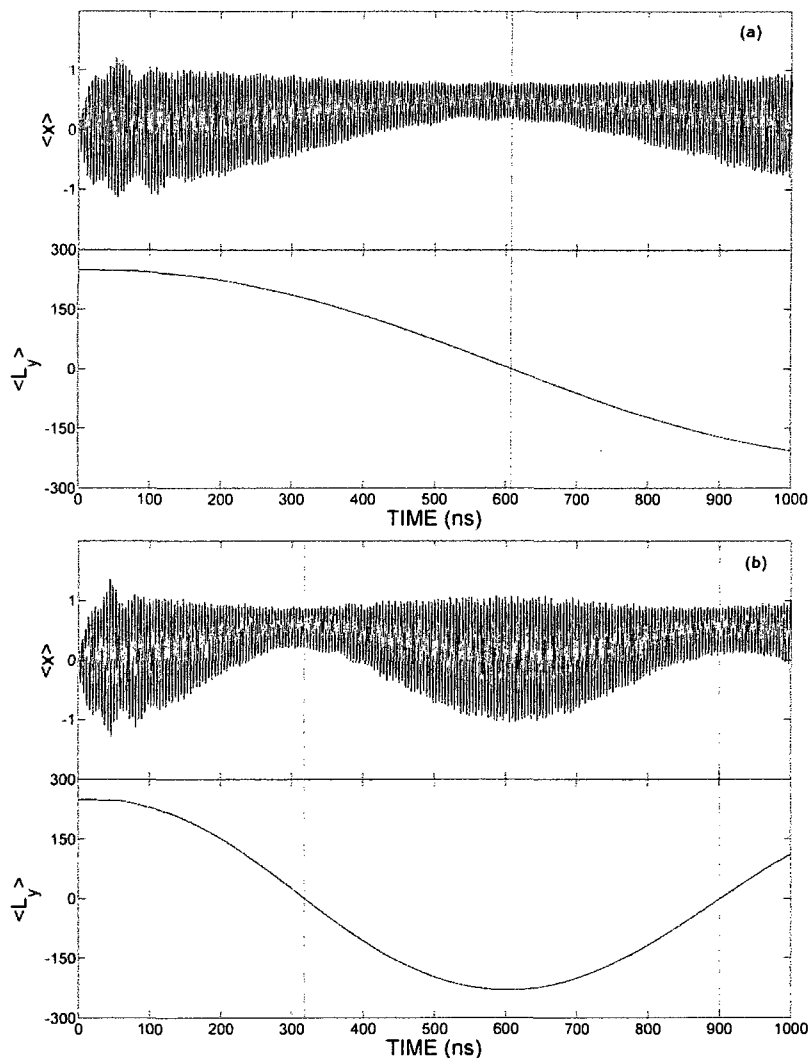
Figure 5.24 : Evolution of $\langle x \rangle$ and $\langle L_y \rangle$ during a 4.3 ns stabilization train with kick strengths of (a) $\Delta p_{train} = -0.0089$ and (b)$\Delta p_{train} = -0.018$. The red verticle lines indicate when the wavepacket reaches a minimum in $|L_y|$.

applied to cancel the dc component of the train, the angular momentum distribution remains essentially unchanged.

Figure 5.26 shows the applied field profile of the stabilization pulses with the dc
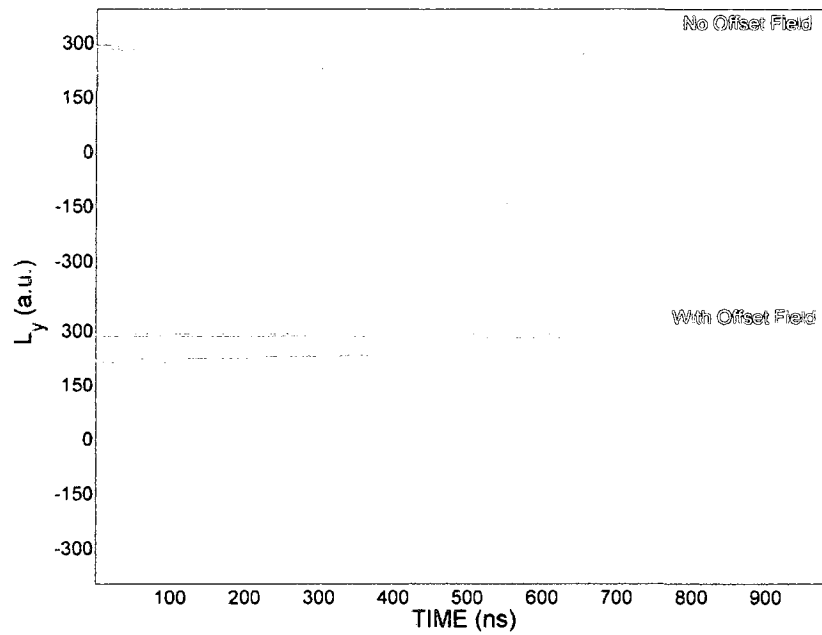
Figure 5.25 : Evolution of the angular momentum distribution during a stabilization train of period 4.3 ns and kick strength $\Delta p_{train}$ = -0.0089 with and without an offset to cancel the DC component of the train.
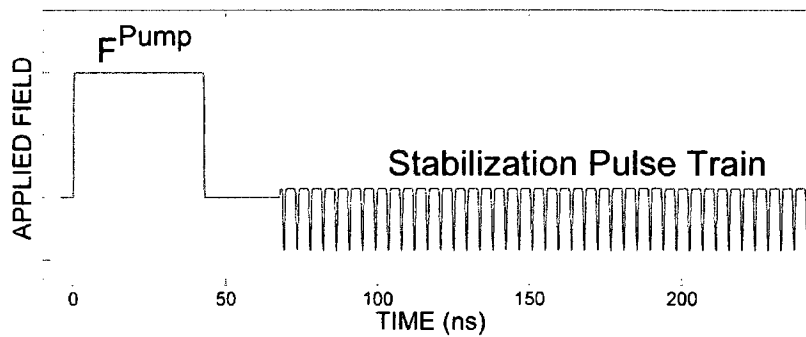


Figure 5.26 : Pulse profile of wavepacket stabilization train with a dc component canceling offset.

component of the train cancelled. This allows the stabilization of the wavepacket for extended periods. As is evident from Fig. 5.27, even after $\sim$ 100 orbits the wavepacket
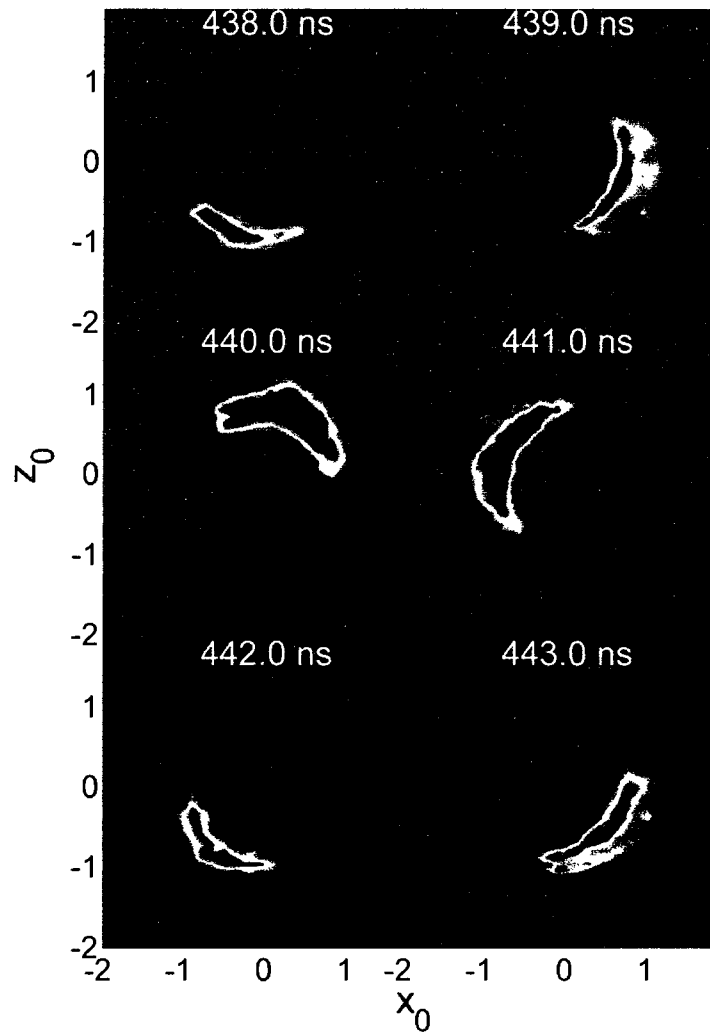
Figure 5.27 : Snapshots of the (simulated) electron probability density distribution showing the time dependent behavior of the wavepacket after $\sim 100$ orbits. The times indicated are the times after turn-off of the pump field $F_z^{pump}$.

remains localized and continues to move in a near-circular orbit. A sustained Bohr-like wavepacket, however, can only be achieved with a careful choice of driving field, i.e., of the kick strength, period, and phase. Tests revealed that if the kick strength is too small localization is not maintained. If it is too large the wavepacket broadens

and becomes progressively less well localized. A kick strength of $\Delta p_{train} = -0.018$ was found to be optimal. The period $T_p$ of the HCP train must also match closely the initial electron orbital period $T_n = 4.3$ ns.
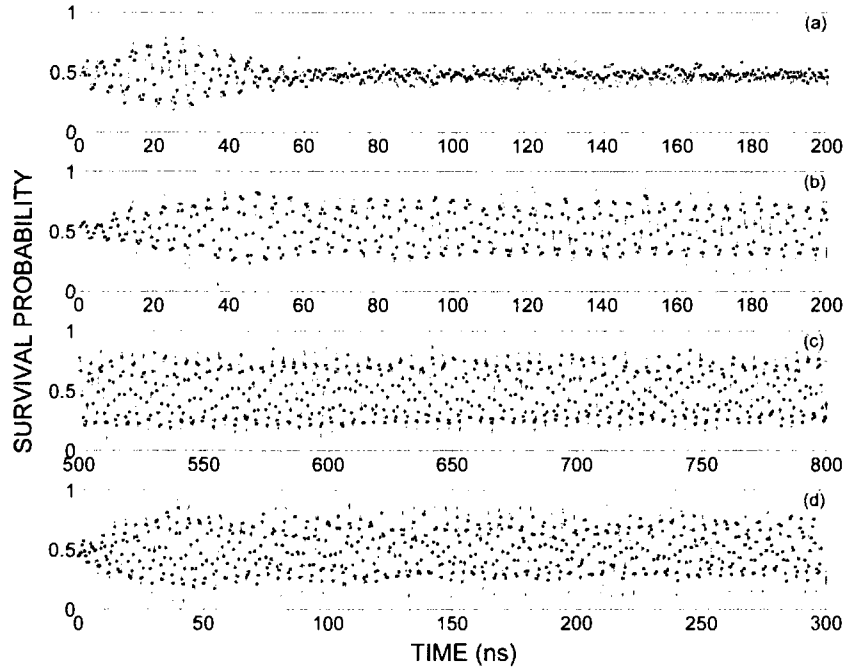


Figure 5.28 : Experimental (symbols) and calculated (lines) survival probabilities for a probe pulse of 6 ns duration and 100 mV/cm amplitude as a function of its time of application after turn-off of the pump field $F_z^{pump}$. The different panels show results obtained with: (a) no HCP train applied; (b) and (c), a train of HCPs of strength $\Delta p_{z0} = -0.018$ and period $T_p = 4.3$ ns initiated following a delay $t_D = 27.5$ ns; and (d) same as for (b) and (c) but with a pulse period $T_p = 8.6$ ns. All results were obtained with the probe pulse applied in the $+z$ direction.

Figure 5.28 shows the experimental and calculated results of using this optimized pulse sequence. Frame (a) shows the result without the stabilization train, and as expected localized wavepacket motion is observed for several orbits before dephasing. Figure 5.28 (b) shows the result of using the optimized stabilization train on an iden-

tical time scale. In this case, a localized wavepacket is maintained with no evidence of dephasing. Figure 5.28 (c) shows the same data set but at much later times. Again, clear periodic motion is observed without any reduction in the amplitude of oscillation. The effect of driving the wavepacket at half the orbital period ($T_p = 8.6$ ns) is shown in Fig. 5.28(d). Figure 5.29 demonstrates the sensitivity of the stabilization to the driving parameters. Figure 5.29(a) shows the results for the same conditions as for Fig. 5.28(b) to allow easier visual comparison. Figures 5.29 (b) and (c) show the effect of driving the wavepacket with periods of $T_p = 3.7$ and 5.0 ns respectively. In both cases the wavepacket is destroyed within several orbits after application of the pulse train. The timing of the HCPs relative to the position of the wavepacket in its orbit is also critical. As is evident from Figs. 5.29 (a) and (d), generation of a sustained wavepacket requires that the HCPs start when the wavepacket is centered on the $+z$ axis, i.e., at $x \sim 0$, $z \sim +n^2$.
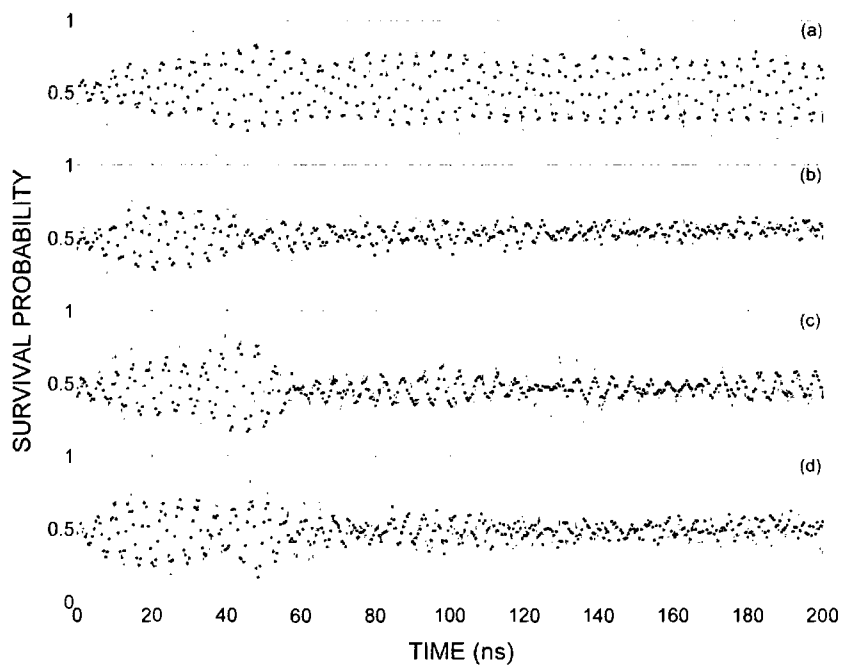
Figure 5.29 : Experimental (symbols) and calculated (lines) survival probabilities as a function of time after turn-off of the pump field. The different panels show results obtained with: (a) the same conditions as in Fig. 5.28(b); (b), (c) as in (a) but with HCP periods $T_p = 3.7$ and 5.0 ns, respectively; (d) as in (a) but with a delay time $t_D = 29$ ns.

# Chapter 6

# Conclusions and Outlook

## 6.1 Conclusions

This work has demonstrated the remarkable level of control that can be exercised in the manipulation of Rydberg atom wavepackets in one and two dimensions.

The application of a periodic train of HCPs gives rise to islands of stability in the Poincaré surface of section in phase space. A pulse sequence which includes two preparatory pulses preceding the periodic train can be used to efficiently and selectively load a Rydberg atom wavepacket into an island of stability. By varying the available control parameters (i.e. the amplitude and time delay between preparation pulses) one can selective load the resulting stablized wavepacket anywhere withing the stable island. The extreme cases of this technique lead to the population of the center of the island and the periphery or "shore" of the island. Placing the wavepacket in the center of the island results in a wavepacket with a nearly static energy distribution. However, placing the wavepacket on the edge of the island results in the periodic evolution of the wavepacket around the perimeter of the island. This periodic motion is accompanied by oscillations in the energy distribution of the wavepacket. This variation in energy was observed by monitoring the evolution of the wavepacket with

a probe delay experiment. The results were in excellent agreement with CTMC predictions.

It was also shown that once a wavepacket is optimally loaded into an island, the position of the island in phase space can be shifted by adiabadically chirping the period of the applied HCP train. If the change in period for each adjacent pulse is small compared to the orbital period of the electron($\delta T_P \ll T_n$), the transfer is efficient, with more than 90% of atoms surviving the process. Because a shift of a stable island in the direction of increasing position coordinate constitutes an increase in energy, by carefully controlling the final position of the stable island, the final energy of the wavepacket can also be controlled. SFI measurements confirmed that a train of 50 chirped pulses efficiently transported an initial wavepacket at $n = 350$ to $n = 650$. CTMC calculations and measurements of the final momentum disribution demonstrated the spatial polarization of the initial state was preserved. It was also found that by reversing the direction of chirping, the transport process can be reversed. In addition to the larger period-1 island of stability in phase space, there also exist other islands which correspond to more complicated motion. The period-2 island is such an example. It was also demonstrated that after a chirped pulse sequence, by superimposing a second period train onto the first and then adabadically varying the spacing between the two trains, the wavepacket can be transferred to the period-2 island.

Previous attempts to create a two dimensional (near-circular) wavepacket by ap-

plying a single large orthogonal HCP to a quasi-1D atom have met with limited success. This technique led to the population of a large range of energy levels thus making attepts at manipulation and control rather limited. However, by using a relatively small static transerve pump field, the angular momenum of the inital quasi-1D atom can be controlled to a high degree of precision. The resulting localized wavepacket has created a new series of experiments in two dimensions. Simply by tuning the parameters of the pump pulse (such as the amplitude and rise/fall time), the lifetime of wavepacket can be greatly enhanced by minimizing the width of the resulting energy distribution. However, even the equilibrium state several hundred nanoseconds following the dephasing of the wavepacket provides a laboratory for studying interesting dynamical effects. It was demonstrated that localization can be re-induced using a single HCP. in addition, by applying a phase and frequency matched pulse train during the time of initial optimum localization, a non-dispersing near circular wavepacket can be created. To date, this wavepacket represents the closest experimentally verified analog to the original Bohr atom.

## 6.2  Outlook

It seems that the remarkable control that is achievable using near-circular wavepackets represents just the beginning in a new series of experiments. This situation is analogous to the discovery of stable islands in the phase space of periodically driven one-dimensional atoms. Much like in the 1D case, it seems that once the near-circular

wavepacket is locked to a driving train, the parameters of the train can be adiabadically varied thus transporting the wavepacket to some different region of phase space. Calculations along these lines seem very promising. Using a carefully tailored sequence of frequency chirped pulses, it should be possible to efficiently transport stabilized near-circular wavepackets to arbitrarily high $n$. The largest experimental challenge is the ability to create a chirped pulse train whose dc component is compensated for thus preventing unwanted angular momentum precessing.

The technique used to dynamically stabilize the near circular wavepacket might by used to selectively filter out states within a narrow energy range from a broadened distribution. This techique could be applied to dynamically filter the range of states created by applying a single large orthogonal HCP to the initial quasi-1D atom.

Past experiments have explored the effect of the application of so-called "colored" noise to the dephasing of wavepackets[68]. Colored noise differs from typical white noise in that it contains some well defined characteristic frequency content which can be controlled. This technique has been very useful in quantitatively analyzing the stability of dynamical systems. It would be interesting to use this technique to study the frequency dependence and robustnest of the dynamically stabilized near-circular wavepacket.

The techniques we have developed for controlling the angular momentum of the Rydberg atom may have applications in quantum information processing. A single transverse pump pulse, with the appropriate duration and amplitude, can transform

the initial quasi-1D Rydberg atom to states of extreme scaled angular momentum $L_0 = \pm 1$. It is not hard to imagine each of these states representing the "0" and "1" of an atomic "bit" of information. With the appropriate pulse sequence, it would be possible to test which extreme angular momentum state was populated. Such a sequence would constitute a "read" operation while the angular momentum transforming pump pulse would represent a "write" operation.

# Bibliography

[1] R. Carley, E. Heesel, and H. Fielding, *Chemical Society Reviews* **34**, 949 (2005).

[2] F. Dunning, J. Lancaster, and C. Reinhold, *Advances in Atomic Molecular and Optical Physics* **52**, 49 (2005).

[3] T. Kopyciuk and R. Parzynski, *Phys. Rev. A* **75** (2007).

[4] E. Persson, K. Schiessl, and A. Scrinzi, *Phys. Rev. A* **74** (2006).

[5] M. Drescher, M. Hentschel, R. Kienberger, M.Uiberacker, V. Yakovlev, A. Scrinzi, T. Westerwalbesloh, U. Kleineberg, U. H. U, and F. Krausz, *Nature* **419**, 803 (2002).

[6] A. Zewail, *J. Phys. Chem. A* **104**, 5660 (2000).

[7] T. Gallagher, *Rydberg Atoms*, Cambridge University Press, 1994.

[8] R. Arbines and I. Percival, *Proc. Phys. Soc. London* **88**, 861 (1966).

[9] M. Frey, F. Dunning, C. Reinhold, and J. Burgdorfer, *Physical Review A* **53** (1996).

[10] C. Reinhold, J. Burgdorfer, M. Frey, and F. Dunning, *Physical Review A* **54** (1996).

[11] S. Yoshida, C. Reinhold, J. Burgdorfer, B. Tannian, R. Popple, and F. Dunning, *Physical Review A* **58** (1998).

[12] H. A. Bethe and E. A. Salpeter, *Quantun Mechanics of One and Two Electron Atoms*, Academic Press, 1957.

[13] L. D. Landau and E. M. Lifshitz, *Quantum Mechanics*, Pergamon Press, 1977.

[14] M. L. Zimmerman, M. G. Littman, M. M. Kash, and D. Kleppner, *Physical Review A* **20** (1979).

[15] K. Helfrich, *Theoretica Chimica Acta* **24** (1972).

[16] F. Dunning and R. Stebbings, *Rydberg States of Atoms and Molecules*, Cambridge University Press, 1983.

[17] T. Gallagher, L. Humphrey, W. Cooke, R. Hill, and S. Edelstein, *Physical Review A* **16** (1977).

[18] W. Cooke and T. Gallagher, *Physical Review A* **17** (1978).

[19] D. Bailey, J. Kiskes, and A. Riviere, *Nucl. Fusion* **5** (1965).

[20] J. Hirschfelder and L. Curtis, *J. Chem. Phys.* **55** (1971).

[21] M. Rice and R. Good, *J. Opt. Soc. Am.* **52** (1962).

[22] C. Reinhold, M. Melles, and J. Burgdorfer, *Physical Review Letters* **70** (1993).

[23] C. Reinhold, M. Melles, H. Shao, and J. Burgdorfer, *J. Phys. B.* **26** (1993).

[24] B. Bransden and M. McDowell, *Charge Exchange and the Theory of Ion-Atom Collisions*, Oxford, Clarendon, 1992.

[25] R. Olson and A. Salop, *Physical Review A* **16** (1977).

[26] I. Percival and R. D, *Adv. Mol. Phys.* **11** (1975).

[27] C. Reinhold and C. Falcon, *J. Phys. B* **21**, 1829 (1987).

[28] B. Leaf, *J. Math. Phys.* **9**, 769 (1968).

[29] C. Reinhold, *Nucl Instrum Meth B* **56**, 18 (1991).

[30] S. Yoshida, *Quantum chaos in the periodically kicked Rydberg atom*, PhD thesis, University of Tennessee, 1999.

[31] R. Arbines and I. Percival, *Proc. Phys. Soc. London* **88**, 873 (1966).

[32] C. Reinhold and J. Burgdorfer, *J. Phys. B* **26**, 3101 (1993).

[33] Hezel, Burkhardt, Ciocca, and Leventhal, *Am J. Phys* **60**, 324 (1992).

[34] C. Reinhold, W. Zhao, J. Lancaster, F. Dunning, E. Persson, D. Arbo, S. Yoshida, and J. Burgdorfer, *Physical Review A* **70** (2004).

[35] B. Tannian, C. Stokely, F. Dunning, C. Reinhold, S. Yoshida, and J. Burgdorfer, *Physical Review A* **62**, 043402 (2000).

[36] C. Stokely, *The Study of the Perturbation of Rydberg Atoms by Half Cycle Pulses*, PhD thesis, Rice University, 2002.

[37] J. Ahn, T. Weinacht, and P. Bucksbaum, *Nature* **397**, 233 (1999).

[38] J. Ahn, T. Weinacht, and P. Bucksbaum, *Science* **287**, 463 (2000).

[39] H. Maeda, D. Norum, and T. Gallagher, *Science* **307**, 1757 (2005).

[40] J. Bromage and C. Stroud, *Phys. Rev. Lett.* **83**, R4963 (1999).

[41] A. Buchleitner and D. Delande, *Phys. Rev. Lett.* **75**, R1487 (1995).

[42] A. Buchleitner, D. Delande, and J. Zakrzewski, *Phys. Rep.* **368**, R409 (2002).

[43] F. Dunning, J. Lancaster, C. Reinhold, S. Yoshida, and J. Burgdorfer, *Adv. At. Mol. Opt. Phys.* **52** (2005).

[44] C. Reinhold, J. Burgdrfer, M. Frey, and F. Dunning, *Phys. Rev. Lett.* **79**, 5226 (1999).

[45] M. Frey, , X. Ling, B. G. Lindsay, K. A. Smith, and F. Dunning, *Rev. Sci. Instrum.* **64** (1993).

[46] S. Yoshida, C. Reinhold, E. Persson, J. Burgdorfer, and F. Dunning, *J. Phys. B* **38**, S209 (2006).

[47] A. Messiah, *Quantun Mechanics*, North-Holland, 1970.

[48] D. Arbo, C. Reinhold, J. Burgdorfer, A. K. Pattanayak, C. L. Stokely, W. Zhao, J. Lancaster, and F. Dunning, *Physical Review A* **67**, 063401 (2003).

[49] W. Zhou, J. Mestayer, J. Lancaster, F. Dunning, C. Reinhold, S. Yoshida, and J. Burgdorfer, *Phys. Rev. Lett.* **97**, 253003 (2006).

[50] C. Stokely, J. Lancaster, F. Dunning, D. Arbo, C. Reinhold, and J. Burgdorfer, *Phys. Rev. A* **67**, 013403 (2003).

[51] H. Schuster, *Deterministic Chaos*, VHC, Weinheim, 1973.

[52] L. E. Reichl, *The Transition to Chaos: Conservative Classical Systems and Quantum Manifestations*, Springer, New York, 2004.

[53] P. M. Koch and K. A. H. van Leeuwen, *Phys. Rep.* **255**, 289 (1995).

[54] D. A. Steck, W. H. Oskay, and M. G. Raizen, *Science* **293**, 274 (2001).

[55] J. Feist, A. Backer, R. Ketzmerick, S. Rotter, B. Huckestein, and J. Burgdorfer, *Phys. Rev. Lett.* **97**, 116804 (2006).

[56] C. O. Reinhold, S. Yoshida, J. Burgdrfer, B. E. Tannian, C. L. Stokely, and F. B. Dunning, *J. Phys. B.* **34**, L551 (2001).

[57] H. Maeda and T. F. Gallagher, *Phys. Rev. Lett.* **92**, 133004 (2004).

[58] S. Yoshida, C. O. Reinhold, P. Kristofel, J. Burgdorfer, S. Watanabe, and F. B. Dunning, *Phys. Rev. A* **59**, 4121 (1999).

[59] M. Kalinski and J. H. Eberly, *Opt. Express* **1**, 216 (1997).

[60] J. J. Mestayer, W. Zhao, J. C. Lancaster, F. B. Dunning, C. O. Reinhold, S. Yoshida, and J. Burgdorfer, *Phys. Rev. Lett.* **99**, 183003 (2007).

[61] M. Born, *The Mechanics of the Atom*, G. Bell and Sons, London, 1927.

[62] J. Murray-Krezan and R. R. Jones, *Phys. Rev. A* **75**, 063411 (2007).

[63] I. Percival and R. D, *J. Phys. B* **12**, 2051 (1979).

[64] C. P. Slitcher, *Principles of Magnetic Resonance*, Springer, New York, 1992.

[65] B. Tannian, C. Stokely, F. Dunning, C. Reinhold, S. Yoshida, and J. Burgdorfer, *Physical Review A* **64**, 021404 (2001).

[66] J. J. Mestayer, B. Wyker, J. C. Lancaster, F. B. Dunning, C. O. Reinhold, S. Yoshida, and J. Burgdorfer, *Phys. Rev. Lett.* **100**, 243004 (2008).

[67] Z. D. Gaeta, M. W. Noel, and C. Stroud, *Phys. Rev. Lett.* **73**, 636 (1994).

[68] S. Yoshida, C. O. Reinhold, J. Burgdorfer, W. Zhao, J. Mestayer, J. Lancaster, and F. B. Dunning, *Phys. Rev. A.* **75**, 013414 (2007).